Title	Effect of abnormal formation pressure on petroleum migration and entrapment, and its application to petroleum exploration
Title-Notes	石油の移動集積に対する異常地層圧力の影響とその石油探鉱への応用
Author	MORIYA, Shunji
Dept.	千葉大学理学研究科

Acknowledgement

I would like to express my sincere appreciation to Professor Susumu Kato and Professor Kazuo Nakayama, Graduate School of Science, Chiba University, Japan, for their supervision of this dissertation. It is indeed through the various geological evaluation works carried out under them that I have been stimulated my interest in petroleum migration and entrapment, the subject of this research. The examining committee members, Professor Makoto Ito, Professor Tanio Ito, Professor Nobuhiro Kotake and Professor Toshinori Sato of Graduate School of Science, Chiba University are also acknowledged for their advices and criticisms.

This research is made out from a number of projects which I conducted together with many colleagues in Japan Petroleum Exploration Co., Ltd. (JAPEX), JGI, Inc. and University College Dublin, Ireland. I would like to thank all of them for their helpful discussions and valuable recommendations during the projects.

Results of geological evaluation work in the Iwafuneoki field, Niigata, Japan constitute the core of this research. Three years working with my colleagues in JAPEX: Mr. Yuichi Saito, Mr. Terumasa Yamane, Ms. Mizue Nishimura, Mr. Kazuya Kondo, Mr. Kenichi Watanabe, Mr. Tetsuya Yamamoto and Dr. Osamu Takano is one of the most valuable and delightful time. I also would like to thank Mr. Hajime Saga, Japan Agency for Marine-Earth Science and Technology, who encouraged me in working on petroleum migration and entrapment in this field.

Experience in working on Norwegian Continental Shelf is of particular importance for gaining my idea about the role of abnormal formation pressure. I have received many valuable inputs from Professor John J. Walsh, School of Geological Sciences, University College Dublin, Ireland, my colleagues in Fault Analysis Group, especially Dr. Conrad Childs and Dr. Tom Manzocchi, and Dr. Øyvind Sylta of Migris AS, Norway.

I have conducted a series of numerical simulations in this research. Dr. Daniel J.F. Carruthers, Permedia Research Group, Canada, kindly allowed me to use the research code of his simulator MPath. His cooperation and many suggestions are really appreciated.

Finally, I would like to acknowledge Japex Offshore Ltd., JAPEX, Mitsubishi Gas Chemical Company, Inc. and Idemitsu Oil & Gas Co., Ltd. for permission to use their data.

Abstract

The effect of abnormal formation pressure on petroleum migration and entrapment is one of the disputed problems in petroleum systems analysis. The mechanism on how abnormal formation pressure affects petroleum migration and entrapment are discussed, and a practical approach to use abnormal formation pressure data for optimizing migration models is demonstrated.

The abnormal formation pressure does not have a direct influence on petroleum migration and entrapment, *i.e.* it does not promote nor prevent the trapped petroleum to leak, based on theoretical consideration of pressure profile in reservoirs and examination of field examples.

However, there are close mutual relationships between abnormal pressure and permeability, and between permeability and capillary threshold pressure. Therefore abnormal pressure data can be used to predict capillary threshold pressure of seal rocks and to optimize petroleum migration and entrapment models.

Validity and applicability of the above model are examined by a case study in the Iwafuneoki field, Japan. It successfully reproduced both pressure and petroleum distribution in the field with acceptable accuracy.

The finding on the role of abnormal formation pressure has a potential impact on prospect evaluation for petroleum exploration. It can cast a new light on undiscovered or overlooked prospects in overpressured areas.

Continuing improvements of the models by using all the data and knowledge including abnormal formation pressure are necessary to better understanding of petroleum migration and entrapment. Those challenges will lead the migration modelling to a real prediction tool.

Table of contents

List of Figures

List of Tables

List of symbols

a	Characteristic length scale (pore throat radius)
BFV	Capillary-bound fluid volume from NMR log
B_o	Bond number
c	Compaction coefficient
C_a	Capillary number
D [m]	Diameter of rock grains
F [N/m^3]	Force on a unit volume of fluid, or lithology factor
F	Lithology factor
FFV	Free fluid volume from NMR log
g [m/s^2]	Acceleration due to gravity, 9.80665 m/s2
G_f [kg/kg]	Fraction of gas dissolved in oil
h [m]	Hydraulic head
h_c [m]	Petroleum column height
k [m^2 or mD]	Absolute or intrinsic permeability. Subscripts h and v refer to horizontal and vertical, respectively.
k_o	Shape factor
k_r [m^2/m^2]	Relative permeability. Subscripts w, o and g refer to water, oil and gas, respectively.
k_{TIM} [m^2]	NMR (nuclear magnetic resonance log) permeability by Timur-Coates model
P [Pa]	Gauge pressure. Subscripts w, o and g refer to water, oil and gas, respectively
P_c [Pa]	Capillary pressure. Subscripts ma, ow and gw refer to mercury-air, oil-water and gas-water, respectively
P_{ex} [Pa]	Excess pressure or overpressure
P_{hy} [Pa]	Hydrostatic pressure
P_{th} [Pa]	Capillary threshold pressure (displacement pressure). Subscripts ma, ow and gw refer to mercury-air, oil-water and gas-water, respectively
q [m^3/m^2/s]	Darcy's velocity defined as volume flux of fluid passing across unit area of the rock per unit time. Subscripts w, o and g refer to water, oil and gas, respectively.
$\bar{r}_p$ [m]	Mean pore radius of the rock
r_p [m]	Pore radius of the rock
r_t [m]	Pore-throat radius of the rock
R_e	Reynolds number

s [m²/ m³]	Specific surface
S [frac]	Fluid saturation. Subscripts *w*, *o* and g refer to water, oil and gas, respectively.
S [Pa]	Overburden pressure
S_{wir} [frac]	Irreducible water saturation
S_{or} [frac]	Residual oil saturation
Vcl [frac]	Clay volume
z [m]	Height above the datum elevation (z increases as elevation increases)
ΔT [μs/ft]	Transit time from sonic logs
ΔT_o [μs/ft]	Sonic transit time of mudstone at surface
ΔT_n [μs/ft]	Normal trend line of sonic transit time for mudstone
ϕ [m³/m³]	Porosity
ϕ_0 [m³/m³]	Surface porosity
Φ [Pa]	Fluid potential. Subscripts f, *w* and *p* refer to fluid, water and petroleum, respectively
γ [N/m]	Interfacial tension.
μ [Pa.s]	Fluid viscosity. Subscripts *w* and *p* refer to water and petroleum, respectively
θ [rad]	Contact angle between petroleum and rock
ρ [kg/m³]	Fluid density. Subscripts *w* and *p* refer to water and petroleum, respectively
σ_v [Pa]	Vertical effective stress
τ [m/m]	Tortuosity of pore

1 Introduction

1.1 Objectives

Since Magoon and Dow (1994) pointed out the importance of petroleum systems analysis, *i.e.* evaluating petroleum potential systematically by integrating all the elements and processes involved for petroleum formation, analysis of petroleum migration and entrapment has become a fundamental requirement in evaluation workflows. However, in the author's view, those analyses are still rarely quantitative and many are nothing but a ritual step to back *implicitly* explorationists' ideas which often heavily rely on other aspects of the petroleum system such as geologic structure, reservoir facies distribution, seismic attribute anomalies - *i.e.* delineation of traps. It demonstrates that the analysis of petroleum migration and entrapment is far from being used as a predictive tool in practical petroleum exploration.

Indeed, there still remain many to be solved or improved, from fundamental mechanisms to practical ingenuity, to create geologically more plausible migration and entrapment models. How the abnormal formation pressure affects petroleum migration and entrapment is one of the disputed problems, and it is the main subject of this research.

Retard of water flow in mudstones or other impermeable (more correctly less permeable) rocks results in development of abnormal formation pressure. It is believed that this abnormal pressure may affect petroleum migration and entrapment, in particular, capacity of the seal rocks. If this happens, it would have a significant impact on predicting petroleum column height and hence evaluating petroleum reserves. Furthermore, the petroleum leaked or spilled from a trap generally migrates toward other downstream traps. The effects are therefore not just on the trap in question, but also on other potential traps along the migration pathways.

Leaving aside the direct effects of abnormal pressure on migration and entrapment, the abnormal pressure itself is an indicator of one of the most important rock properties – permeability k. On the other hand, k is closely related to capillary threshold pressure P_{th}– another extremely important property which overwhelmingly controls petroleum migration and entrapment. Therefore abnormal formation pressure will provide with one of the most valuable data to predict P_{th} of the rocks, which is often poorly constrained. Many published works, unfortunately, assign k and P_{th} separately in their models, loosing the mutual correlation of k - P_{th} easily. It is expected that by calibrating P_{th} with abnormal formation pressure, migration models can become more plausible. Optimizing the migration models by utilizing all the data and information available, including abnormal

formation pressure, is another subject of this research, and is extremely important to make them feasible for practical exploration purpose.

In summary, this research has two objectives; they are firstly to discuss the mechanism on how abnormal formation pressure affects petroleum migration and entrapment, and secondly to demonstrate a practical approach to use abnormal formation pressure data for optimizing migration models. The author believes that better understanding of petroleum migration and entrapment can cast a new light on undiscovered or overlooked exploration prospects.

1.2 Methodologies

Three approaches are employed in this research to achieve the objectives. They are review of physical processes, re-examination of observed (field) data and numerical simulations.

(1) Review of physical processes

Petroleum migration and entrapment are commonly formulated by the same equations used in petroleum engineering field, which describe the fluid flow in reservoirs at production time scale. However, there are at least two very large differences between them, *i.e.* time scale and the rock involved.

Production time scale petroleum (and water) flow deals with the time scale of days or years, which contrasts with petroleum migration in millions of years. In addition, fluid flow at production time scale concentrates in permeable media and therefore flow in mudstones can simply be neglected, while petroleum (and water) migrates not only in sandstones or highly permeable media but also in mudstones or less permeable media at geological time scale. Abnormal formation pressure does indeed develop in mudstones or fault rocks as a consequence of the retard of water flow in those less permeable rocks at geological time scale.

Therefore, it is necessary to review the validity of the commonly used equations, which should describe petroleum and water flow both in sandstones and mudstones at geological time scale.

(2) Re-examination of observed (field) data

Any model or assumption must be proven by observed data. Various data from actual oil fields are collected to verify the models proposed in this research.

It is a common practice that same observed data lead very different conclusions. It is because interpretation of the data is highly dependent on the interpreters' view. Observed

data which have been used to explain a different model are therefore re-examined from the new viewpoint.

(3) Numerical simulations

Because of its geological complexity and spatial and time scale involved (sedimentary basin scale and geological time scale), problems on migration and entrapment can be best solved numerically, rather than analytically or experimentally. Therefore, numerical simulations are extensively used in this research to examine the validity and applicability of the models.

Any flow in the subsurface occurs in three dimensional spaces. Consequently, it is needed to numerically solve both water and petroleum flow in 3D. Furthermore, the model should have a sufficient resolution to reproduce the complexity of geology. A most adequate commercial simulator is used to meet these requirements.

1.3 Organisation

This dissertation consists of seven chapters.

After making clear the objectives and methodologies in Chapter 1, the author starts Chapter 2 with a review of key terms, concepts and equations on secondary migration and entrapment of petroleum, based on the published researches. Some of the issues are still in debate, and for those the author would like to define his position, as they are the assumptions adopted in this research.

In Chapter 3, the effects of abnormal pressure in water phase in reservoirs on petroleum migration and entrapment are discussed by theoretical consideration and from field examples.

Abnormal pressure indirectly indicates the existence of effective capillary seals via the close relationship between permeability k and capillary threshold pressure P_{th}. Chapter 4 is devoted for establishing appropriate k - P_{th} relationship to predict the capillary sealing capacity by using abnormal pressure data.

In chapter 5, the author would like to give an example of regional-scale petroleum migration modelling in the Iwafuneoki field, Japan to examine the validity and to illustrate the applicability, of the model proposed in the previous chapters.

The author would like to discuss on the insights into further petroleum exploration and on the subjects for future researches in Chapter 6, and conclude with listing the main findings in Chapter 7.

2 Review on the mechanism of secondary migration and entrapment of petroleum

Before taking up the main subject, the author would like to review some key terms, concepts and equations on secondary migration and entrapment of petroleum, based on the published researches. They will be used throughout this thesis. Some of the issues are still in debate, and for those the author would like to define his position because they are the basic assumptions for the rest of this research.

Definition of secondary migration of petroleum is given first, followed by the mode of secondary migration, mechanism and governing equations of migration and entrapment. Then methods of numerical modelling of petroleum migration are outlined.

2.1 Definition of secondary migration

Secondary migration is generally defined as the movement of petroleum fluids (oil and/or gas) expelled from source rocks, through porous and permeable carrier or reservoir rocks to commercial accumulations or traps (Tissot and Welte, 1984, p.294; **Figure 2.1a**). The movement within the source rocks, on the other hand, is termed primary migration. According to that definition, the difference of secondary migration from primary migration lies on the grain size and possibly wettability of the porous media, in addition to *in situ* petroleum generation in the source rocks. That is, source rocks are fine-grained (mudstone or fine-grained carbonate) and may be oil-wet, while carrier or reservoir rocks are coarse-grained (sandstone or porous carbonate) and usually water-wet though some carbonate reservoirs are reported to be oil-wet (*e.g.* Lucia, 1999). It is those differences in the rocks that cause the difference in flow mechanism between primary and secondary migration.

Secondary migration, however, does not necessarily occur in coarse-grained rocks, as simplified in **Figure 2.1a**. Sedimentary sequences in reality are much more complex and generally coarse-grained carrier beds are not continuous from the kitchens (matured source rocks) to the accumulations but separated by finer-grained rocks, *i.e.* mudstones or fine-grained carbonates (**Figure 2.1b**). Even if petroleum can migrate through a continuous carrier from its kitchen to a trap, the excess amount of petroleum that can not be retained by the sealing capacity of the trap should leak vertically up through the fine-grained seal rocks. This leakage should also be termed secondary migration, though some authors call it "tertiary migration" (Tissot and Welte, 1984). Therefore, secondary migration is more correctly defined as "any movement (of petroleum fluids) outside the matured source rock"

(Hunt, 1995, p.238), regardless of the grain size of the porous media. According to this definition, which is adopted in this thesis, too, the only possible difference between the primary and secondary migration in terms of flow mechanism is wettability of the media.

In this thesis, the author would like to focus on a close examination of secondary migration and entrapment of petroleum fluids at interfaces of sandstones and mudstones.

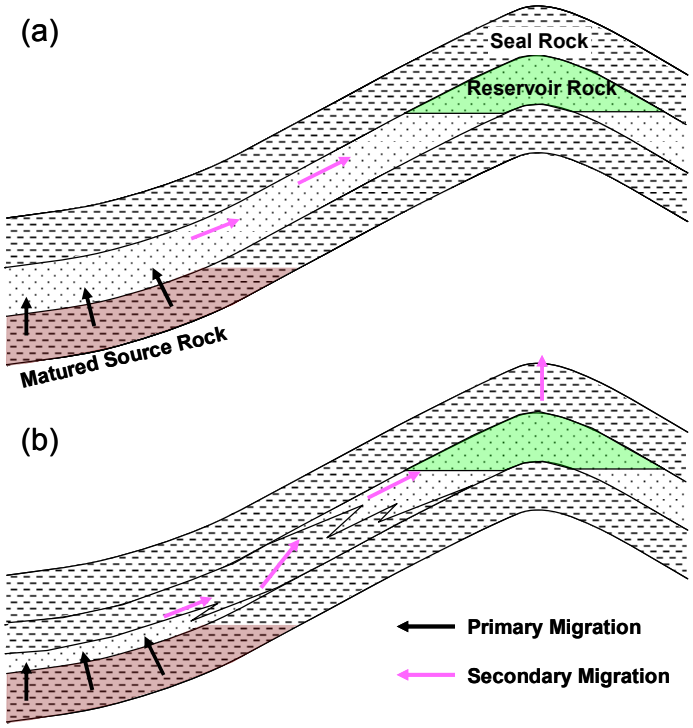

Figure 2.1 Definitions of secondary migration by (a) Tissot and Welte, 1984 and (b) Hunt, 1995.

2.2 Mode of secondary migration

It is widely accepted that petroleum expelled from source rocks migrates through carrier rocks in separate phase, rather than in solution in formation water or other modes (Tissot and Welte, 1984; England *et al.* 1987; Hunt, 1995). The reasons for this include: (1) water has very low solubility of petroleum and (2) there is little relationship in solubility-dependent fractionation of petroleum in source rocks and reservoirs.

In this research, it is assumed that petroleum migrates through water-wet rocks in discrete petroleum phase. If this assumption is not valid in any possibility, the conclusions from this work should be revised.

2.3 Governing equations of secondary migration

The movement of petroleum fluids in porous media is expressed by the combination of multi-phase Darcy's law and the conservation of mass. In this section, this widely-accepted mechanics of secondary migration of petroleum in water-wet porous media is summarized first, based mainly on Hubbert (1953), England *et al.* (1987) and Ingebritsen *et al.* (2006). Then limitation or potential problem of using Darcy's law for secondary migration modelling will be reviewed.

2.3.1 Fluid potential as the driving force of secondary migration

The driving force F experienced by a unit volume of fluid is given by the gradient of the fluid potential Φ_f, assuming frictionless process:

$$F = -\nabla \Phi_f \tag{2.1}$$

where:

$$\nabla = \begin{pmatrix} \frac{\partial}{\partial x} \\ \frac{\partial}{\partial y} \\ \frac{\partial}{\partial z} \end{pmatrix}$$

The negative sign of equation 2.1 indicates that the driving force is in the direction of decreasing the fluid potential.

The fluid potential is defined as the work necessary to move unit volume of fluid from the datum level (*i.e.* sea level or water table) to the depth of interest. The potentials for incompressible (*i.e.* fluid density is constant) water and petroleum are:

$$\Phi_w = P - \rho_w \cdot g \cdot z \tag{2.2}$$

$$\Phi_p = P - \rho_p \cdot g \cdot z + 2\gamma_{pw} \cdot \cos\theta_{pw} \cdot \left(\frac{1}{r_t}\right) \tag{2.3}$$

where

Φ [Pa]: fluid potential. Subscripts w and p refer to water and petroleum, respectively

P [Pa]: pore water pressure

ρ [kg/m^3]: fluid density. Subscripts w and p refer to water and petroleum, respectively

g [m/s2]: acceleration due to gravity, 9.80665 m/s^2

z [m]: depth below the datum elevation (z increases as depth increases)

γ_{pw} [N/m]: interfacial tension between petroleum and water

θ_{pw} [rad]: contact angle between petroleum and rock

r_t [m]: pore-throat radius of the rock

Substituting equation 2.2 into 2.3 gives:

$$\Phi_p = \Phi_w + \left(\rho_w - \rho_p\right) \cdot g \cdot z + 2\gamma_{pw} \cdot \cos\theta_{pw} \cdot \left(\frac{1}{r_t}\right) \tag{2.4}$$

The first term of the right-hand side of equation 2.4 is known as excess pressure or overpressure. The second and third terms are buoyancy and capillary pressure, respectively.

The driving force for secondary migration of petroleum is derived by differentiating equation 2.4:

$$F = -\nabla\Phi_w - \left(\rho_w - \rho_p\right) \cdot g - 2\gamma_{pw} \cdot \cos\theta_{pw} \cdot \nabla\left(\frac{1}{r_t}\right) \tag{2.5}$$

In a hydrostatic condition, $\nabla\Phi_w = 0$ at any position and equation 2.5 becomes

$$F = -\left(\rho_w - \rho_p\right) \cdot g - 2\gamma_{pw} \cdot \cos\theta_{pw} \cdot \nabla\left(\frac{1}{r_t}\right) \tag{2.6}$$

In coarse-grained reservoir rocks where capillary pressure term is safely neglected, equation 2.5 becomes

$$F = -\nabla\Phi_w - \left(\rho_w - \rho_p\right) \cdot g \tag{2.7}$$

In fine-grained rocks, however, the capillary term becomes significant because it is inversely proportional to pore-throat radii. More explanation on the capillary effects will be made in section 2.4.1.

2.3.2 Flow rate of secondary migration

Flow of single incompressible fluid in porous media is quantified experimentally by Darcy's law in which the flow rate is linearly related to the gradient of fluid potential:

$$q_f = -\frac{k}{\mu}\nabla\Phi_f \tag{2.8}$$

where

q_f [$m^3/m^2/s$]: Darcy's velocity defined as volume flux of fluid passing across unit area of the rock per unit time

k [m^2]: absolute or intrinsic permeability tensor

μ [Pa.s]: fluid viscosity

In multiphase flow systems of immiscible fluids, Darcy's law is still used traditionally by applying the following modification.

$$q_p = -\frac{k_{rp}k}{\mu_p}\nabla\Phi_p \tag{2.9}$$

where

k_r [m^2/m^2]: relative permeability. Subscript p refers to petroleum.

2.3.3 Governing equation of fluid flow

Governing equations of fluid flow are derived by combining Darcy's law with the conservation of mass. Change in fluid mass of a unit volume of porous medium for a certain time interval must be equal to the mass influx and outflow, according to the law of conservation of mass (**Figure 2.2**).

$$\Delta Mass = Mass_{in} - Mass_{out} \tag{2.10}$$

That is,

$$\begin{aligned}\Delta\left(\phi\rho_f \Delta x\Delta y\Delta z\right) = {} & \rho_f q_x\left(x-\frac{\Delta x}{2},y,z\right)\Delta y\Delta z\Delta t + \rho_f q_y\left(x,y-\frac{\Delta y}{2},z\right)\Delta x\Delta z\Delta t \\ & + \rho_f q_z\left(x,y,z-\frac{\Delta z}{2}\right)\Delta x\Delta y\Delta t - \rho_f q_x\left(x+\frac{\Delta x}{2},y,z\right)\Delta y\Delta z\Delta t \\ & - \rho_f q_y\left(x,y+\frac{\Delta y}{2},z\right)\Delta x\Delta z\Delta t - \rho_f q_z\left(x,y,z+\frac{\Delta z}{2}\right)\Delta x\Delta y\Delta t\end{aligned} \tag{2.11}$$

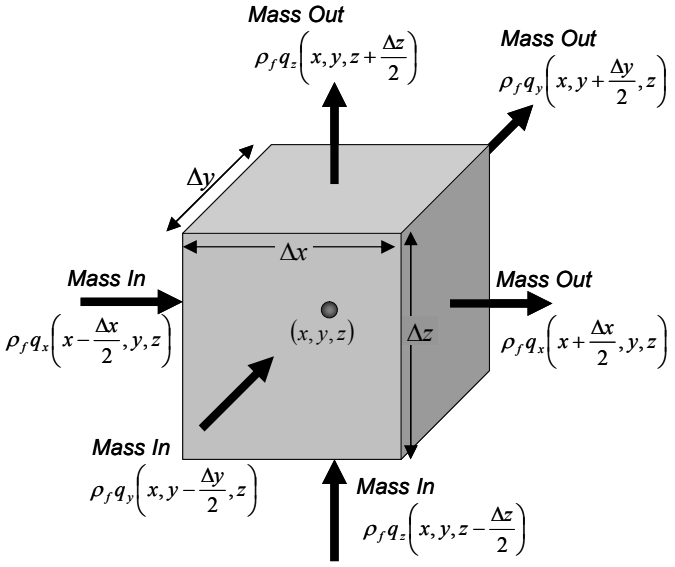

Figure 2.2 Conservation of mass on representative element volume.

Rearranging equation 2.11 and taking the limit as Δx , Δy , Δz and $\Delta t \to 0$ gives

$$\frac{\partial\left(\phi\rho_f\right)}{\partial t} + \nabla\left(\rho_f q_f\right) = 0 \tag{2.12}$$

This is known as the continuity equation for fluid flow through porous media.

By invoking the Darcy's law appropriate for a single incompressible fluid, equation 2.12 becomes

$$\frac{\partial(\phi\rho_f)}{\partial t} = \nabla\left(\frac{k\rho_f}{\mu_f}\nabla\Phi_f\right) = \nabla\left[\frac{k\rho_f}{\mu_f}(\nabla P + \rho_f g\nabla z)\right] \quad (2.13)$$

This is the fundamental fluid flow equation and known as the diffusion equation. Under steady-state (or equilibrium) conditions, the left-hand side of equation 2.13 becomes zero, and it reduces to:

$$\nabla\left(\frac{k\rho_f}{\mu_f}\nabla\Phi_f\right) = \nabla\left[\frac{k\rho_f}{\mu_f}(\nabla P + \rho_f g\nabla z)\right] = 0 \quad (2.14)$$

known as the Laplace's equation.

For the multiphase water-oil-gas system, by introducing saturation and relative permeability variables and capillary term, the flow equations become:

$$\frac{\partial(\phi S_w\rho_w)}{\partial t} = \nabla\left[\frac{k_{rw}k\rho_w}{\mu_w}(\nabla P_w + \rho_w g\nabla z)\right] \quad (2.15)$$

$$\frac{\partial(\phi S_o\rho_o)}{\partial t} = \nabla\left[\frac{k_{ro}k\rho_o}{\mu_o}(\nabla P_o + \rho_o g\nabla z)\right] \quad (2.16)$$

$$\frac{\partial\left[\phi(S_g\rho_g + S_o\rho_o G_f)\right]}{\partial t} = \nabla\left[\frac{k_{rg}k\rho_g}{\mu_g}(\nabla P_g + \rho_g g\nabla z)\right] + \nabla\left[\frac{k_{ro}k\rho_o G_f}{\mu_o}(\nabla P_o + \rho_o g\nabla z)\right] \quad (2.17)$$

$$P_{cow} = P_o - P_w = f(S_o, S_w) \quad (2.18)$$

$$P_{cgo} = P_g - P_o = f(S_g, S_o) \quad (2.19)$$

$$S_w + S_o + S_g = 1 \quad (2.20)$$

where

G_f [kg/kg]: fraction of gas dissolved in oil

S [frac]: fluid saturation.

P_c [Pa]: capillary pressure. Subscripts *ow* and *gw* refer to oil-water and gas-water, respectively

Fluid flow equations 2.15 to 2.20 can be solved analytically for rather simple problems (Carslaw and Jaeger, 1959). However, for more complex problems involving heterogeneous and anisotropic rock properties and variable fluid properties, numerical solutions are necessary.

2.3.4 Limitations of Darcy's law

It is generally accepted that Darcy's law is applicable when inertial forces are negligible in comparison to pressure gradient and viscous forces, *i.e.* the Reynolds number R_e is small (Mavko *et al.* 1998; Ingebritsen *et al.* 2006).

$$R_e = \frac{\rho q l}{\mu} \quad (2.21)$$

It means that there is an upper limit of flow rate q, and Darcy's law is applicable only to laminar flow in relatively low flow regime and not to turbulent flow in high flow regime. Above the threshold flow rate, significant amount of energy is lost to turbulence and Darcy's law overpredicts the flow rate (Ingebritsen *et al.* 2006). The term "low" or "high" here is used in the viewpoint of the production time scale, and fluid (water) flow on the geological time scale obviously falls in the "low" flow regime because of its extremely low flow rate q in most geological settings. Ingebritsen *et al.* (2006) estimated the flow rate where Darcy's law fails as $q > 6 \times 10^{-3}$ m/s or 2×10^{5} m/yr for water flow in coarse-grained sandstone, which is extremely high compared with fluid flow on the geological time scale ($q < 4$ m/yr; Catalan *et al.* 1992).

On the other hand, some authors mention a minimum pressure gradient below which there is little flow and the Darcy velocity may again be systematically overestimated (Neuzil, 1986, 1995; Mavko *et al.* 1998; Ingebritsen *et al.* 2006). That is, there is the lower limit of flow rate in which Darcy's law is applicable (but see Dewhurst *et al.* 1999 for opposite opinion). Non-Darcian behaviour below this pressure gradient has been attributed to streaming potentials in fine-grained soils, immobile adsorbed water layers, and clay-water interaction, giving rise to non-Newtonian fluid viscosity (Mavko *et al.* 1998). This might be significant for properly formulating water flow in mudstones on geological time scale.

In multiphase flow systems, the problem becomes more complex. Firstly, the capillary term of equation 2.5 can cause non-linear flow behaviour when the flow is extremely slow, which is inconsistent with Darcy's law (England *et al.* 1987, Fig.9). Secondly, and to be fatal, petroleum migration in the geological time scale must be capillary-dominated flow, not viscous-dominated flow (England *et al.* 1987; Carruthers, 1998; Tokunaga *et al.* 1998b). If it is the case, Darcy's law assuming bulk flow of petroleum in porous media may not be applicable. This will be further discussed in the next section.

2.3.5 Viscous-dominated versus capillary-dominated flow

Nature of petroleum migration or multiphase flow in general, is controlled by the relative magnitude of three forces: gravity, capillary and viscous forces. It can be expressed in terms of the capillary number and bond number (Wilkinson, 1984). The capillary number C_a is the ratio of viscous to capillary forces and defined as:

$$C_a = \frac{\mu_p \cdot q_p}{\gamma_{pw} \cos\theta_{pw}} \tag{2.22}$$

where

μ_p [Pa.s]: dynamic viscosity of petroleum

q_p [m³/ m²/s]: flow rate of petroleum fluid

γ_{pw} [N/m]: interfacial tension between petroleum and water

θ_{pw} [rad]: contact angle between petroleum and rock

The bond number B_o is the ratio of gravity to capillary forces and defined as:

$$B_o = \frac{(\rho_w - \rho_p) \cdot g \cdot a^2}{\gamma_{pw} \cos \theta_{pw}} \tag{2.23}$$

where

a : characteristic length scale (pore throat radius)

ρ [kg/m³]: fluid density. Subscripts w and p refer to water and petroleum, respectively

g [m/s²]: acceleration due to gravity, 9.80665 m/s²

The relative importance of viscous and capillary forces is assessed by the capillary number, and it is controlled by the flow rate as shown in equation 2.22. If the flow rate is relatively high (C_a is large), viscous pressure gradient has significant influence on the flow mechanism. In this viscous-dominated flow regime, stable displacement of petroleum fluids occurs (Lenormand *et al.* 1988; Carruthers, 1998; Tokunaga *et al.* 2000). It characterizes the petroleum flow on the production time scale. If, on the other hand, the flow rate is relatively low (C_a is small), viscous pressure gradient becomes negligible and capillary and gravity forces dominate. In this capillary-dominated flow regime, capillary-fingering displacement of petroleum fluids occurs (Lenormand *et al.* 1988; Tokunaga *et al.* 2000).

The question is if the petroleum migration falls in the viscous-dominated flow regime or the capillary-dominated flow regime. England *et al.* (1987) estimated the capillary number for petroleum migration both in sandstone and mudstone, assuming the Darcian flow of petroleum[*1]. They concluded that "the capillary number is never greater than 10^{-10}: capillary forces therefore dominate at all times."

2.4 Mechanism of entrapment

Petroleum migrating through carrier beds may form accumulations when it reaches trapping structures. Two requirements should be met for the trapping structures, *i.e.* trapping geometry of the reservoir rocks and sealing capacity of the cap rocks. The trapping geometry includes anticlines (4-way dip closures), faulted structures (fault traps), lithology changes (stratigraphic traps), *etc.* Sealing capacity is determined by capillary pressure, though hydrodynamic pressure gradient may affect the capacity in hydrodynamic conditions. Some researchers insist the importance of "pressure seals" for

[*1] It may not appropriate to apply the Darcy's law to obtain the petroleum flow rate, but it will at least tell us the maximum capillary number, because Darcy's velocity systematically overestimates the flow rate.

another mechanism of sealing (Bradley, 1975; Hunt, 1990; Bradley, and Powley, 1994), which has caused confusions on the study of sealing mechanism of petroleum for the last decades.

This thesis concentrates on the sealing capacity of traps, not the geometry, *i.e.* all the discussion throughout the thesis is for "capillary-limited traps" in the sense of Nakayama and Sato (2002). In this section, capillary effects are outlined first as the main mechanism of the sealing. Then hydrodynamic effects are shown as the deflecting force of capillary-buoyancy equilibrium. Finally the concept of "pressure seal" is introduced from a critical viewpoint.

2.4.1 Capillary effects

As well documented in the classical articles *e.g.* Berg (1975) and Schowalter (1979), capillary pressure at interface between reservoir and seal rocks is the resistant force to prevent the petroleum from further migration and responsible for the accumulations.

Capillary pressure is defined as the pressure difference between the wetting phase and non-wetting phase across a curved interface (Leverett, 1941). In a water-petroleum-rock system, water is the wetting-phase while petroleum is the non-wetting phase, and the pressure of petroleum is higher than that of surrounding water. Petroleum-water capillary pressure P_{cpw} is given by:

$$P_{cpw} = P_p - P_w = 2\gamma_{pw} \cdot \cos\theta_{pw} \cdot \left(\frac{1}{r_t} - \frac{1}{r_p} \right) \tag{2.24}$$

where

γ_{pw} [N/m]: interfacial tension between petroleum and water

θ_{pw} [rad]: contact angle between petroleum and rock

r_t [m]: pore-throat radius of the rock

r_p [m]: pore radius of the rock

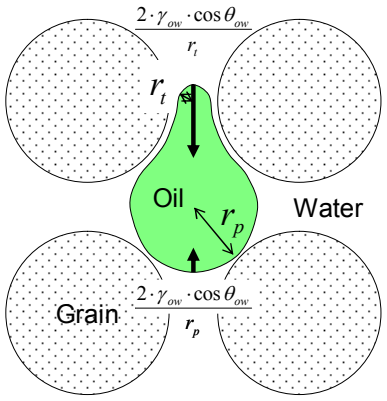

Figure 2.3 Schematic diagram showing capillary pressure in water-oil-rock system.

$$P_{cow} = 2 \cdot \gamma_{ow} \cdot \cos\theta_{ow} \cdot \left(\frac{1}{r_t} - \frac{1}{r_p} \right)$$

Table 2.1 Magnitude of capillary pressure for ideal rocks with rhombohedral packing of uniform spheres, applying Berg (1975) method.

Lithology	Grain size D		Pore radius r_p [mm]	Pore-throat radius r_t [mm]	Interfacial tension γ[N/m]	Contact angle θ[deg]	Capillary pressure P_c [kPa]	Density difference ⊿ρ[kg/m^3]	Oil column h_c [m]
	Φ	[mm]							
Sandstone	2	0.250	0.051750	0.019250	0.035	0	2.3	300	0.8
Siltstone	5	0.031	0.006469	0.002406	0.035	0	18.3	300	6.2
Mudstone	9	0.002	0.000404	0.000150	0.035	0	292.3	300	99.4
Sand-mud interface	2/9	0.25/0.002	0.051750	0.000150	0.035	0	464.1	300	157.8

This equation indicates that capillary pressure is a function of pore size, as well as of fluid properties. That is, capillary pressure increases with decreasing pore throat radius (**Figure 2.3**). Magnitude of capillary pressure for ideal sandstone and mudstone with rhombohedral packing of uniform spheres is shown in **Table 2.1**, applying Berg (1975) method:

$$r_p = 0.207 \cdot D \tag{2.25}$$

$$r_t = 0.077 \cdot D \tag{2.26}$$

where D is diameter of the grains. Largest capillary pressure is achieved at the interface between sandstone and mudstone, where the pore throat size r_t becomes smallest and the pore size r_p becomes largest.

Capillary threshold pressure P_{th} (or capillary displacement pressure) is defined as the pressure required to form a continuous filament of non-wetting fluid through the largest connected pore throats of the rock (Schowalter, 1979). **Figure 2.4** shows a schematic explanation of P_{th}. In capillary-limited traps, P_{th} must be equal to the buoyant pressure caused by the trapped petroleum column h_c.

$$P_{th} = 2\gamma_{pw} \cdot \cos\theta_{pw} \cdot \left(\frac{1}{r_t} - \frac{1}{r_p}\right) = \left(\rho_w - \rho_p\right) \cdot g \cdot h_c \tag{2.27}$$

Therefore, it is possible to estimate the maximum petroleum column height the seal rock can retain if the density of petroleum and water, interfacial tension and contact angle between petroleum and water, effective pore-throat radius of the seal rock, and effective pore radius of the reservoir rock are known.

$$h_c = \frac{2\gamma_{pw} \cdot \cos\theta_{pw}}{\left(\rho_w - \rho_p\right) \cdot g} \cdot \left(\frac{1}{r_t} - \frac{1}{r_p}\right) \tag{2.28}$$

As indicated in equation 2.25, P_{th} is dependent on fluids in the pores, not only on pore sizes of the rocks. It is thus useful to use P_{th} in mercury-air system as the general expression of sealing capacity of the rocks, to make it only a function of pore size. Conversion from petroleum-water system to mercury-air system is (Schowalter, 1979):

$$P_{thma} = \frac{\gamma_{ma} \cdot \cos\theta_{ma}}{\gamma_{pw} \cdot \cos\theta_{pw}} \cdot P_{thpw} \qquad (2.29)$$

where subscripts *ma* and *pw* indicate mercury-air and petroleum-water, respectively.

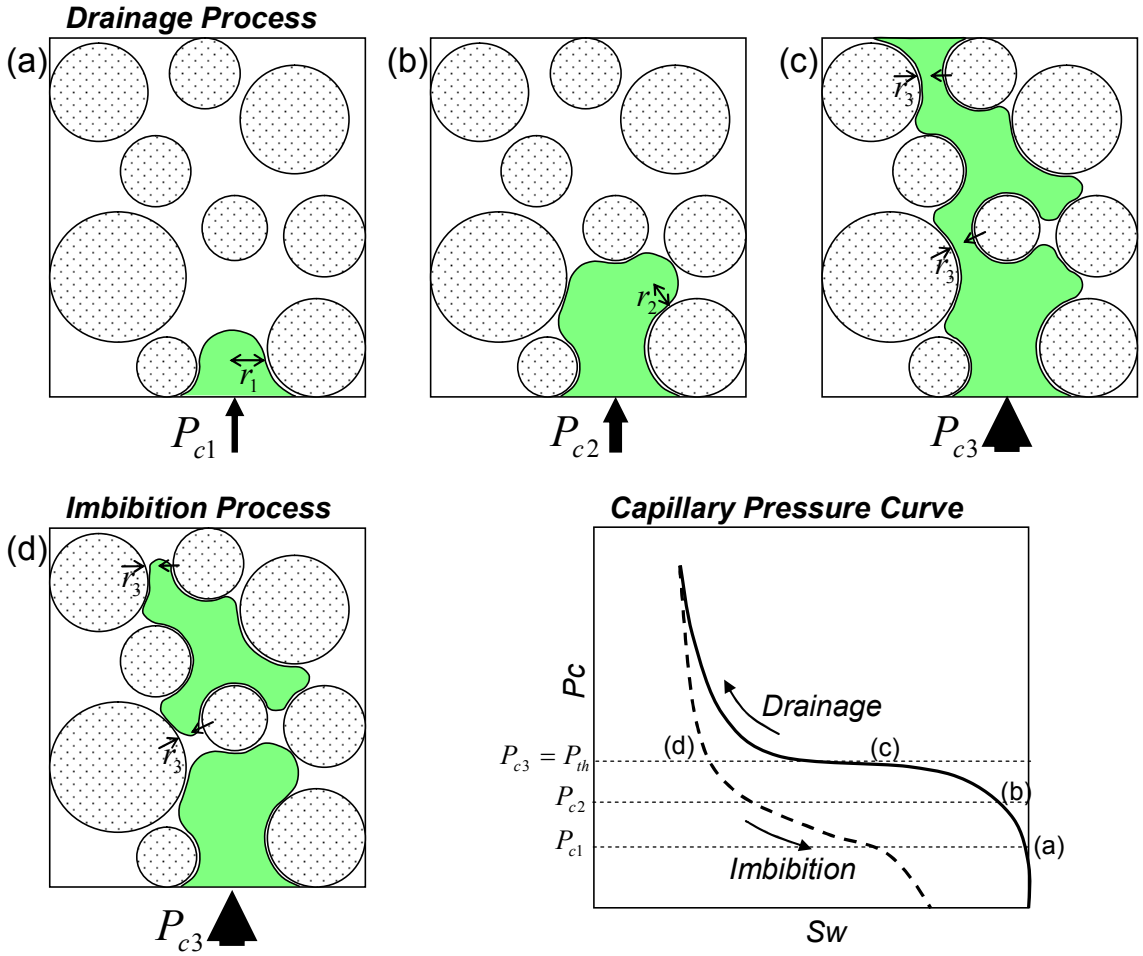

Figure 2.4 Capillary pressure P_c and capillary threshold pressure P_{th}. P_{th} is defined as the pressure required to form a continuous filament of non-wetting fluid through the largest connected pore throats of the rock (P_{c3}).

2.4.2 Hydrodynamic effects

The effects of hydrodynamics on petroleum migration and entrapment are first discussed by Hubbert (1953) and since then numerous authors have documented the hydrodynamic effects on both migration and entrapment from various parts of the world.

In hydrodynamic flow regime, $\nabla\Phi_w$ in equation 2.5 is not equal to zero, and petroleum will experience the additional force. Since this force is not necessarily vertical, it may result in non-vertical migration of petroleum in porous media. As the buoyancy term

in equation 2.5 is different for oil and gas, the two fluids may migrate in different directions to traps.

Furthermore, the hydrodynamics can affect petroleum entrapment by inclining petroleum-water contacts. They will dip in the direction of water flow given by (Hubbert, 1953; **Figure 2.5**):

$$\frac{dz}{dx} = \frac{\rho_w}{\rho_w - \rho_p} \cdot \frac{dh}{dx} \tag{2.30}$$

where,

dz/dx: slope of the petroleum-water contact

ρ [kg/m3]: fluid density. Subscripts w and p refer to water and petroleum, respectively

dh/dx: slope of the hydraulic head *h* in the horizontal direction *x*.

Since hydraulic head *h* is defined as:

$$h = \frac{\Phi_w}{\rho_w \cdot g} = \frac{P}{\rho_w \cdot g} - z \tag{2.31}$$

then equation 2.30 can be written as:

$$\frac{dz}{dx} = \frac{1}{(\rho_w - \rho_p) \cdot g} \cdot \frac{d\Phi_w}{dx} \tag{2.32}$$

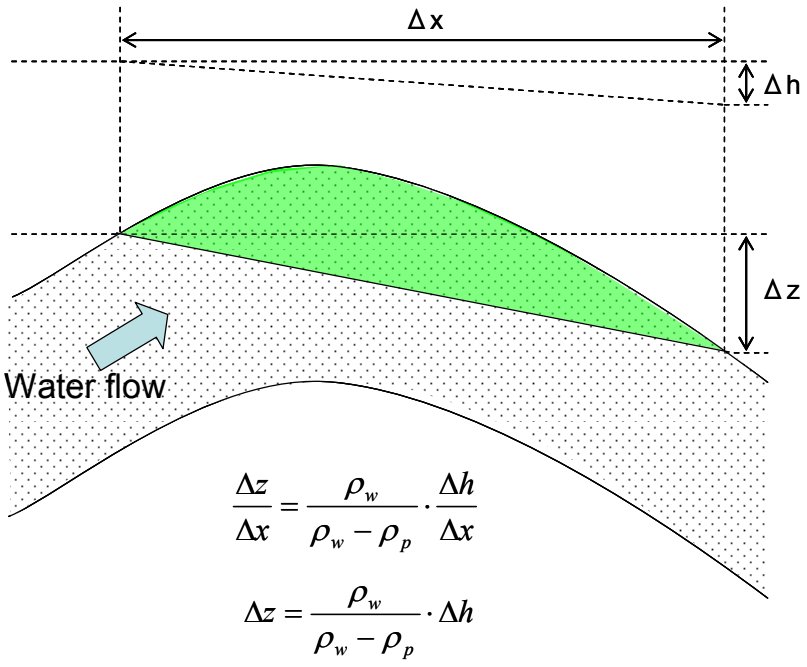

Figure 2.5 Hydrodynamic effect on petroleum accumulation, based on Hubbert (1953). Note that difference in hydraulic head Δh (difference in water potential) is taken for Δx, *i.e.* distance of the petroleum pool.

Note that Φ_w is the water potential and equal to the excess pressure P_{ex}, and thus $d\Phi_w/dx$ is the horizontal excess pressure gradient.

By using Darcy's Law (equation 2.8),

$$\frac{dz}{dx} = \frac{\mu_w \cdot q_w}{k_{rw} k \cdot (\rho_w - \rho_p) \cdot g} \tag{2.33}$$

That is, hydrodynamic effects are proportional to flow rate of water, and inversely proportional to permeability to water.

The hydrodynamic effects are reported from the areas where continuous recharge of meteoric water is suggested, *e.g.* the Powder River Basin, Wyoming (Hubbert, 1953), the Williston Basin, US and Canada (Hindle, 1997) or the Northwest shelf, Australia (Underschultz, 2005).

However, the hydrodynamic concepts are often extended *inadequately* as the modifier of sealing capacity of the cap rocks even in the area where a very small amount of water flow exists. It will be discussed in detail in the next chapter.

2.4.3 "Pressure seal"

The concept of pressure seal was first introduced by Bradley (1975), though he used the term "seal" instead of "pressure seal". The pressure seals refer to "seals that prevent essentially all pore fluid movement over substantial intervals of geologic time" (Hunt, 1990), and therefore are totally different from the capillary seals "that impede hydrocarbon movement but allow water to pass through" (Schowalter, 1979). They are "formed where the pore throats become effectively closed, *i.e.* the permeability approaches zero" (Bradley and Powley, 1994). They are often considered to form the boundaries of abnormally pressured compartments encountered in deeper part of various sedimentary basins.

It is true that there are plenty of examples of abnormal pressure or pressure compartments reported from all over the world (Law and Spencer, 1998). Some of the researchers attribute the cause of those abnormally pressured compartments to the existence of pressure seals (Hunt, 1990; Bradley and Powley, 1994; Takahata, 2004).

However, the concept of pressure seal has caused much debate because it contradicts the principles of hydrodynamics, which assume the inherent hydraulically continuous rock framework, *i.e.* there are no rocks with zero permeability (Toth *et al.* 1991; Bredehoeft *et al.* 1994; Neuzil, 1995). For hydrologists, abnormal pressures just mean that the time was too short, or pressure generation was too rapid to reach the equilibrium, *i.e.* for the pressure to dissipate to the hydrostatic level. Therefore, it seems outrageous to them to see it as static phenomena and to bring up impermeable pressure seals for explaining abnormal pressure compartments.

If we consider the abnormal pressures as hydrodynamic phenomena, as hydrologists do, and the author also, the keys are (1) the rate of pressure generation over geologic time and (2) permeability of the rocks (mostly of mudstones as they are predominant in sedimentary basins). Many researches addressed this issue and made quantitative estimation for those (Corbet and Bethke, 1992; Bredehoeft *et al.* 1994; Deming, 1994; He and Corrigan, 1995; Swarbrick *et al.* 2000; Lee and Deming, 2002; **Table 2.2**). Most of those works assume disequilibrium compaction as the main cause of pressure generation, and concluded that the permeability of as low as or less than a nano-Darcy is needed to maintain the abnormal pressure over substantial geologic time. Indeed, the main insistence from pro-pressure seal researchers is that the permeability of nano-Darcy order is not realistic. However, it *is* realistic based on the recent measurements of mudstone permeability (Neuzil, 1994; Schlomer and Krooss, 1997; Ingram *et al.* 1997; Lash, 2006; see next chapter for details). Furthermore, it should be noted that laboratory or well test measurements of extremely low permeability mudstones would be technically so difficult to obtain reliable permeability values.

Table 2.2 Published permeability estimation for abnormally pressured sediments.

Source	Type of Estimation	Area	Abnormal Pressure	Seal Age	Seal Lithology	Cause of Abnormal Pressure	Permeability [m2]	Permeability [mD]	Thickness [m]	Time Pressure Maintained [my]
Deming (1994)	Analytical solution for pressure dissipation						1.E-23 1.E-21	1.E-08 1.E-06	100 1000	1* 1*
He and Corrigan (1995)	Analytical solution for pressure dissipation						1.E-21 1.E-19	1.E-06 1.E-04	100 1000	1** 1**
Corbet and Bethke (1992)	Numerical simulation	Western Canada	N.A. (Underpressured)	Cretaceous	Mudstone	Unloading by erosion	< 3.E-20	< 3.E-05	500	3
Bredehoeft et al. (1994)	Numerical simulation	Uinta basin, Utah	0.8 of lithostatic	Tertiary	Mudstone	Oil generation	1.E-18 1.E-20	1.E-03 1.E-05	3000	0.1 10
Swarbrick et al. (2000)	Numerical simulation	Central North Sea	24 MPa	Cretaceous	Chalk	Disequilibrium compaction	1.E-21	1.E-06	450	3
Lee and Deming (2002)	Numerical simulation	Anadarko Basin, Oklahoma	0.4 to 0.8 of lithostatic	Cretaceous-Cenozoic	Mudstone	Disequilibrium compaction	<= 1.E-23 <= 1.E-21	<= 1.E-08 <= 1.E-06	10000 10000	200 200

*Time needed for the initial overpressure Po to dissipate to $0.16P_o$

**Time needed for the initial overpressure Po to dissipate to $0.1P_o$

If, on the other hand, there exist "pressure seals" or impermeable rock units surrounding the overpressured compartments in the deeper part of sedimentary basins (*e.g.* in matured source rocks), it means that those compartments are completely sealed off from any petroleum migration as they are bounded by perfect seals with infinite capillary threshold pressure. The idea is unlikely simply because source rocks and petroleum accumulations are generally in different pressure compartments, and the petroleum should migrate from one compartment to another to form accumulations, crossing the "pressure seals".

The author acknowledges that abnormal pressures are hydrodynamic phenomena,

because the static model (pressure seal model) seems physically inappropriate, if not "retrogressive" (Toth *et al.* 1991). Appreciating that any rock has finite permeability and hence finite capillary threshold pressure is one of the most fundamental principles adopted in this thesis in evaluating petroleum migration and entrapment, as well as in the field of hydrology.

2.5 Numerical modelling of petroleum migration and entrapment

Numerical modelling of petroleum generation, migration and entrapment, often termed "basin modelling" is a powerful tool to conduct the petroleum systems analysis deductively. Since Nakayama and van Sichlen (1981) and Welte and Yukler (1981) first tried basin modelling including secondary migration, significant progress has been made for the past quarter century (Hermanrud, 1993; Carruthers, 1998; Welte *et al.* 2000).

The main requirement for modelling petroleum migration and entrapment, in addition to its generation, is that it should handle 3D models, simply because migration occurs in three dimensional spaces which continuously change with time. It means dramatic increases both in the number of geologic inputs and in computation time. Recent application of 3D seismic data and advances in computer science enable it to be used not only for solving complex problems, but also as a predictive tool for further petroleum prospecting. Nevertheless, there still remain many to be solved or improved, *e.g.* finer resolution models with higher calculation speed, and the challenge to tackle with those continues. How the effect of abnormal formation pressure should be incorporated in the models is one of the unsolved problems, which is the main subject of this research.

In this section, methods for migration modelling are outlined first, and advantages and disadvantages for individual methods are listed. Some of the published application works are reviewed next, with emphasis on how they treated abnormal pressure, and on how they determined permeability and capillary threshold pressure in their models.

2.5.1 Methods of numerical modelling

Three methods are applied in oil industry to model petroleum migration: Darcy flow, ray-tracing and invasion percolation (Carruthers, 1998; Welte *et al.* 2000).

(1) Darcy flow method

Petroleum migration is formulated by the multi-phase Darcy's law (equation 2.9 in section 2.3.2) in this method (Welte and Yukler, 1981; Nakayama, 1987; Ungerer *et al.* 1990). Therefore, it can account for the flow rate of petroleum and it is the largest

advantage to other two methods. However, it is not clear if the Darcy's law properly describes petroleum migration at geological time scale, as mentioned in section 2.3.4. Another shortcoming of this method is in its slow calculation time. Models with millions of grid cells are not feasible to run, which limits practical use of this method.

(2) Ray-tracing method

Ray-tracing assumes that petroleum migrates upward along the steepest ridges of carrier beds due to buoyancy (Sylta, 1991; Childs *et al.* 2002b; 2002c). Since this method simply traces flow paths normal to backstripped depth contours of the carriers, it is much faster than the Darcy flow method. It can therefore handle extremely high resolution models with hundreds of millions of grid cells. Disadvantages of this method are that it does not calculate petroleum flow rate, pressure and other fluid properties, and that the carriers need to be pre-defined – which is not straightforward for complex geological settings.

(3) Invasion percolation method

Invasion percolation assumes that petroleum migration is overwhelmingly controlled by the balance between buoyancy and capillary forces (Carruthers, 1998). Without solving multi-phase Darcy's law, it can simulate extremely large models very fast, and still honours the principles of capillary sealing and leakage. It does not require the pre-defined carrier beds, but instead needs 3D capillary threshold pressure distribution. Predicting realistic threshold pressure distributions is the challenge to use this method. Disadvantage is same for the ray-tracing, *i.e.* it does not calculate petroleum flow rate, pressure and other fluid properties.

In this research, the invasion percolation method is used for simulating petroleum migration and entrapment. It is because that is the fastest method to simulate petroleum migration in extremely heterogeneous geological models. Calculation speed and capability of complex geology are of prime importance for practical purpose.

The effects of abnormal formation pressure are basically not incorporated in this method as it does not calculate formation pressure. It is considered to be a shortcoming if one tries to incorporate hydrodynamic effects or pressure seal mechanism. They are however to be discarded in this research at least for the effects on the sealing capacity, and therefore the invasion percolation is preferable method to others even from this point of view.

2.5.2 Review of published numerical modelling

(1) Effects of abnormal formation pressure

Most of the published case studies which use the Darcy flow method reckon pressure gradient as a driving force for petroleum migration in addition to the buoyancy and capillary forces. Thus abnormal formation pressure causes the "hydrodynamic effects" in those models (see the next chapter for detailed explanation of "hydrodynamic effects").

Nakayama (1987) described a 2D Darcy-based numerical modelling method and its application to the Iwafuneoki field, Japan. As reproduced in **Figure 2.6**, the oil and gas flow vectors are very similar to those of water which are controlled by overpressure (and permeability) distribution. The difference in flow directions for water, oil and gas is attributed to the buoyancy effect of oil and gas. The overall similarity of migration pathways to water flow patterns implies that the relative magnitude of the "hydrodynamic effect" is extremely high (similar order of magnitude) in his model.

Ungerer *et al.* (1990) described a 2D Darcy flow modelling method and its application to real fields by using Temispack, one of the most popular commercial simulators. By illustrating the North Sea example, they emphasized the importance of overpressure in water phase on seal efficiency. In their Figure 23, they explained that the overpressure in the cap rock enabled gas accumulation in underlying reservoir in the south-eastern half of the cross section, while the overpressure in the reservoir resulted in little gas accumulation and promoted vertical leakage through the cap rock in the north-western half of the section. That is, the "hydrodynamic effect" on sealing capacity of the cap rock seems very large in their model.

On the other hand, the ray-tracing and invasion percolation methods do not originally account for the "hydrodynamic effects" because they do not calculate formation pressure. Nevertheless, some studies use the water pressure data calculated outside those simulators, to incorporate the "hydrodynamic effects" in their models (*e.g.* Lothe *et al.* 2006; **Figure 2.7**).

(2) Permeability – capillary threshold pressure determination

Since abnormal formation pressure is closely related to low permeability, and permeability in turn has a negative correlation with capillary threshold pressure, simulation should be performed while keeping the k-P_{th} correlation to properly account for the effects of abnormal formation pressure on petroleum migration and entrapment. However, many simulations in the literature seem to determine k and P_{th} separately, causing a potential risk of loosing the correlation of the two key parameters (but see Ingram *et al.* 1997). As a consequence, the simulation results become questionable.

In Nakayama (1987), both k and P_{th} are related to lithology and porosity, but the former is determined as a function of the surface permeability and a constant whereas the latter is as pore-throat radius, both of which users assign arbitrary. That is, calibration of k, which uses pressure data, does not automatically affect that of P_{th}. It may loose the mutual correlation of the two parameters, and may misinterpret the relative magnitude of hydrodynamic and capillary forces.

If one uses the ray-tracing or invasion percolation to incorporate the "hydrodynamic effects", the pressure data must be imported from other Darcy flow simulators. This results in more risks for the k-P_{th} relationship to be destroyed.

In summary, the hydrodynamic effect on petroleum migration and entrapment seems very large in many published models. However, it is not clear if their results are real or just numerical artefact. That is, the questions are (1) if the "hydrodynamic effect" is geological fact, and if so, then (2) how large the effect is. In other words, they are the problems on the physical mechanism of the effect of abnormal pressure on petroleum migration and entrapment, and the parameter optimization to properly quantify it.

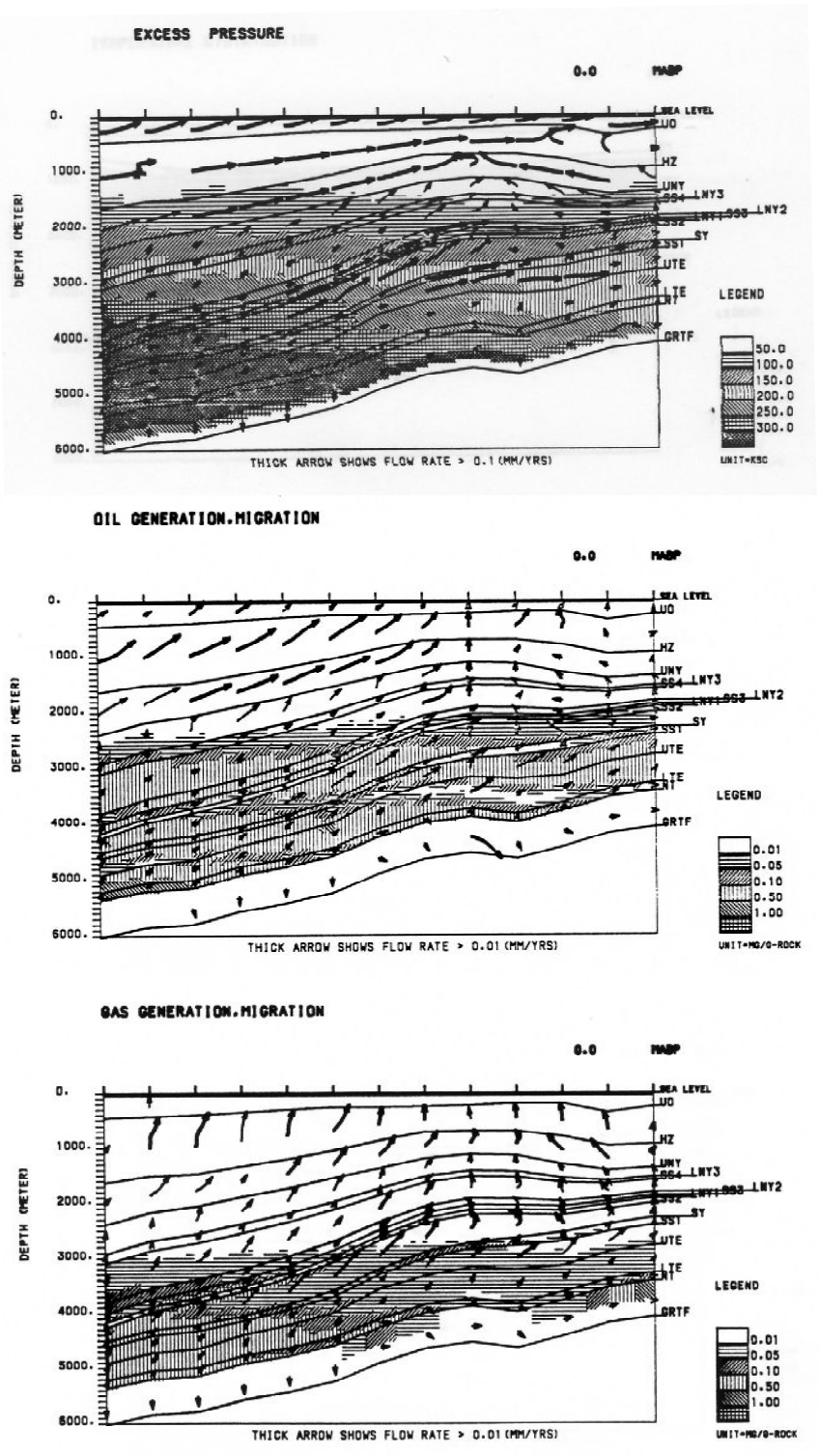

Figure 2.6 Present-day water, oil and gas flow rates in the Iwafuneoki field, Japan, simulated by Geopet II (Nakayama, 1987, reprinted by permission from the author). Oil and gas migration seems significantly affected by hydrodynamic flow of water. Note that gas flow vectors are more vertical than those of oil because of its larger buoyancy. Downward oil and gas flows in "GRTF" are due to the capillary effect, according to the author.

(a) Assuming Hydrodynamic Effect

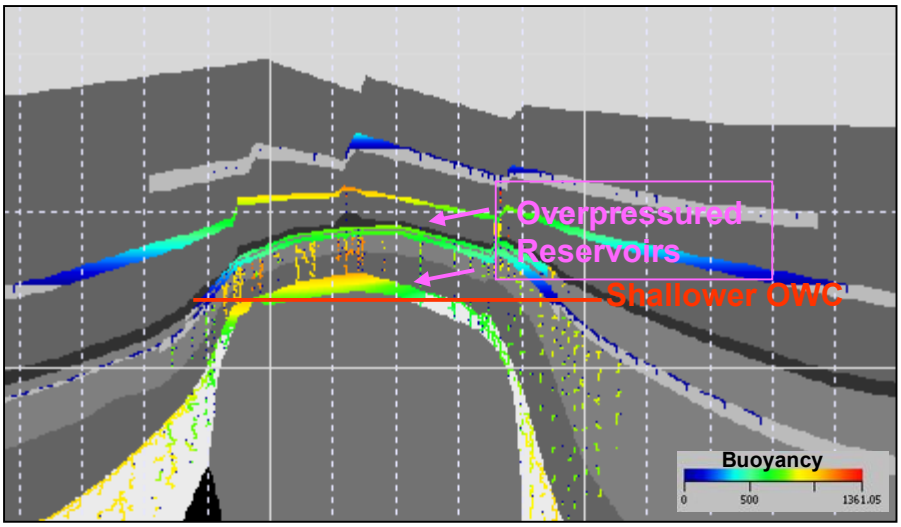

Sealing Capacity = Buoyancy + Overpressure

(b) Assuming No Hydrodynamic Effect

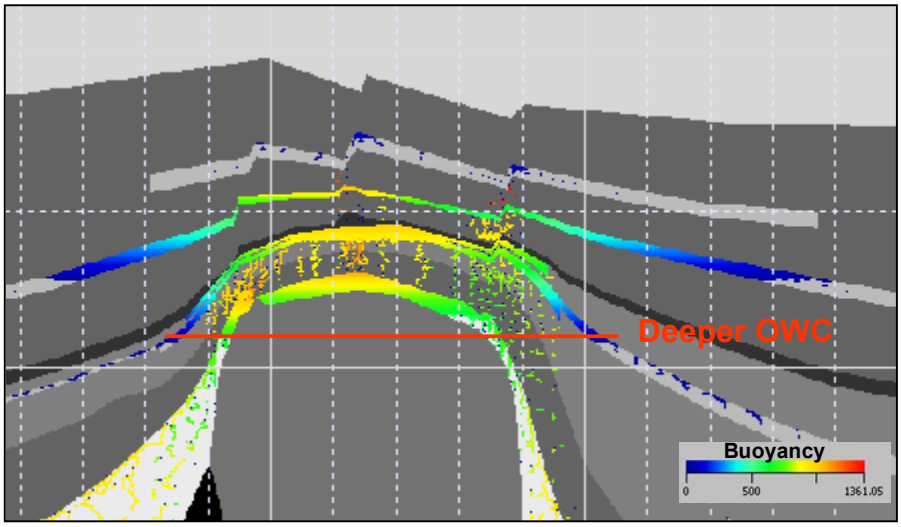

Sealing Capacity = Buoyancy

Figure 2.7 Impact of overpressure on migration simulation using MPath. Simulation results for identical geological model, with different assumption on the effect of overpressure. Note the difference in resultant capillary pressure (buoyancy) and column height of overpressured reservoirs (shown in arrows). Difference is also recognized in hydrostatic reservoirs at shallower depths, due to the difference in leakage from deeper reservoirs.

3 Examination of the effects of abnormal pressure in water phase on petroleum migration and entrapment

In this chapter, theoretical consideration on the effects of abnormal pressure in water phase in reservoirs on petroleum migration and entrapment is introduced first, to demonstrate that the abnormal pressure itself does not promote nor prevent the trapped petroleum to leak, as opposed to widely-accepted "hydrodynamic" effects. Attention will be focused on how large the viscous pressure drop in the water phase in a petroleum column is, which must be the factor controlling the magnitude of the hydrodynamic effects, and the author would like to illustrate that the pressure drop is practically negligible.

The effects of abnormal pressure on petroleum migration and entrapment had repeatedly been indicated by field examples from various part of the world. However, recent discoveries in overpressured compartments seem to prove the idea that abnormal pressure promote or prevent petroleum leakage may be invalid. In the second section in this chapter, field examples from the Niigata basin, Japan and the Norwegian continental shelf will be examined, which will support the author's position.

3.1 Theoretical consideration on the effects of abnormal pressure in water phase on petroleum migration and entrapment

3.1.1 Three different ideas on the effects of abnormal pressure on sealing capacity

It is generally believed that abnormal pressure in water phase in reservoirs will affect the petroleum column heights which the traps can hold. That will in turn, inevitably affect further migration of the petroleum leaked or spilled from those traps.

How the abnormal pressure may affect the sealing capacity is, however, still in debate. There are three different ideas (**Figure 3.1** and **3.2**):

(1) the abnormal pressure has no effect on sealing capacity,

(2) it increases or decreases sealing capacity by "hydrodynamic effect", or

(3) it acts as "pressure seal" to prevent any flow of both water and petroleum.

Researchers who emphasize the "hydrodynamic effects" insist that high pressure in the reservoirs decreases sealing capacity while high pressure in the seals increases it (**Figure 3.2**; model-2). On the other hand, if one acknowledges the "pressure seal" theory, the pressure difference in water phase always indicate the barrier to any fluid flow (both water and hydrocarbons), and implies higher sealing capacity (**Figure 3.2**; model-3).

In the following sections, validity of the former two ideas will be considered, because

the third one does not acknowledge physics of subsurface fluid flow and the author has already discarded it in Section 2.4.3.

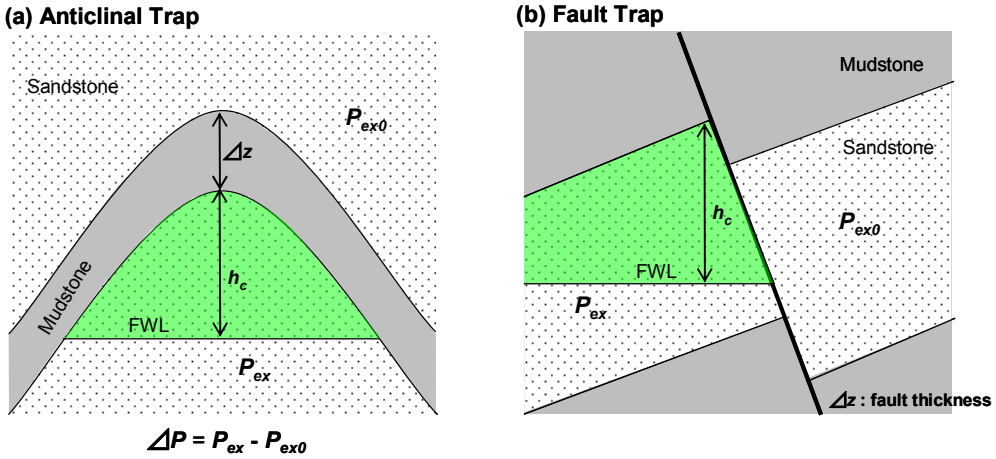

Figure 3.1 Schematic cross sections for (a) anticlinal and (b) fault traps. P_{ex} and P_{ex0} are excess pressure of the reservoir and adjacent aquifer, respectively.

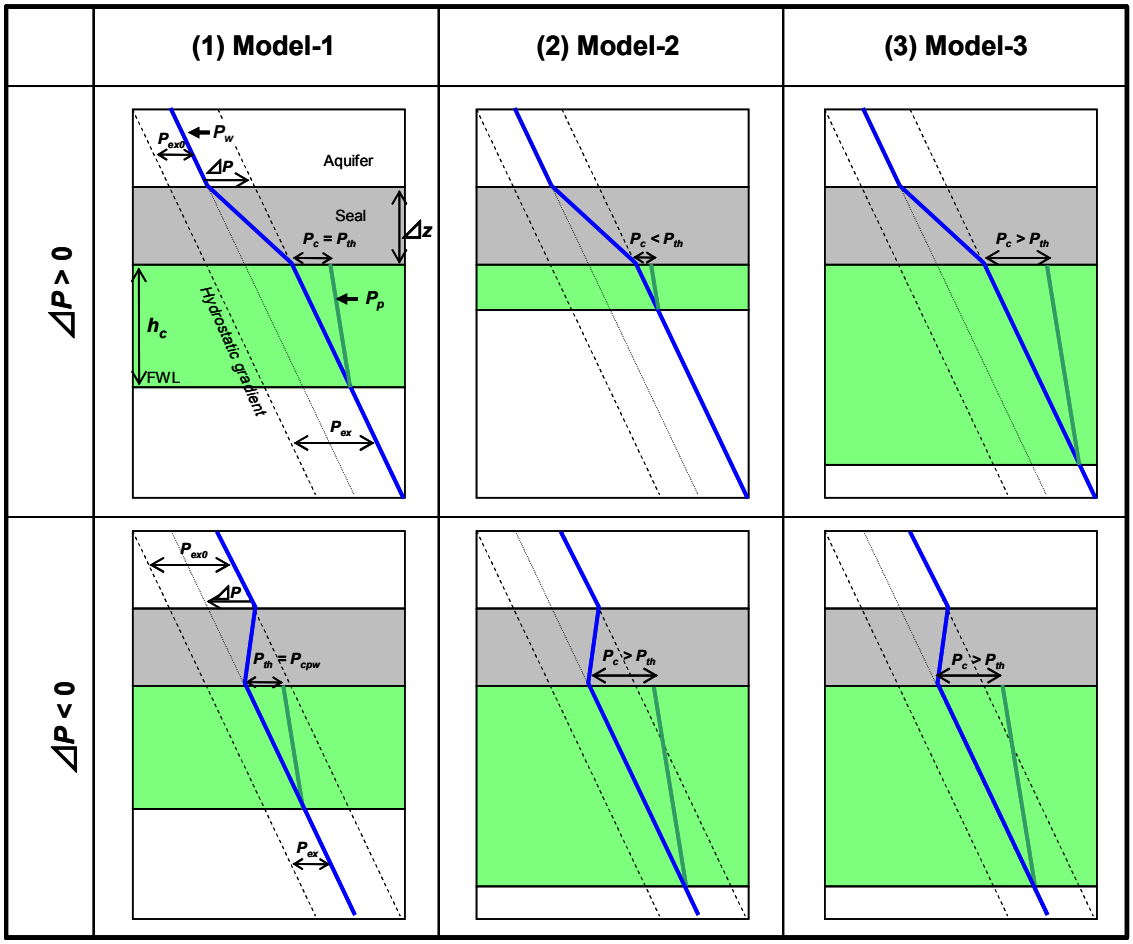

Figure 3.2 Schematic pressure profiles and petroleum column heights for the anticlinal trap shown in Figure 3.1(a), based on three different ideas on the effect of abnormal pressure in the water phase.

3.1.2 Inadequate extension of hydrodynamic concepts to assessment of sealing capacity

Hydrodynamic effects, originally introduced by Hubbert (1953), were basically to account for the effects of water flow *in reservoirs* on petroleum migration and entrapment (see Section 2.4.2). The two main hydrodynamic effects he pointed out are: (1) petroleum migration pathways may be deflected and (2) petroleum – water contacts may be inclined, because the petroleum equi-potential surfaces will be tilted downward in the water flow direction in reservoirs. Those situations occur only in the areas where water flows in rather high rate in the reservoirs by continuous recharge of meteoric water.

However, Hubbert's original concepts were *inadequately* extended in later works to the assessment of seal capacity where difference in water phase pressure between the reservoir and the seal (more correctly, adjacent reservoirs) is recognized (Clayton and Hay, 1994; Heum, 1996; Fristad *et al.* 1997). In those works, the pressure difference was considered to promote or prevent petroleum leakage from the traps. The idea was extensively used for assessing seal capacity in abnormally pressured reservoirs (*e.g.* Ungerer *et al.* 1990; Heum, 1996; Yielding *et al.* 1997; Olstad *et al.* 1997).

Bjorkum *et al.* (1998) was the first (at least to the author's knowledge) who recognized the problem in applying the hydrodynamic concepts to the assessment of seal capacity. They stated that "…any overpressure in a water-wet reservoir will not contribute to pushing the hydrocarbons through a water-wet seal, and overpressured water-wet reservoirs should therefore not be considered more prone to capillary leakage than normally pressured reservoirs". Although their conclusion seems reasonable to the author and some researchers (*e.g.* Teige *et al.* 2005), it was criticized in the discussions by Clayton (1999) and Rogers (1999), and many researchers still seem to support the *inadequate* extension of the hydrodynamic concepts (*e.g.* Yielding, 2002; Corcoran and Dore, 2002; Grauls *et al.* 2002).

3.1.3 Water phase pressure profile at reservoir-seal interface

The sealing capacity in hydrodynamic conditions is best investigated by drawing a pressure profile over the reservoir and overlying seal intervals in which the forces controlling the sealing capacity, *i.e.* the capillary pressure (or buoyancy) of petroleum P_c, threshold pressure of the seal P_{th} and the viscous pressure drop in water phase across the reservoir ΔP_r are clearly shown (**Figure 3.3**). In hydrodynamic conditions, those forces acting on the interface between the reservoir and seal are theoretically not in balance except in steady-state conditions, but practically they can be regarded as in balance even

in transient conditions because the flow of both water and petroleum is extremely slow and the change in condition must also occur extremely slowly (*i.e.* at geological time scale).

The most important point to investigate the force balance and hence the sealing capacity is how to determine the viscous pressure drop in the water phase ΔP_r. It should be the difference in the excess pressure (*i.e.* difference from the hydrostatic pressure gradient) across the petroleum column (*i.e.* between the free water level and the top of the petroleum column), because it must be the pressure drop where the petroleum phase is in pressure communication that can affect the sealing capacity. It should not be the difference over the seal interval (ΔP in **Figure 3.3**). It will be easily understood by reviewing Hubbert's original theory (**Figure 2.5**).

In the model proposed by Bjorkum *et al.* (1998) and refined in the replies to the discussions by Clayton and Rogers (Bjorkum *et al.* 1999a and 1999b), water in the reservoir is assumed to have a pressure gradient parallel to the hydrostatic gradient (**Figure 3.3a**). Since there is no viscous pressure drop across the petroleum column in their model, the sealing capacity for the abnormally pressured reservoir is the same as that for the normally pressured reservoir.

$$h_c = \frac{P_{th}}{(\rho_w - \rho_p) \cdot g} \tag{3.1}$$

where

h_c [m]: petroleum column height which the seal can hold

P_{th} [MPa]: capillary threshold pressure of the seal

ρ [kg/m^3]: fluid density. Subscripts w and p refer to water and petroleum, respectively.

g [m/s^2]: acceleration due to gravity, 9.80665 m/s^2

Clayton (1999) claimed in the discussion to Bjorkum *et al.* (1998) that the water phase is not continuous in the uppermost part of the oil column where water saturation is very low, and any excess pressure present in the reservoir can not be transmitted to the seal, and therefore the excess pressure in the reservoir will contribute to capillary leakage.

$$h_c = \frac{P_{th} - \Delta P}{(\rho_w - \rho_p) \cdot g} \tag{3.2}$$

where ΔP represents the excess pressure in the reservoir relative to the seal.

His idea, however, looks invalid because water permeability never becomes zero even in the uppermost part of the oil column where irreducible water saturation is reached and pressure transmission must occur in geological time scale (Bjorkum *et al.* 1999a; Rogers, 1999). Yet he did not show how large the water pressure is at the top of the petroleum column which, in author's opinion, is needed to determine the pressure drop across the petroleum column. Indeed, many other researches who are for the Clayton model (*e.g.* Heum, 1996) simply take the pressure difference between the abnormally pressured

reservoir and adjacent aquifers (ΔP) as the pressure drop term in equation 3.2 (**Figure 3.3b**). It is obviously incorrect as mentioned above, *i.e.* because at least some portion of ΔP is the pressure drop in the seal which should be removed from the equation.

Rogers (1999) in the discussion to Bjorkum *et al.* (1998) showed the correct pressure profile of the overpressured reservoir and the overlying seal (**Figure 3.3c**). Since it is the pressure drop across the petroleum column which can affect the sealing capacity, the correct formulation incorporating the hydrodynamic effects is:

$$h_c = \frac{P_{th} - \Delta P_r}{(\rho_w - \rho_p) \cdot g} \tag{3.3}$$

where ΔP_r is the viscous pressure drop across the petroleum column.

The question is, as Rogers (1999) pointed out, whether this pressure drop is significant or not. It will be further investigated in the following sections.

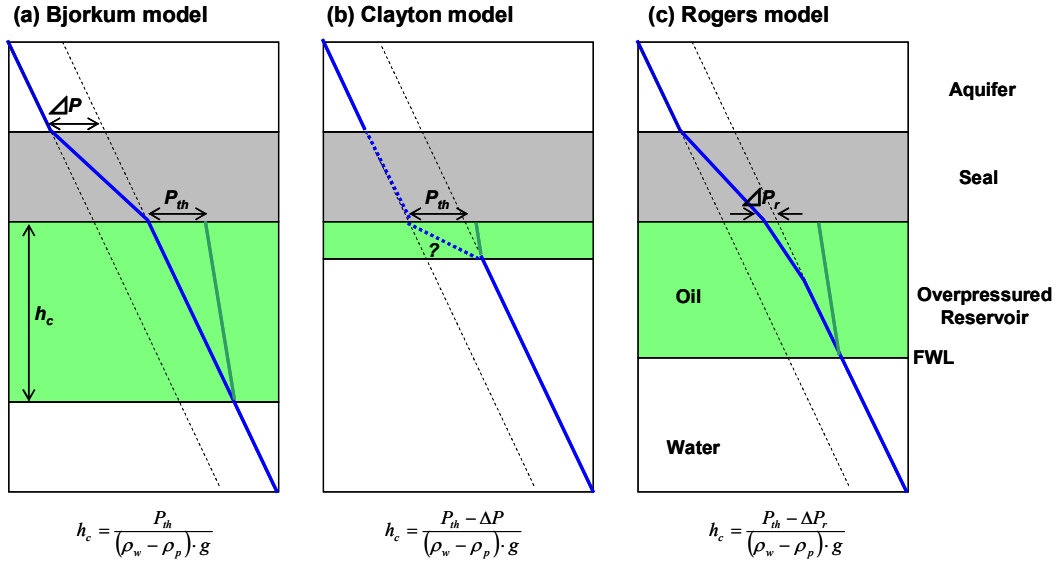

Figure 3.3 Schematic pressure profiles of overpressured reservoir and overlying seal illustrating three different models of water phase pressure profile at the interface of reservoir and seal.

3.1.4 Viscous pressure drop across petroleum column

As discussed in the previous section, it is viscous pressure drop across the petroleum column that matters for evaluating the hydrodynamic effects on sealing capacity of cap rocks.

Magnitude of viscous pressure drop in a petroleum column is proportional to the flow rate of water and inversely proportional to the effective permeability to water in the column. Provided water flows vertically, the flow rate of water in the petroleum column is

equal to that in the overlying seal, because of conservation of mass.

$$q_w = -\frac{k_{wr}}{\mu_w} \cdot \frac{\Delta P_r}{\Delta z_r} = -\frac{k_{ws}}{\mu_w} \cdot \frac{\Delta P_s}{\Delta z_s} \tag{3.4}$$

where:

q_w [m/s]: flow rate of water

k_w [m^2]: effective permeability to water. Subscripts r and s refer to reservoir and seal, respectively.

μ_w [Pa.s]: water viscosity

$\Delta P / \Delta z$ [Pa/m]: vertical pressure gradient. Subscripts r and s refer to reservoir and seal, respectively.

Therefore, ratio of pressure drop across the petroleum column and the seal is equal to the reciprocal of permeability ratio of in the petroleum column and the seal (Bjorkum *et al.* 1999b).

$$k_{wr} \cdot \frac{\Delta P_r}{\Delta z_r} = k_{ws} \cdot \frac{\Delta P_s}{\Delta z_s} \tag{3.5}$$

It means that if effective permeability to water in the petroleum column is sufficiently higher than that in the seal, pressure drop in the column is negligible.

Bjorkum *et al.* (1999b) and Teige *et al.* (2005) tried to quantify the effective permeability to water in petroleum columns by theoretical consideration and laboratory experiment, respectively.

Bjorkum *et al.* (1999b) made a theoretical estimation but they adopted a rather unique method, which makes their conclusion questionable. That is, they estimated the average thickness of the water films around sand grains in the petroleum column by using resistivity logs, and calculated water permeability from that average thickness and density of the films in the petroleum column, though estimation of those two parameters from any wireline logs is extremely difficult in the author's opinion. They concluded that effective permeability to water in the petroleum column is about 1.1 μD, which is much (1,000 to 10,000 times) larger than that in the seal and hence the pressure drop in the petroleum column is negligibly small.

Teige *et al.* (2005), on the other hand, carried out a laboratory experiment to examine the water flow through a petroleum column at irreducible saturation, by using a water-wet, highly permeable (1988 mD) core sample, oil-saturated to S_{wir}. They obtained the relative permeability to water of 0.71 μD in the oil column, which, they believe, is significantly higher than that in mudstones, and therefore supports the conclusion by Bjorkum *et al.* (1999b). Despite their conclusion, it is also questionable if the water permeability in the oil column is really much higher than that in mudstones, because they used an extremely permeable sample and applied only 0.5 MPa of capillary pressure, which is equivalent with

only a 150 m of oil column, in their measurement. They would obtain a smaller permeability value if they used a less permeable sample and applied more capillary pressure equivalent with naturally encountered oil column heights, *i.e.* several hundreds of meters.

3.1.5 Estimation of effective permeability to water in a petroleum column

Difficulty in quantifying relative permeability to water in a petroleum column is attributed to the lack of laboratory measurement at near irreducible water saturation. Generally relative permeability measurements apply too small pressure on non-wetting fluid to achieve the irreducible water saturation, *e.g.* 150 psi (1 MPa) of air pressure to water-saturated samples (CoreLab, 1982), which is equivalent with capillary pressure of only 150 m of oil column. That is why theoretical estimation is necessary like Bjorkum *et al.* (1999b).

Here the author would like to show an alternative estimation, which uses capillary pressure measurement data. Mercury injection capillary pressure (MICP) tests contrasts with relative permeability measurements in terms of magnitude of applying pressure. It can apply several hundreds MPa of mercury pressure, which is equivalent with several thousand meters of oil column and therefore sufficient to achieve the water saturation in the actual petroleum columns.

One of the simplest theoretical or semi-theoretical estimations of relative permeability to water in a petroleum column is to apply Purcell's equation, which relates permeability to capillary pressure by using Poiseuille's Law and capillary pressure equation (Purcell, 1949):

$$k = (\gamma \cos\theta)^2 F\phi \int_{S=0}^{S=1} \frac{dS_w}{(P_c)^2} \tag{3.6}$$

where:

k [m^2]: absolute permeability
γ [N/m]: interfacial tension
θ [rad]: contact angle
F : lithology factor (constant)
ϕ [frac]: porosity
S [frac]: wetting phase (water) saturation
P_c [Pa]: capillary pressure

The effective permeability to the wetting phase (water) is (Amyx *et al.* 1960):

$$k_w = (\gamma \cos\theta)^2 F\phi \int_{S=0}^{S=S_w} \frac{dS_w}{(P_c)^2} \tag{3.7}$$

Then, the relative permeability to water is (Amyx *et al.* 1960):

$$k_{rw} = \frac{k_w}{k} = \frac{\int_{S=0}^{S=S_w} \frac{dS_w}{(P_c)^2}}{\int_{S=0}^{S=1} \frac{dS_w}{(P_c)^2}} \tag{3.8}$$

That is, the relative permeability to water can be calculated from capillary pressure curve. Hence effective permeability to water across a column height can be estimated if the absolute permeability and capillary pressure measurements are available, and both of which are routinely measured.

Figure 3.4 shows an example of calculating effective permeability to water from mercury injection capillary pressure (MICP) measurement of a sandstone sample from the Iwafuneoki field, Japan (see Chapter 5 for details of the field). For this particular sample, effective permeability to water in an oil column is the order of μD. **Figure 3.5** shows estimated effective permeability to water in an oil column for total 12 sandstone core samples with absolute permeability ranging from 22 to 1,560 mD. From this figure, it is concluded that effective permeability to water in an oil column will range from 1.E-02 to 1.E-04 mD. Those figures roughly agree to the results of Bjorkum *et al.* (1999b) and Teige *et al.* (2005), despite all those three adopted different methods for the estimation.

3.1.6 Effects of abnormal pressure in water phase on petroleum migration and entrapment

Once the effective permeability to water in a petroleum column is estimated, the remaining unknown for quantifying the viscous pressure drop using equation 3.5 is the permeability of seal rocks. Although it can take a wide range of values (*e.g.* Neuzil, 1994), it must be less than *ca.* 1.E-05 mD to sustain substantial abnormal pressure for a certain interval of geologic time (**Table 2.2**). If one takes highest possible effective permeability to water of 1.E-05 mD for seal, the pressure drop in the column is only 0.000025 MPa/m or 0.01 MPa across a 400 m oil column for a typical sandstone reservoir, overlain by the seal with the pressure gradient of 0.025 MPa/m or 5 MPa over 200m of thickness (**Figure 3.6**). In this case, the pressure drop in the oil column is 1/1,000 of that in the seal.

According to the simple calculations shown here and those in Bjorkum *et al.* (1999b) and Teige *et al.* (2005), the pressure drop in the oil column is most probably negligibly small. Therefore, it will not reduce nor increase the petroleum column height in abnormally pressured reservoirs by the hydrodynamic effects. The water flow by the pressure drop is also too small to deflect the petroleum migration pathways even if it is not in the vertical direction. In conclusion, the idea that abnormal pressure in water phase in a

reservoir affects the petroleum migration and entrapment is “illusion”.

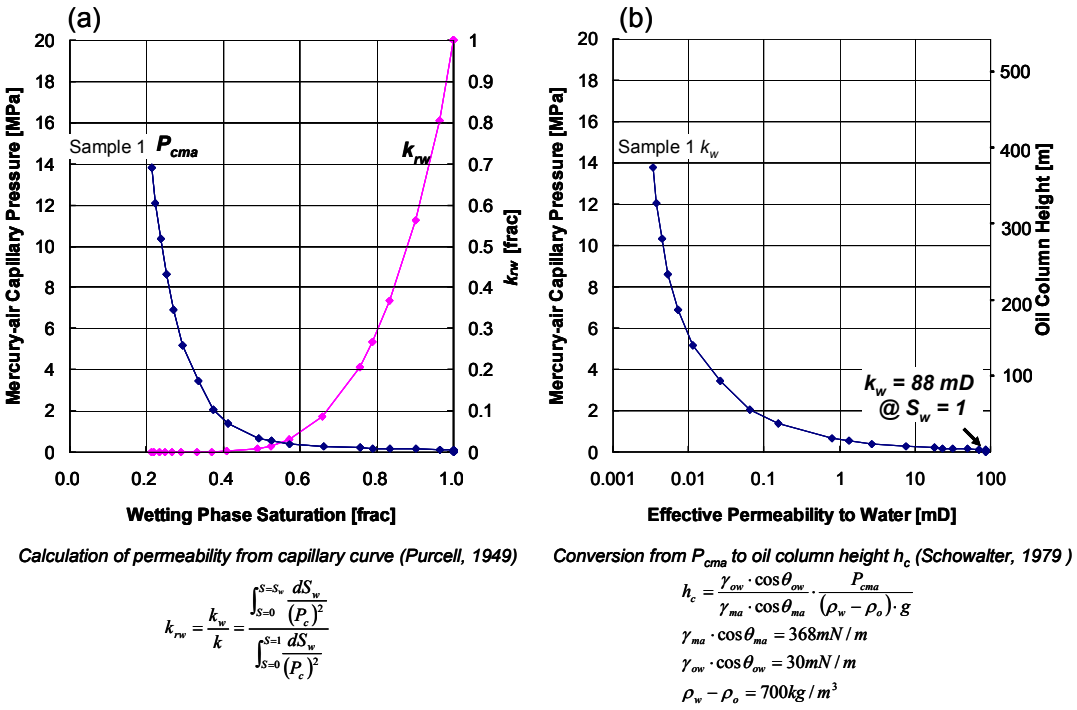

Figure 3.4 (a) Relative permeability to water calculated from mercury injection capillary pressure measurement for a sandstone core, Iwafuneoki field, Japan. (b) Effective permeability to water as a function of oil column height.

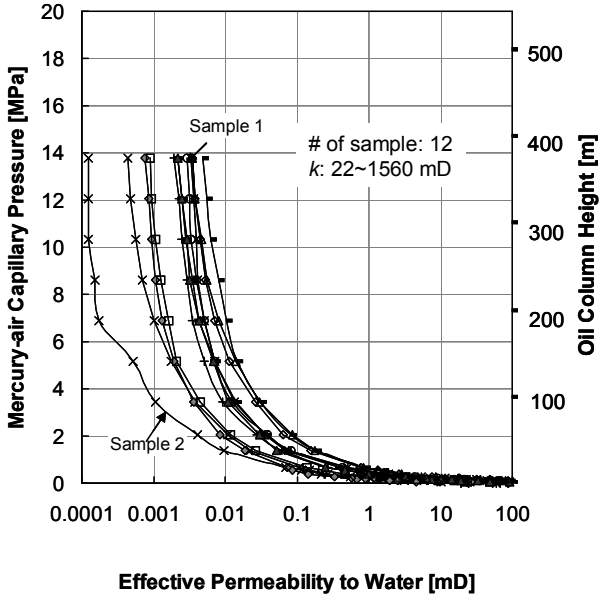

Figure 3.5 Estimated effective permeability to water as a function of capillary pressure, for sandstone cores from the Iwafuneoki field, Japan. Oil column height is for reference only (see Figure 3.4 for conversion from P_{cma} to h_c).

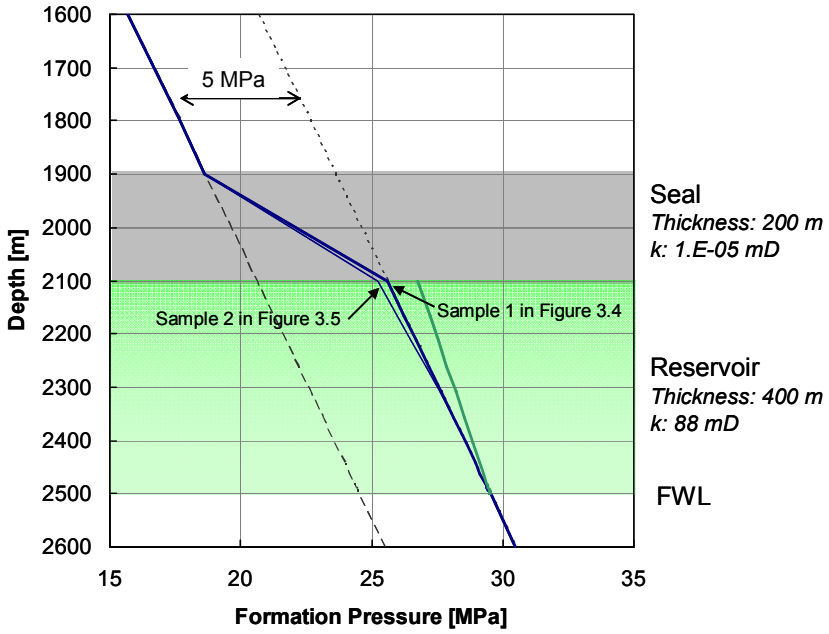

Figure 3.6 Water pressure profiles in an oil column. Excess pressure of 5 MPa is assumed. Permeability for the seal rock is assumed to be 1.E-05 mD. Effective permeability to water in the oil is estimated by using sandstone core samples from the Iwafuneoki field, Japan. The maximum pressure drop is 0.4 MPa across the 400 m of oil column for Sample 2 in Figure 3.5.

3.2 Hydrodynamic effects from field data

It has been reported that a strong association exists between abnormal formation pressure and economically significant petroleum accumulations (*e.g.* Law and Spencer, 1998). As mentioned in the previous section, the overpressure in water phase in reservoir rocks is often regarded as a negative factor to decrease the sealing capacity of the seal rocks. This idea was extensively used for reasoning of dry wells drilled in overpressured compartments (*e.g.* Ungerer *et al.* 1990; Heum, 1996; Olstad *et al.* 1997). All of them suggest weaker sealing capacity above the overpressured reservoirs from the context, though they literally claimed the possibility of hydrofracturing despite the actual formation pressures are lower than the leak-off pressures.

However, recent discoveries in overpressured compartments, *e.g.* the Kristin field and Morvin discovery in the Haltenbanken, offshore Norway (Norwegian Petroleum Directorate, 2008) and the Tune field, North Sea (Norwegian Petroleum Directorate, 2008; Childs *et al.* 2002a) indicate the idea that overpressure promote leakage may be invalid, as long as it does not exceed the hydrofracturing pressure.

In this section, the relationship between sealing capacity of seal rocks and abnormal

pressure in reservoir rocks will be examined by using actual oil / gas field data It will demonstrate that there is no relationship between proven petroleum column height and overpressure in water phase, both positively and negatively.

3.2.1 Example fields

Examples examined here consist of siliciclastics, *i.e.* seal rocks are mudstones or fault gouge clays, and include anticlinal, stratigraphic and fault traps from Niigata, Japan and the Norwegian continental shelf (**Table 3.1**, **Figure 3.7** and **3.8**). Formation pressure of those ranges from hydrostatic to severely overpressured, but none of them is underpressured. The requirements for evaluating sealing capacity: (1) they must be capillary-limited traps and (2) sufficient petroleum must be charged in those traps, are considered to be valid for all the example fields, from the regional knowledge of individual fields.

The column heights, fluid properties and formation pressure are from both published and unpublished data. Sources of individual data are listed in **Table 3.1**.

Table 3.1 List of oil / gas fields examined.

Basin	Field	Discovery	Fluids	Trap Type	Reservoir Age	Reservoir Lithology	Seal Lithology	Data Sources
Niigata	Higashi Niigata	1969	Gas and oil	Anticline	Miocene - Pleistocene	Sandstone	Mudstone	Saito et al. (2008), JAPEX unpublished
Niigata	Iwafuneoki	1984	Gas and oil	Stratigraphic	Pliocene	Sandstone	Mudstone	Saito et al. (2008), JAPEX unpublished
Haltenbanken	Åsgard	1981	Gas and condensate	Faulted anticline	Jurassic	Sandstone	Mudstone	Olstad et al. (1997), NPD (2008)
Haltenbanken	Kristin	1997	Gas and condensate	Faulted anticline	Jurassic	Sandstone	Mudstone	NPD (2008)
Haltenbanken	Morvin	2001	Gas and oil	Faulted	Jurassic	Sandstone	Mudstone	NPD (2008)
North Sea	Oseberg Syd	1984	Gas and oil	Fault	Triassic - Jurassic	Sandstone	Fault	Childs et al. (in press), NPD (2008)
North Sea	Tune	1996	Gas and oil	Fault	Jurassic	Sandstone	Fault	Childs et al. (2002a), NPD (2008)
North Sea	Gullfaks	1978	Oil	Faulted anticline	Triassic - Jurassic	Sandstone	Mudstone	Karlsson (1986), Heum (1996), Hesthammer et al. (2001), Childs et al. (2002c)

NPD: Norwegian Petroleum Directorate

(1) Higashi Niigata field, Niigata, Japan

The Higashi Niigata field (**Figure 3.7**), located in the central part of the Niigata basin, produces gas and condensate with some oil from multiple sandstone reservoirs of Miocene to Pleistocene age. It is an anticlinal trap, and column heights for the individual pools are controlled by sealing capacity of the overlying mudstones, because the free water levels for the pools are shallower than the structural spills and petroleum charge to the field must be sufficient based on a numerical simulation (Nakayama, 1981).

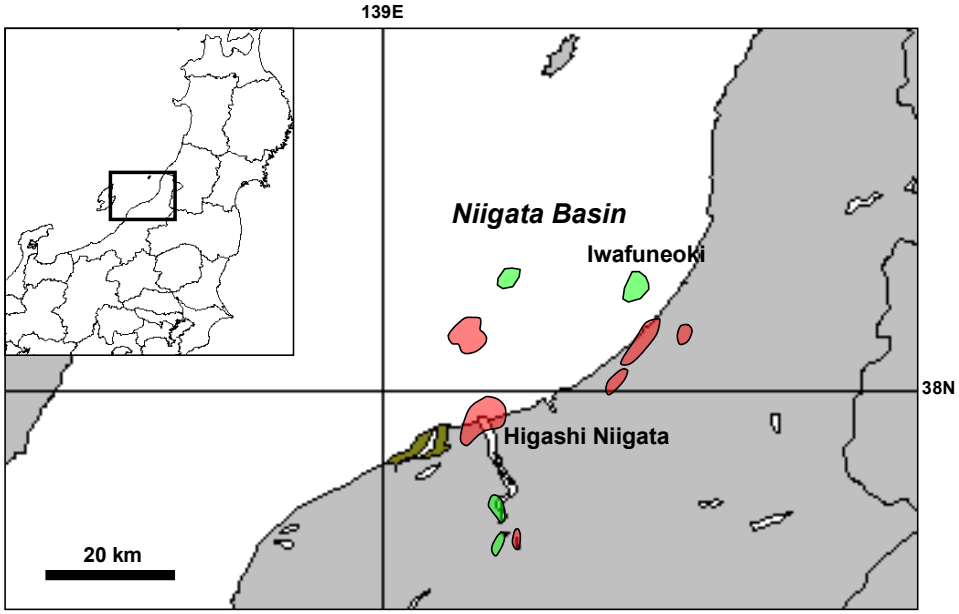

Figure 3.7 Location map of the Niigata Basin, Japan.

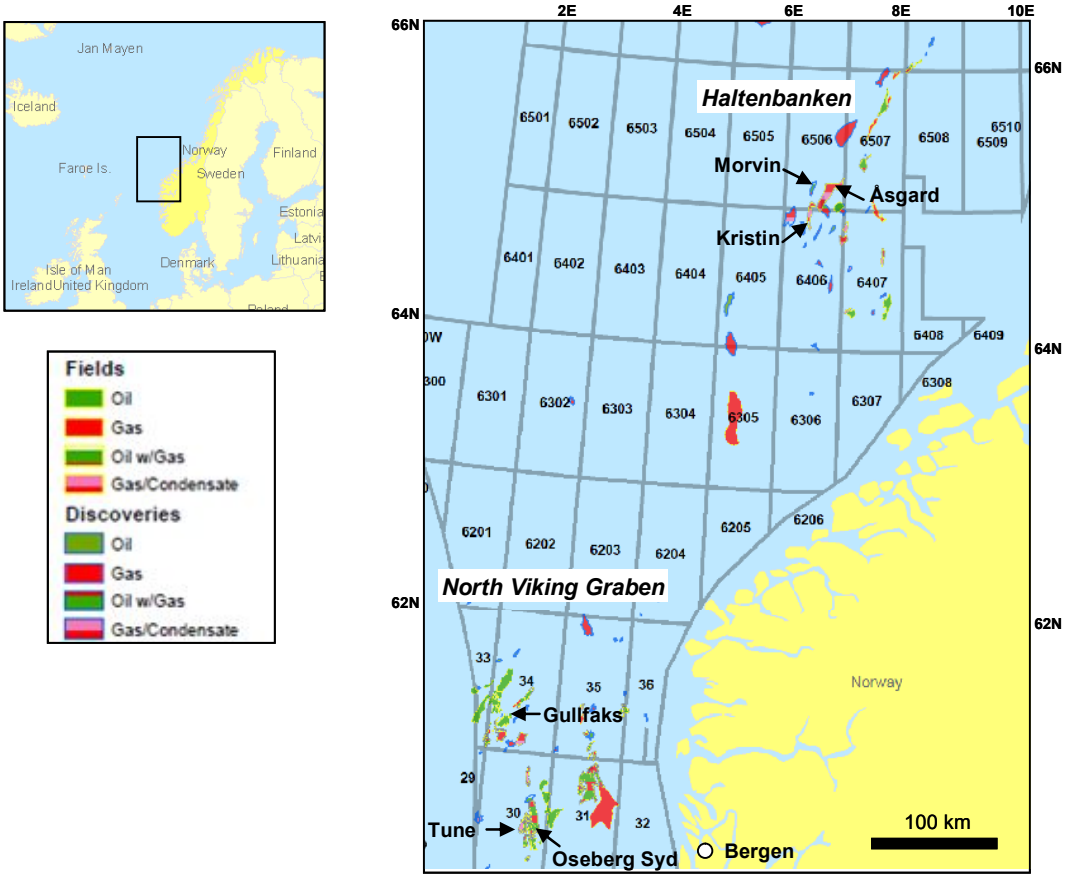

Figure 3.8 Location map of the Haltenbanken and North Viking Graben, offshore Norway. Data from http://www.npd.no.factmap

The excess pressure in the water phase is less than 10 MPa for the Shiiya and younger reservoirs, but it rapidly increases to *ca.* 30 MPa at the Teradomari reservoirs, which is almost equal to the hydrofracturing pressure (Takahata, 2004).

(2) Iwafuneoki field, offshore Niigata, Japan

The Iwafuneoki field, offshore Niigata, Japan, produces oil and gas from several turbidite sand reservoirs of Pliocene age (Miyazaki *et al.* 1987; Moriya *et al.* 2007; **Figure 3.7**). The sands, deposited across the south-plunging Iwafuneoki anticline, form the stratigraphic traps as they shale out to the north, *i.e.* up-dip side of the anticline.

Since it is a stratigraphic trap, it is difficult to identify the exact locations of the effective seals, and thus to determine the column heights and seal parameters. Here column heights are measured from the shallowest reservoir depths encountered by wells to the free water levels, which indicates the minimum possible column heights. As for the seal parameters, data are taken from the mudstone intervals immediately above the reservoirs at shallowest wells. The excess pressure in this field ranges 4 to 15 MPa, showing step-like increases with depth.

Chapter 5 will cover more detailed analysis of the relationship between sealing capacity and abnormal formation pressure in this field.

(3) Haltenbanken, offshore Norway

The Kristin field and Morvin discovery (Norwegian Petroleum Directorate, 2008; **Figure 3.8**) are located in the overpressured compartment immediately west of the Åsgard field (Smørbukk discovery) in the Haltenbanken, offshore Norway. It is exactly where no petroleum accumulations were predicted in Ungerer *et al.* (1990) and Olstad *et al.* (1997) models because they are extremely overpressured. In its report on well 6406/2-3, the first discovery in this overpressured compartment in 1997, Norwegian Petroleum Directorate (2008) says that "*hydrocarbon leakage due to the prognosed high pore pressure in the Kristin structure was regarded the primary risk for the trap, knowing that all high pressured wells drilled in this area had been dry*."

However, the well proved the Jurassic reservoirs to be gas/condensate bearing even though they are highly overpressured almost equal to hydrofracturing pressure (**Figure 3.9 and 3.10**).

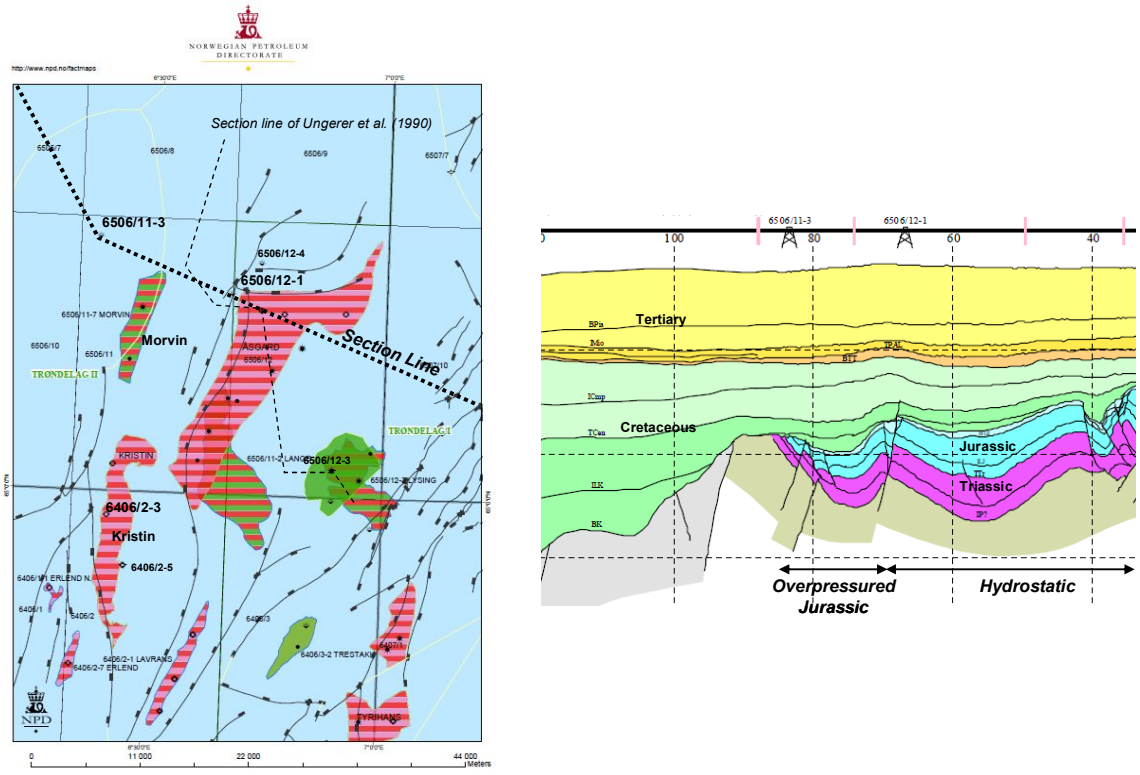

Figure 3.9 Location and schematic cross section of the Haltenbanken, offshore Norway (from Norwegian Petroleum Directorate, 1995; 2008). Leakage from the overpressured compartment was predicted before the discoveries at the Kristin in 1997 and Morvin in 2001 in the overpressured Jurassic.

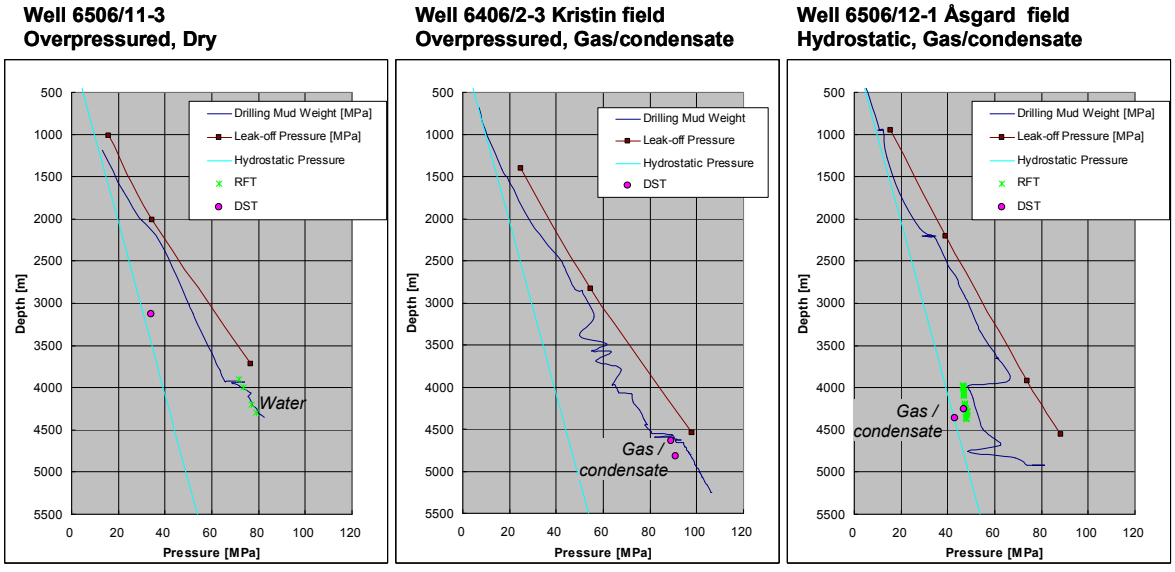

Figure 3.10 Pressure profiles for wells drilled in the overpressured and normally pressured compartments in the Haltenbanken, offshore Norway (data from Olstad et al. 1997 and Norwegian Petroleum Directorate, 2008).
See Figure 3.9 for well locations.

(4) Oseberg Syd and Tune fields, North Viking Graben, Norwegian North Sea

The Oseberg Syd and Tune fields (**Figure 3.8**), located on the eastern flank of the North Viking Graben, Norwegian North Sea, comprises a series of fault blocks of Late Jurassic age (Childs *et al.* 2002a; Childs *et al.* 2002b; Childs *et al.* in press). Oil and gas occur within the sands in the Jurassic Tarbert and Ness Formations and Triassic Statfjord Formation.

Observed petroleum columns in the fields indicate the sealing capacity of the fault rock bounding the traps is required, because the column heights are too large to be explained by the fault juxtaposition seal model (Childs *et al.* in press).

(5) Gullfaks field, North Viking Graben, Norwegian North Sea

The Gullfaks field (**Figure 3.8**), located on the western flank of the North Viking Graben, Norwegian North Sea, produces oil from the Jurassic Tarbert and Ness Formations and Triassic Statfjord Formation (Karlsson, 1986). The field is a highly overpressured fault trap with excess pressure of 12.3 MPa, very close to the hydrofracturing pressure (Heum, 1996). Since it is the shallowest structure of the Tampen Spur, *i.e.* no further lateral migration except for the cap rock leakage, the oil column of *ca.* 200 m is considered to be controlled by sealing capacity of the cap rock (Karlsson, 1986). Heum (1996) suggested that the column is limited by the hydrofratcturing of the cap rock, because the buoyancy caused by the 200 m of oil column roughly corresponds to the difference between the excess pressure of the water phase and the hydrofracturing pressure.

3.2.2 Parameters examined

The relationship between sealing capacity of seal rocks and abnormal pressure in reservoir rocks are examined by a series of cross plots (**Figure 3.11**).

The y-axes of all the plots are the sealing capacity of the seal rocks expressed as the capillary pressure converted from petroleum – water to mercury – air systems (P_{cma}). It is convenient to use P_{cma} rather than P_{cpw} (capillary pressure in petroleum – water system) or buoyancy because it is not dependent on the properties of the trapped fluids, *i.e.* density, interfacial tension and wettability at subsurface conditions. The conversion applied is based on Schowalter (1979), but it should be noted that the petroleum – water interfacial tension at subsurface conditions is often poorly constrained.

The x-axes of **Figure 3.11a** to **c** are the parameters which must be related to the capillary sealing capacity. They are generated to contrast with those in **Figure 3.11d** to **f** which are related to abnormal pressure in the water phase.

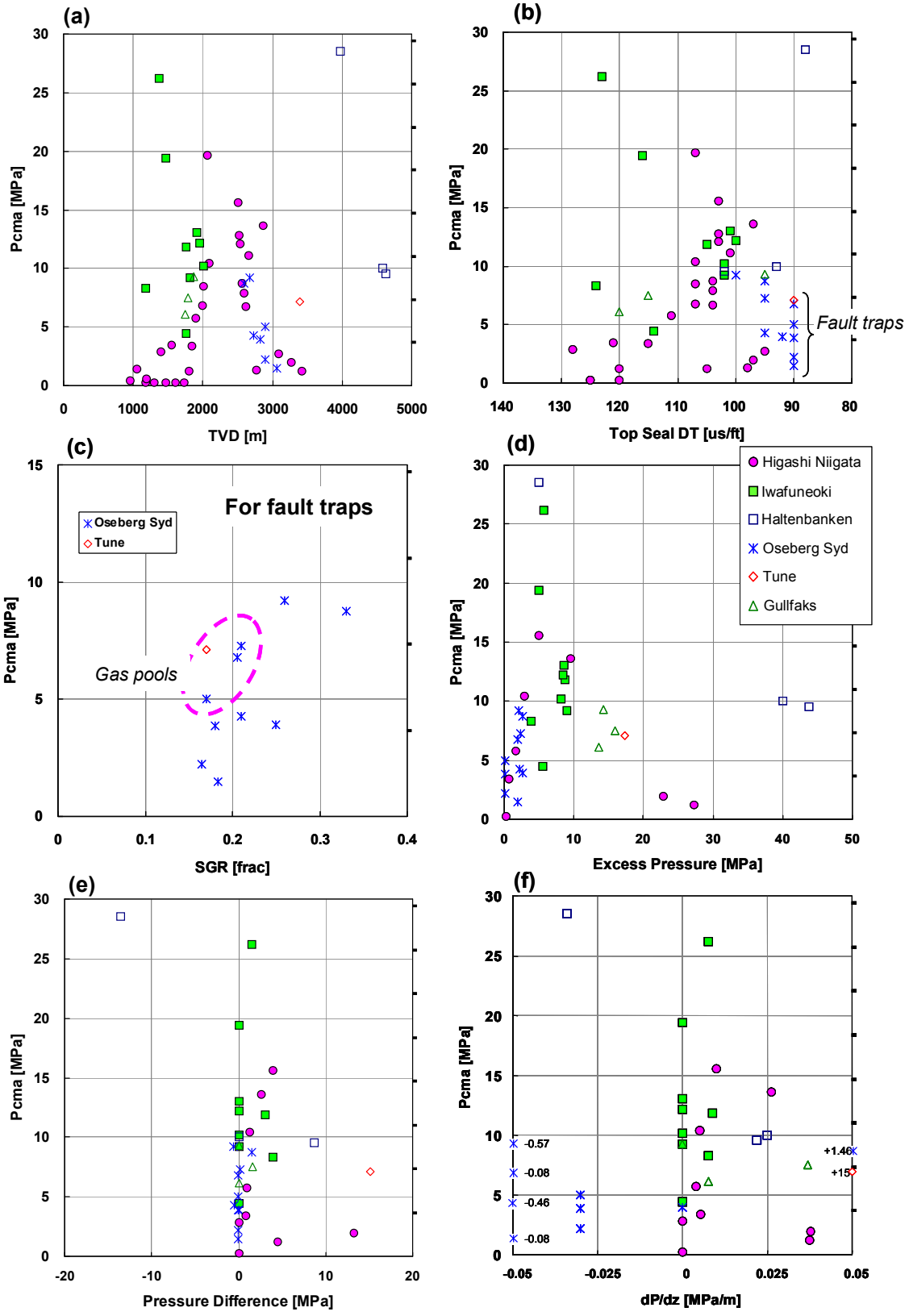

Figure 3.11 Petroleum – water capillary pressure converted to mercury – air system (P_{cma}) plotted against various parameters which may related to seal capacity.

(1) P_{cma} vs. capillary sealing capacity plots (Figure 3.11a to c)

TVD (true vertical depth) is chosen as a parameter indicating compaction trends of seal rocks (**Figure 3.11a**). The capillary sealing capacity is expected to increase with TVD because compaction of the seal rocks progresses with burial. It is only true where the seal rocks do not have significant facies changes and are normally compacted (*i.e.* no abnormal pressure). Despite of this limitation, it is still useful because TVD is the most easily publicly accessible data from all the fields.

Seal rock porosity is a more appropriate parameter for examining the compaction effects than TVD. Average transit time from sonic logs (DT) for the cap rock intervals are taken here as the porosity of the seal rocks, for it is most routinely logged over the sections drilled (**Figure 3.11b**). DT represents the compaction trends even if the sediments are not normally compacted. Therefore the only possible factor to affect the P_{cma} vs. DT relationship is the difference in the cap rock facies, besides the hydrodynamic effects. An exception is for some of the fault traps, where the petroleum leakage is assumed laterally across the faults, not vertically from the cap rocks (Oseberg Syd and Tune fields).

P_{cma} – SGR (shale gouge ratio) cross plot (**Figure 3.11c**) is generated to evaluate the fault rock capillary sealing capacity for the fault traps in the Oseberg Syd and Tune fields where across-fault leakage is assumed (Childs *et al.* 2002a,; 2002b; 2008 in press). SGR is defined as the percentage of mudstone in the slipped interval (Yielding *et al.* 1997), and it is widely accepted as a useful estimator for the capillary sealing capacity of fault rocks, especially in the North Sea (Yielding, 2002; Childs *et al.* 2002c).

(2) P_{cma} vs. abnormal formation pressure plots (Figure 3.11d to f)

Three parameters are used to examine the effects of abnormal pressure in the water phase on the sealing capacity. They are excess pressure P_{ex} (**Figure 3.11d**), the pressure difference ΔP between the reservoir concerned and the adjacent reservoir or aquifer (**Figure 3.11e**), and gradient of the pressure difference $\Delta P/\Delta z$ (**Figure 3.11f**). The definitions for those parameters are schematically shown in **Figure 3.1**.

Those three are the critical parameters to quantify the magnitude of hydrodynamics which might affect the sealing capacity. Many researchers simply take ΔP as the hydrodynamic term in the capillary equilibrium (equation 3.2) for the seal capacity evaluation (Clayton and Hay, 1994; Heum, 1996; Fristad *et al.* 1997). In numerical simulations of migration and entrapment, on the other hand, the hydrodynamic term is expressed as $\Delta P/\Delta z$ and added as a gradient of water potential (equation 2.15).

It should be noted that since the pressure in mudstones can not be measured directly by RFT (wireline pressure measurement) or DST (drill stem test), the parameters are inevitably derived from the pressure in reservoirs, or from drilling mud weight data for the

mudstone interval at best (**Figure 3.10**, but see Chapter 5 for an alternative method for estimating pressure in mudstones). That sometimes leaves ambiguities whether they really represent pressure profiles in seal rocks.

Another difficulty in calculating the parameters is determination of the seal thickness. In fault seal cases, $\Delta P/\Delta z$ is poorly constrained because thickness Δz of fault rocks can not generally be obtained. Here it is assumed to be 1 m, constant for all the fault traps examined.

3.2.3 Hydrodynamic effects from field data

(1) Pcma vs. capillary sealing capacity plots (Figure 3.11a to c)

The best correlation can be seen in **Figure 3.11b** and **c** in which P_{cma} is plotted against porosity of the cap rocks and clay content in fault gouges, respectively. **Figure 3.11a** shows rather vague correlation, but it must be because of the different porosity – depth relationships from different fields.

Cap rock porosity has a very good negative correlation with P_{cma} (P_{cma} increases with decreasing DT) for the anticlinal (Higashi Niigata) and stratigraphic traps (Iwafuneoki), and only some of the points in those fields deflect from the correlation line (**Figure 3.11b**). They are (1) some of the Iwafuneoki pools with extremely high P_{cma} and (2) *ca.* 3,000 m and deeper pools in the Higashi Niigata. The reason for the former will be examined by the variation in mudstone facies (see Chapter 5 for further examination), whereas for the latter can be the hydraulic fracturing caused by the severe overpressure in the deeper reservoirs (Takahata, 2004).

It is noted that even some of the fault traps are plotted on the correlation line in **Figure 3.11b**, *i.e.* the Haltenbanken and Gullfaks. This indicates that the petroleum columns in those fields are controlled by the top seal capacity, rather than the lateral fault seal capacity. On the other hand, the pools in the Oseberg Syd and Tune clearly have smaller P_{cma} for given porosity, indicating lateral leakage from the fault seals. They indeed have a fairly well positive correlation with SGR (**Figure 3.9c**), the index of clay contents in the fault rocks, which indicates the petroleum columns in those fields are controlled by the lateral fault seals. This conclusion is conformable with the migration simulation results by Childs *et al.* (in press). The slight difference in plotted area between oil and gas pools is most probably due to the conversion from petroleum – water to mercury – air system, which is poorly constrained.

(2) Pcma vs. abnormal formation pressure plots (Figure 3.11d to f)

Unlike P_{cma} vs. capillary sealing capacity plots, P_{cma} vs. abnormal formation pressure

plots do not show apparent correlation (**Figure 3.11d** to **f**).

If one assumes that the overpressure in the reservoirs promotes petroleum leakage and the overpressure in the overlying seals retains more petroleum in the reservoirs, all those three plots must have negative correlations, because large numbers in P_{ex} (**Figure 3.11d**) and positive numbers in ΔP and $\Delta P/\Delta z$ (**Figure 3.11e** and **f**) represent overpressure in the reservoirs whereas small numbers in P_{ex} and negative numbers in ΔP and $\Delta P/\Delta z$ represent overpressure in the seals. If, on the contrary, one assumes pressure difference as an indicator of "pressure seals", large numbers (either positive or negative) must be related to high P_{cma}. However, both of the above scenarios do not seem to apply in the example fields shown here.

In summary, **Figure 3.11** illustrates that P_{cma} has good correlation with the indices of capillary sealing capacity (**Figure 3.11a** to **c**) but it does not have apparent correlation with those related to the abnormal pressure in the water phase (**Figure 3.11d** to **f**). This fact clearly indicates that there is no relationship between proven petroleum column height and overpressure in water phase, both positively and negatively.

4 Optimization of permeability - capillary threshold pressure relationship of mudstones

In the previous chapter, it was demonstrated that the abnormal formation pressure itself does not promote nor prevent the trapped petroleum to leak, based on the theoretical consideration of pressure profile in reservoirs and examination of field examples. Abnormal pressure is, however, caused by the retard of water flow in low permeability barriers and meanwhile low permeability k is closely related to high capillary threshold pressure P_{th}. Therefore, abnormal pressure often indicates the existence of effective capillary seals with high P_{th}. Of course, abnormal pressure is not directly related to k but *via* Darcy's law; the amount of water squeezed from the sediments per unit time interval is another important factor for abnormal pressure development. However, if one can quantify the amount of water in the system, then the abnormal pressure data can be used to properly assess or calibrate k and hence P_{th} of mudstones. The most important point in this workflow is the k-P_{th} correlation. This chapter is devoted for establishing appropriate k-P_{th} relationship at reservoir- or basin-scale, to evaluate the capillary sealing capacity by using abnormal pressure data.

The nature of the two key parameters, *i.e.* k and P_{th} of mudstones (not of sandstones), and the relationship between the two will be reviewed first, based on previous researches. The relationship is however, derived from laboratory measurements and theoretical equations, and it might not be applicable to reservoir- or basin-scale models which are important for petroleum migration modelling purpose. A series of numerical experiments (simulations) are carried out to obtain an appropriate up-scaled k-P_{th} relationship to be applied to reservoir- or basin-scale models. Emphasis will be placed on the effects of (1) difference in nature of water flow and petroleum breakthrough, and (2) heterogeneity and anisotropy inherent in geology, on the k-P_{th} relationship at reservoir- or basin-scale. The assessment of k and P_{th} from regional case studies will follow it to illustrate the validity of the up-scaled k-P_{th} relationship established. Finally, a workflow to optimize petroleum migration models by using abnormal formation pressure data will be proposed.

4.1 Previous works on permeability and capillary threshold pressure of mudstone

4.1.1 Permeability of mudstone

Permeability of mudstone is, though the number of the data is still limited compared with those for sandstone (Aplin *et al.* 1999; Aplin and Larter, 2005), significantly lower

than usually assumed and reaches as low as nano-darcy order in both laboratory measurements and regional scale studies (Brace, 1980; Neuzil, 1994).

Generally permeability k of mudstone is given as a function of porosity ϕ based on laboratory measurements and theoretical considerations (Neuzil, 1994; Yang and Aplin, 1998; Tokunaga *et al.* 1998a; Dewhurst *et al.* 1999). **Figure 4.1** compiles ϕ -k relationships reported in literatures. Permeability of mudstone is, however, related not only to porosity but also lithology or pore size distribution (*e.g.* Yang and Aplin, 1998; Aplin and Larter, 2005). Actually, it is reported that absolute permeability may range over three orders of magnitude for a given porosity (Neuzil, 1994). Thus it is important to establish the permeability model as a function of both porosity and lithology.

Discrepancy between core- and regional-scale permeability is reported by many authors (Neuzil, 1994; Dewhurst *et al.* 1999). Dewhurst *et al.* (1999) stated that the apparent scale dependence implies heterogeneous permeability structure usually attributed to fractures, faults or the inter-layering of more permeable, coarser-grained sediments.

4.1.2 Capillary threshold pressure of mudstone

Mercury injection capillary pressure (MICP) measurements are generally employed to estimate capillary threshold pressure P_{th} for plug core or cuttings samples (Purcell, 1949; Schowalter, 1979; Schlomer and Krooss, 1997; Sneider *et al.* 1997; Krushin, 1997). As breakthrough of the non-wetting fluid is not directly observed in MICP measurements, P_{th} is empirically determined as the pressure at non-wetting phase saturation of 7.5 to 10 percent (Schowalter, 1979; Sneider *et al.* 1997), or the pressure at wetting phase saturation of 100% on the capillary pressure curve approximated as a hyperbola (Thomeer, 1960). Direct P_{th} measurement can be made for whole core samples, but the chance of taking whole cores of mudstone is much more limited.

4.1.3 *k*- P_{th} relationship of mudstone

(1) Laboratory experiments

A power-law relationship between permeability k and threshold pressure P_{th} is derived from laboratory experiments by many authors (Thomeer, 1960; Thomas *et al.* 1968; Ingram *et al.* 1997; Hildenbrand *et al.* 2002; Sperrevik *et al.* 2002; Nordgard Bolas *et al.* 2005). Compiling the published data to date reproduces the similar negative correlation as proposed by previous authors (**Figure 4.2**). However, this correlation includes a large amount of uncertainty, and P_{th} values can vary by almost two orders of magnitude at a

given k. This is partly because of the differences in measurement condition and the subjectivity in P_{th} determination as described above, but more importantly, attributed to the variation in facies or pore structure of mudstones.

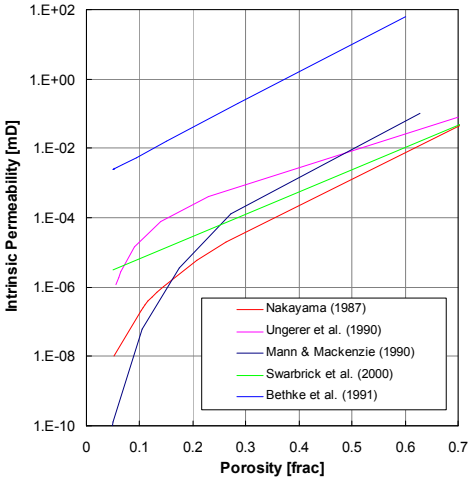

Figure 4.1 Published porosity ϕ and permeability k relationships for mudstone employed in basin-scale numerical models.

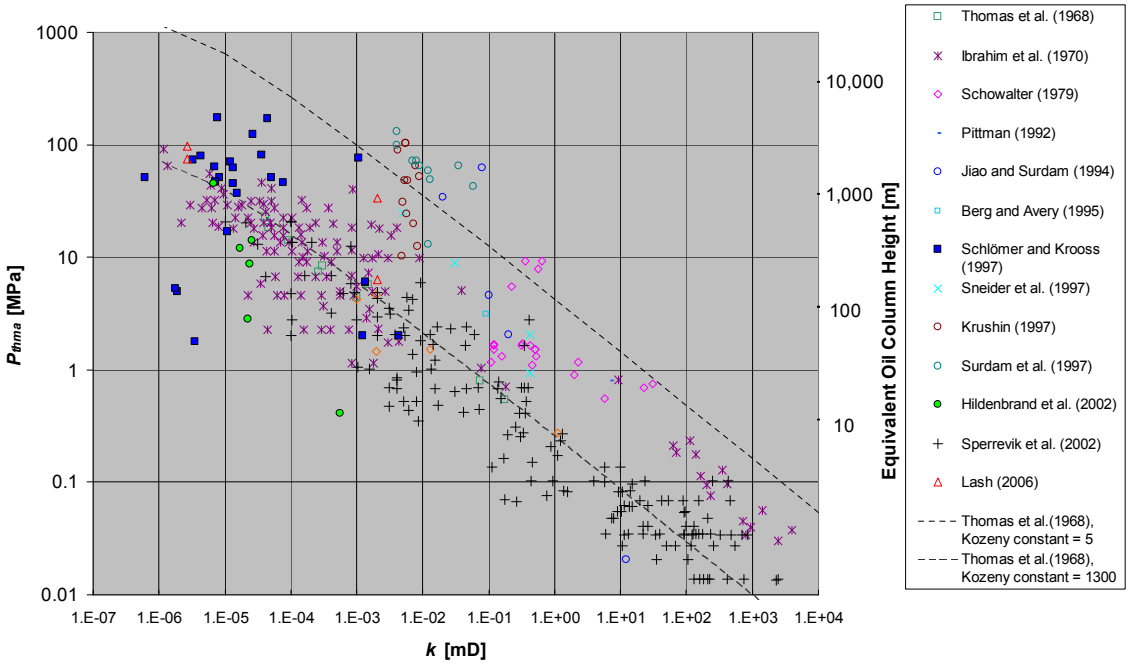

Figure 4.2 Published permeability k and capillary threshold pressure P_{thma} measurements for various rock types. K is to air, except for Schlomer and Krooss (1997) and Lash (2006) in which water permeability is measured. Determination of P_{thma} is according to the individual authors, *i.e.* either the pressure at non-wetting phase saturation (Sa) equals 7.5 to 10%, or the one at which the extrapolated capillary curve intersects Sa=0 line. Krushin (1997), Sneider et al. (1997) and Lash (2006) measured vertical k and P_{th}, but others carried out either horizontal or omni-directional measurements. For conversion of P_{thma} to the equivalent oil column height, density difference of 300 kg/m^3 and interfacial tension of 30 mN/m are assumed.

(2) Semi-theoretical k - P_{th} relationship

Permeability k is closely related to pore-size distribution (Purcell, 1949; Amyx *et al.* 1960; Dewhurst *et al.* 1999), whereas threshold pressure P_{th} is a function of the largest connected pore-throat size. Therefore, they are expected to be closely related to each other (Purcell, 1949; Thomeer, 1960, 1983; Thomas *et al.* 1968).

Thomas *et al.* (1968) related k directly to P_{th} by using the Kozeny-Carman equation (Carman, 1956; Amyx *et al.* 1960). According to this well-known equation, k is a function of porosity ϕ, pore size and pore structure.

$$k = \frac{\phi \cdot \bar{r}_h^{\,2}}{k_o \cdot \tau^2} \tag{4.1}$$

where k_o is a constant (shape factor), τ is tortuosity and $\bar{r}_h$ is mean hydraulic radius. Tortuosity τ is defined here as the ratio of actual flow path L_a to the length across the porous medium L. Mean hydraulic radius $\bar{r}_h$ is the ratio of the pore volume ϕ to the pore surface per unit volume s. $k_o \cdot \tau^2$ is called as Kozeny constant.

$$\tau = \frac{L_a}{L} \tag{4.2}$$

$$\bar{r}_h = \frac{\phi}{s} \tag{4.3}$$

Assuming the pores as circular tubes, $\bar{r}_h$ can be expressed by pore-throat radius r_t

$$\bar{r}_h = \frac{\pi r_t^{\,2}}{2\pi r_t} = \frac{r_t}{2} \tag{4.4}$$

Substituting (4.4) to (4.1) gives

$$k = \frac{\phi \cdot r_t^{\,2}}{4k_o \cdot \tau^2} \tag{4.5}$$

P_{th}, on the other hand, is a function of pore-throat radius r_t, as pore size term in equation (2.24) is safely ignored.

$$P_{th} = 2\gamma \cos\theta \cdot \frac{1}{r_t} \tag{4.6}$$

Combining equations (4.5) and (4.6), Thomas *et al.* (1968) obtained a "theoretical" k-P_{th} relationship.

$$P_{th} = \frac{\gamma \cos\theta}{\sqrt{k_o}\,\tau} \cdot \sqrt{\frac{\phi}{k}} \tag{4.7}$$

If Kozeny constant $k_o \cdot \tau^2$ is assumed to be 5 (Amyx *et al.* 1960) for mudstones, threshold pressure in mercury-air system P_{thma} [Pa] becomes a function of ϕ [frac] and k [m^2]

$$P_{thma} = 0.165 \cdot \sqrt{\frac{\phi}{k}} \tag{4.8}$$

If P_{thma} is in MPa and k is in mD, then,

$$P_{thma} = 5.3 \cdot \sqrt{\frac{\phi}{k}} \qquad (4.8')$$

Although mathematical permeability models based on the Kozeny-Carman equation are extensively used, it is reported that they overestimate permeability of mudstones up to several orders of magnitude larger than measured (Yang and Aplin, 1998; Dewhurst *et al.* 1999). The failure of Kozeny-Carman equation, at least with default constants, for estimating mudstone permeability is because it assumes that (1) pores are circular tubes with identical radii, and (2) permeability is a function of mean pore-throat radius. In reality, however, mudstone has a wide variety of pore size and shape with extremely high tortuosity, and only larger, interconnected pores exclusively control overall permeability of the rocks. Although the efforts to establish more sophisticated mathematical models continue, there is no ideal model to date, to account for the wide variety of mudstone permeability (Dewhurst *et al.* 1999). The failure in predicting mudstone permeability, as might be expected, results in the collapse of the k-P_{th} relationship derived from the "theoretical" models. **Figure 4.2** indicates that the k-P_{th} correlation derived from equation 4.8 does not follow most of the measured data.

In order to obtain an agreement with the laboratory measurements, the Kozeny constant $k_o \cdot \tau^2$ must be increased to *ca.* 1300, which is much higher than the default value.

$$P_{thma} = 0.18 \cdot \sqrt{\frac{\phi}{k}} \qquad (4.9)$$

where P_{thma} is in MPa and k is in mD. In practice, this correlation can be used as a "semi-theoretical" model calibrated by laboratory data, though the Kozeny constant should be determined for individual area or lithology (facies).

4.2 Scale-dependency of k- P_{th} relationship

The effects of heterogeneity and anisotropy in porous media on flow properties can be enormous. Generally porous rocks in sedimentary basins are highly heterogeneous and anisotropic at all scales, from core-, log- to seismic-scales (**Figure 4.3**). However, it is in practice difficult to fully incorporate the heterogeneity and anisotropy in reservoir- or basin-scale models, because (1) there is a limitation for the total number of grid cells to describe the models to save computation time of flow equations, and (2) it is difficult to obtain a perfect description, *e.g.* core-scale details for the entire model volume. Therefore, it is needed to represent the inherently heterogeneous and anisotropic rocks as coarser, *e.g.* seismic-scale, grid cells with up-scaled (or equivalent) properties. Examination of (1) appropriate up-scaling of permeability k and capillary threshold pressure P_{th} and (2) the

relationship between the up-scaled k and P_{th}, which should be used in reservoir or basin modelling, is the subject of this section.

Scaling effect of permeability for sandstones is repeatedly studied and reported in petroleum engineering discipline for more than half a century (*e.g.* Law, 1944; Amyx *et al.* 1960; Warren and Price, 1961; Begg and King, 1985; Yamada, 1995; Sanchez-Vila *et al.* 1996). It should be appreciated that the results of those research works are valid for mudstones. The simplest case is for layer cake (or parallel-bedded) models (**Figure 4.4**). The up-scaled permeability $\bar{k}$ parallel to and normal to the bedding is analytically proven to be the arithmetic, and harmonic means, respectively, of the finer grid k (Amyx *et al.* 1960). In more general cases, it must be somewhere between the harmonic and arithmetic means, depending on the nature and degree of heterogeneity and anisotropy.

On the other hand, very little attention seems to be paid to the scaling effect of capillary threshold pressure (but see Carruthers, 1998). Capillary threshold pressure is determined in principle by a single value of pore-throat radius, *i.e.* the smallest pore-throat in the largest connected pore network through the whole rock volume, as opposed to permeability, which is determined by an average (arithmetic, harmonic or somewhere between the two) of the whole volume. Therefore, the effect of sample heterogeneity can be more robust for threshold pressure than for permeability. As for the layer cake example in **Figure 4.4**, the up-scaled P_{th} equals to the minimum of individual P_{th} values if oil migration is parallel to the bedding, whereas it equals to the maximum P_{th} if the oil migrates perpendicular to the bedding.

The difference in up-scaling nature between k and P_{th} can results in a deviation of k-P_{th} relationship originally derived from core measurements. **Figure 4.5** shows that up-scaled k-P_{th} pairs are plotted off the original k-P_{th} correlation line. Given constant k and P_{th} for individual layers, the up-scaled k-P_{th} pairs can be plotted inside the blue square in this figure, depending on the relative thickness of those layers.

One of the most widely-used methods to find out the scaling effects for geologically complex models is running numerical flow simulations for fine-scale models to obtain the up-scaled property values. The same approach is employed in this research to examine the scaling effects of k-P_{th} for heterogeneous and/or anisotropic mudstone or mudstone-dominated sequences. The questions to be answered are what the geologically realistic up-scaled k-P_{th} correlation line would be, and how large the range or uncertainty of the correlation would be.

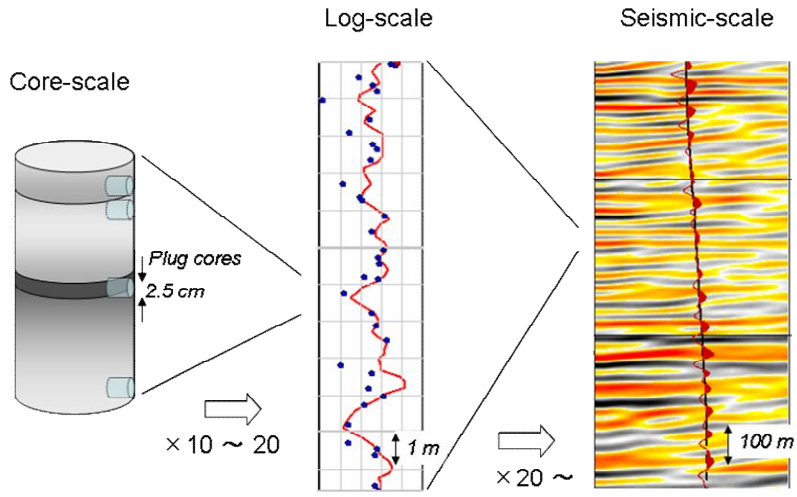

Figure 4.3 Different scales in geological models. Core measurements are normally performed for small plugs with 1 inch diameter. Vertical resolution of conventional wireline logs ranges from 1 to 2 feet, whereas that of seismic profiles is more than 10 m.

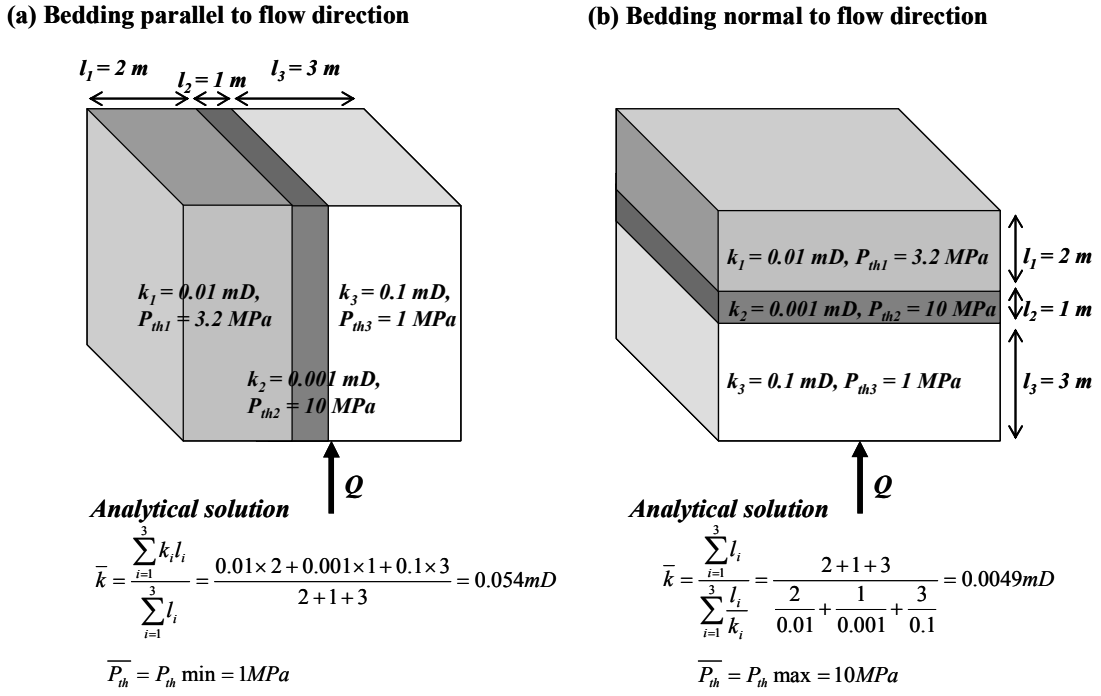

Figure 4.4 Up-scaled (equivalent) permeability and capillary threshold pressure for parallel-bedded mudstone models. Water or petroleum flux Q is assumed from the bottom of the cubes.

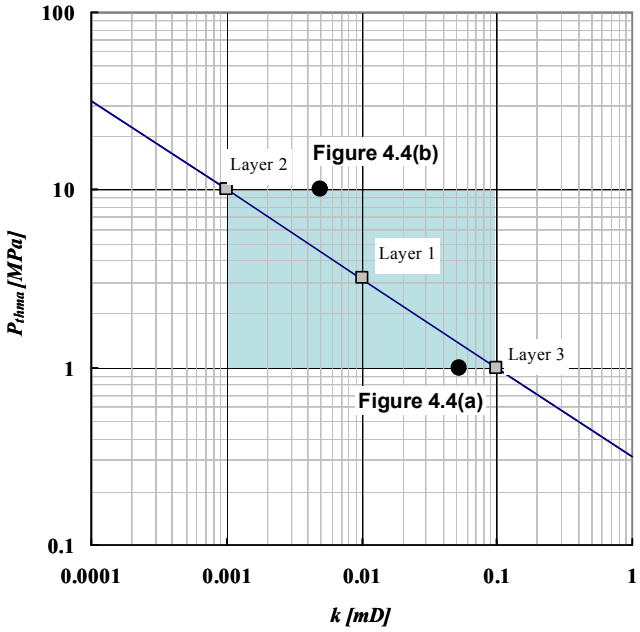

Figure 4.5 **Cross plot of up-scaled permeability k and capillary threshold pressure P_{thma} for parallel-bedded mudstone models (Figure 4.4). Shaded area indicates possible range of up-scaled k and P_{thma} for different proportions of the layer thickness. Note that up-scaled $k-P_{thma}$ pairs do not necessarily follow the $k-P_{thma}$ correlation line derived from those of individual layers.**

4.2.1 Creating numerical models

Two kinds of 3D synthetic models were used for the numerical simulations: random distribution models and geostatistical models. Both of the models are made up of three layers, the thick middle layer representing mudstone or sand-mud mixture in question, sandwiched by two thin sandstone layers on the top and bottom. The top and bottom sand layers are set to be highly permeable compared with the mudstone in the middle, and act as the tabular injector and producer of water and oil.

The list of generated models is shown in **Tables 4.1** and **4.2**. It should be noted that the k and P_{th} are correlated by equation 4.10, which is in close agreement with the core-derived k-P_{th} relationship (**Figure 4.2**).

$$\log P_{thma} = -0.5 \cdot \log k - 0.5 \qquad (4.10)$$

where P_{thma} is in mercury-air system in MPa and k in mD.

The models are static in nature, *i.e.* geometry and properties do not change with time. This is because the purpose of the simulations here is simply to examine the up-scaled k-P_{th} relationship.

(1) Random k-P_{th} distribution models

The models are composed of equal sized cubic cells of 20 by 20 by 22 (20 cells representing mudstone plus top and bottom sand layers) in x, y and z directions, respectively (**Figure 4.6**). Size of the each cell is 0.025 m (equal to core dimension), and that of the total volume is 0.5 m (equal to wireline log dimension).

Permeability and capillary threshold pressure are assigned for each cell by Monte-Carlo simulations. Random k-P_{th} fields were generated for heterogeneous isotropic models, by using normal and log-normal distributions with various standard deviations (**Figure 4.7** and **Tables 4.1**), while the same k-P_{th} fields were used for heterogeneous anisotropic models but conditioned by sedimentary structures (parallel-bedding; **Figure 4.8** and **Tables 4.1**). Adopting normal distribution for k and P_{th} is simply because mathematical treatment is straightforward. Log-normal distribution would be more appropriate to represent realistic k and P_{th} fields because pore size (or grain size) distribution in reality is often approximated with log normal distribution (*e.g.* Law, 1944), though there are criticisms for doing so (*e.g.* Sanchez-Vila *et al.* 1996). Generated k distributions for each model cover a couple of orders of magnitude, which is consistent with those for natural mudstones (*e.g.* Dewhurst *et al.* 1999).

Table 4.1 Input parameters and results of water flow and oil migration simulations for random k-P_{th} distribution models

Model	Homogeneous isotropic	Heterogeneous isotropic					Heterogeneous isotropic					Heterogeneous anisotropic				
	mud0	mud1-01	mud1-02	mud1-03	mud1-04	mud1-05	mud2-01	mud2-02	mud2-03	mud2-04	mud2-05	mud3-01	mud3-02	mud3-03	mud3-04	mud3-05
Rock properties																
Distribution	Uniform			Normal					Log normal					Log normal		
Coefficient of variance	0.0	0.1	0.2	0.3	0.4	0.5	0.1	0.2	0.3	0.4	0.5	0.1	0.2	0.3	0.4	0.5
Permeability k																
Arithmetic mean [mD]	0.010	0.010	0.010	0.010	0.010	0.010	0.010	0.011	0.013	0.015	0.019	0.011	0.011	0.013	0.015	0.019
Geometric mean [mD]	0.010	0.010	0.010	0.010	0.010	0.010	0.010	0.010	0.010	0.010	0.010	0.010	0.010	0.010	0.010	0.009
Harmonic mean [mD]	0.010	0.010	0.010	0.010	0.010	0.010	0.010	0.009	0.008	0.006	0.005	0.009	0.009	0.007	0.006	0.002
Threshold pressure P_{thma}																
Arithmetic mean [MPa]	3.162	3.162	3.162	3.162	3.162	3.162	3.183	3.237	3.340	3.491	3.697	3.271	3.541	4.026	4.796	5.964
Geometric mean [MPa]	3.162	3.162	3.162	3.162	3.162	3.162	3.162	3.162	3.162	3.162	3.162	3.165	3.164	3.142	3.050	2.668
Harmonic mean [MPa]	3.162	3.162	3.162	3.162	3.162	3.162	3.140	3.065	2.957	2.813	2.636	3.063	2.827	2.443	1.840	0.703
Sedimentary structure	none			None					None					Parallel-bedded		
Water flow simulation results																
q_w [m/yr]	0.622	0.606	0.603	0.599	0.598	0.605	0.619	0.665	0.743	0.869	1.066	0.621	0.659	0.732	0.850	1.033
Upscaled k																
k [mD]	0.010	0.010	0.010	0.010	0.010	0.010	0.010	0.011	0.012	0.014	0.017	0.010	0.011	0.012	0.014	0.017
k [m^2]	9.86E-18	9.59E-18	9.55E-18	9.49E-18	9.46E-18	9.58E-18	9.81E-18	1.05E-17	1.18E-17	1.38E-17	1.69E-17	9.84E-18	1.04E-17	1.16E-17	1.35E-17	1.64E-17
Upscaled/Original [%]	100.0	99.0	98.6	97.9	97.7	98.8	101.2	108.7	121.4	142.0	174.2	101.5	108.5	121.6	145.5	197.9
Oil migration simulation results																
Up-scaled P_{th}																
P_{thma} [MPa]	3.162	3.053	2.852	2.705	2.565	2.517	2.993	2.864	2.722	2.587	2.459	2.784	2.539	2.275	2.038	1.826
Upscaled/original [%]	100.0	96.5	90.2	85.6	81.1	79.6	94.7	90.6	86.1	81.8	77.8	74.8	68.2	61.1	54.8	49.1
Invaded cells																
No. of invaded cells	20	1148	773	860	748	1047	433	755	757	757	758	1379	819	810	807	746
S_o [%]	0.3	14.4	9.7	10.8	9.4	13.1	5.4	9.4	9.5	9.5	9.5	17.2	10.2	10.1	10.1	9.3

Table 4.2 Input parameters and results of water flow and oil migration simulations for geostatistical k-P_{th} distribution models

Model	Tarbert_all	Tarbert_01	Tarbert_02	Tarbert_03	Tarbert_04	Tarbert_05	Tarbert_06	Tarbert_07	Tarbert_08	Tarbert_09	Tarbert_10	Tarbert_11	Tarbert_12
Rock properties													
Distribution							Normal						
Permeability k													
k_v_mean [mD]	0.774	0.717	0.780	0.754	0.694	0.845	0.920	0.710	0.840	0.863	0.675	0.746	0.743
k_v_sigma [mD]	0.334	0.328	0.335	0.316	0.324	0.328	0.339	0.317	0.318	0.323	0.326	0.326	0.332
k_v/k_h	0.01	0.01	0.01	0.01	0.01	0.01	0.01	0.01	0.01	0.01	0.01	0.01	0.01
Threshold pressure P_{thma}													
P_{thma} mean [MPa]	0.414	0.435	0.404	0.414	0.460	0.389	0.363	0.438	0.383	0.369	0.462	0.427	0.429
P_{thma} sigma [MPa]	0.284	0.275	0.200	0.264	0.400	0.262	0.186	0.322	0.213	0.147	0.380	0.300	0.316
Sedimentary structure							Shallow marine						
Water flow simulation results													
q_w [m/yr]	0.976	0.912	0.967	0.957	0.866	1.057	1.149	0.884	1.077	1.126	0.830	0.922	0.923
Upscaled k													
k [mD]	0.681	0.636	0.674	0.667	0.604	0.737	0.801	0.617	0.751	0.785	0.579	0.643	0.644
k [m^2]	6.60E-16	6.16E-16	6.53E-16	6.47E-16	5.85E-16	7.14E-16	7.76E-16	5.97E-16	7.28E-16	7.61E-16	5.61E-16	6.23E-16	6.24E-16
Upscaled/Original [%]	88.0	88.7	86.4	88.5	87.0	87.2	87.1	86.8	89.4	91.0	85.8	86.2	86.7
Oil migration simulation results													
Up-scaled P_{th}													
P_{thma} [MPa]	0.355	0.370	0.412	0.427	0.427	0.358	0.356	0.411	0.340	0.339	0.399	0.442	0.450
Upscaled/original [%]	85.8	85.1	101.9	103.1	92.7	92.2	98.0	93.8	88.8	91.9	86.3	103.5	104.9
Invaded cells													
No. of invaded cells	2402	2963	1456	1756	2608	1828	2215	1830	1676	1626	1886	3602	3166
S_o [%]	0.5	7.7	3.8	4.6	6.8	4.7	5.8	4.8	4.4	4.2	4.9	9.4	8.2

Model	Ness_all	Ness_01	Ness_02	Ness_03	Ness_04	Ness_05	Ness_06	Ness_07	Ness_08	Ness_09	Ness_10	Ness_11	Ness_12
Rock properties													
Distribution							Bimodal						
Permeability k													
k_v_mean [mD]	0.639	0.607	0.781	0.587	0.603	0.743	0.599	0.566	0.688	0.641	0.548	0.624	0.676
k_v_sigma [mD]	0.397	0.395	0.396	0.386	0.396	0.395	0.388	0.392	0.396	0.386	0.381	0.395	0.388
k_v/k_h	0.01	0.01	0.01	0.01	0.01	0.01	0.01	0.01	0.01	0.01	0.01	0.01	0.01
Threshold pressure P_{thma}													
P_{thma} mean [MPa]	0.545	0.562	0.459	0.567	0.570	0.483	0.562	0.604	0.513	0.538	0.612	0.555	0.514
P_{thma} sigma [MPa]	0.526	0.532	0.426	0.523	0.546	0.465	0.527	0.600	0.500	0.507	0.609	0.535	0.495
Sedimentary structure							Fluvial						
Water flow simulation results													
q_w [m/yr]	0.593	0.561	0.752	0.530	0.557	0.699	0.548	0.435	0.628	0.595	0.481	0.559	0.636
Upscaled k													
k [mD]	0.543	0.514	0.689	0.486	0.510	0.640	0.502	0.399	0.575	0.546	0.441	0.512	0.583
k [m^2]	5.27E-16	4.98E-16	6.68E-16	4.71E-16	4.94E-16	6.20E-16	4.86E-16	3.86E-16	5.57E-16	5.29E-16	4.27E-16	4.96E-16	5.65E-16
Upscaled/Original [%]	85.1	84.7	88.2	82.8	84.6	86.2	83.8	70.4	83.6	85.1	80.4	82.1	86.3
Oil migration simulation results													
Up-scaled P_{th}													
P_{thma} [MPa]	0.323	0.359	0.323	0.446	0.435	0.354	0.400	0.447	0.415	0.422	0.405	0.401	0.356
Upscaled/original [%]	59.3	63.9	70.5	78.6	76.2	73.3	71.1	74.0	80.9	78.4	66.2	72.2	69.2
Invaded cells													
No. of invaded cells	493	1352	476	2452	951	664	2254	2670	1804	1808	2485	1935	1017
S_o [%]	0.1	3.5	1.2	6.4	2.5	1.7	5.9	6.9	4.7	4.7	6.5	5.0	2.6

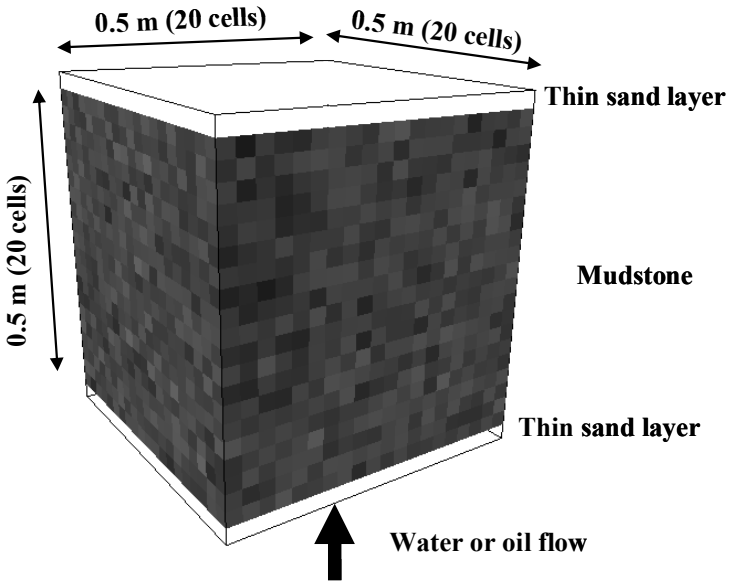

Figure 4.6 Configuration of log-scale and seismic-scale random-distribution mudstone models. Mudstone of 0.125 m3, which corresponds to wireline log-scale, is represented by 8,000 core-size cells.

(a) Log3D_mud0

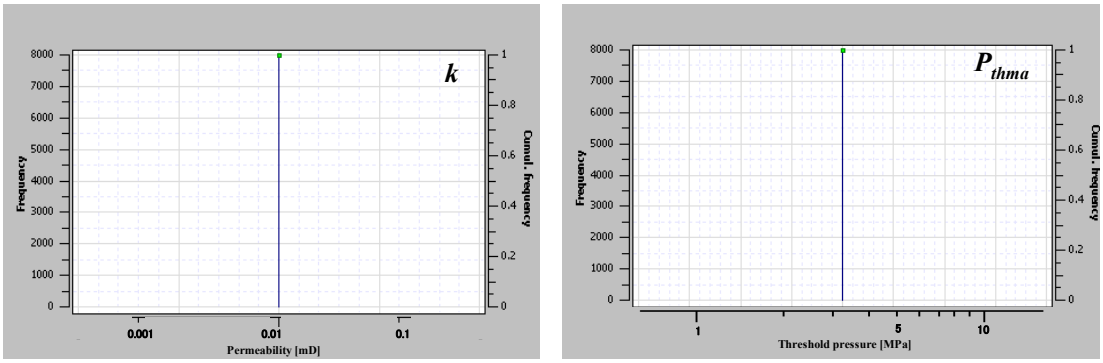

(b) Log3D_mud2-03

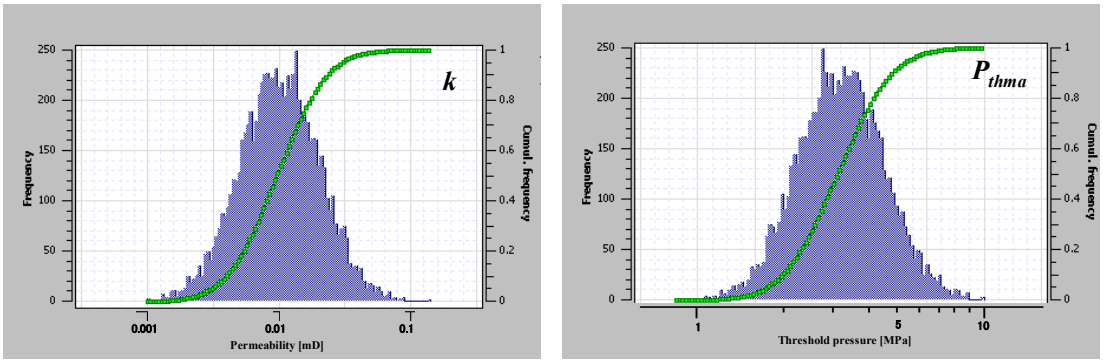

Figure 4.7 Permeability and threshold pressure distributions for (a) homogeneous mudstone model (Log3D_mud0) and (b) heterogeneous isotropic mudstone model (Log3D_mud2-03).

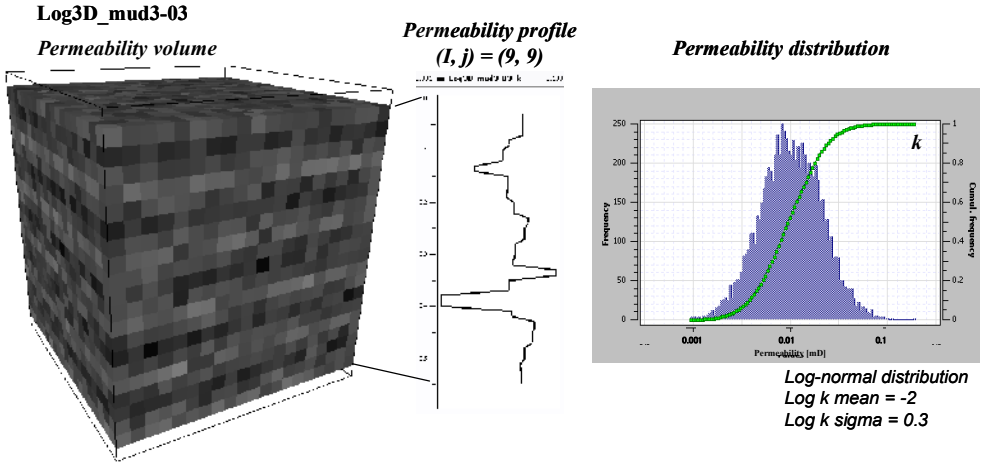

Figure 4.8 Permeability distribution for heterogeneous anisotropic mudstone model (Log3D_mud3-03). Note that k distribution curve is almost identical to that for isotropic model Log3D_mud2-03 (Figure 4.7).

(2) Geostatistical models

Although random distribution models described above cover realistic ranges of k-P_{th}, it is not clear if anisotropy of the models is sufficiently large to represent that of natural mudstones or mudstone-dominated sequences. The best way to examine it is no doubt to use a wide variety of real samples at log- or seismic-scales, but it is practically difficult because there are very little quantitative 3D data available (Jackson *et al.* 2005). Here, publicly available geostatistical models were used to examine the effect of anisotropy on k-P_{th} relationship, as an alternative method. Geostatistical models are more geologically realistic than random distribution models, because they incorporate anisotropy by means of variograms derived from logs or seismic data.

The models were taken from Model 2 of the 10th SPE Comparative Solution Project on up-scaling (**Figure 4.9**; see Christie and Blunt (2001) for full description of the model). The model dimension is 365.76 by 670.56 by 51.816 m, composed of 60 by 220 by 55 grid cells (cell size is 20 by 10 by 2 ft). The model consists of part of the Brent Group, North Sea, and the upper half of the original model represents the Tarbert Formation deposited in shallow marine environment, and the lower half represents the Upper Ness Formation deposited in fluvial environment.

The original model was vertically split into two models, *i.e.* Tarbert and Ness models and the permeable injector and producer layers are added on the top and bottom, just like the random distribution models described above. Those two regional models correspond to grid cell sizes of conventional basin-scale simulations. In addition, each of those was horizontally divided into 12 sub-volumes, for individual models to represent seismic-scale

grid cells used in reservoir-scale simulations (**Figure 4.9** and **Tables 4.2**).

Permeability was derived from the original SPE model, ranging *ca.* 0.1 to 200 mD for horizontal permeability k_h, and 0.001 to 2 mD for vertical permeability k_v, (k_v/k_h = 0.01). The permeability field for the Tarbert model shows a normal distribution, while that for the Ness model indicates a bimodal distribution, reflecting the difference in depositional environments of those formations (**Figure 4.10**). Since there is no P_{th} assigned in the original model, it was calculated by equation 4.10.

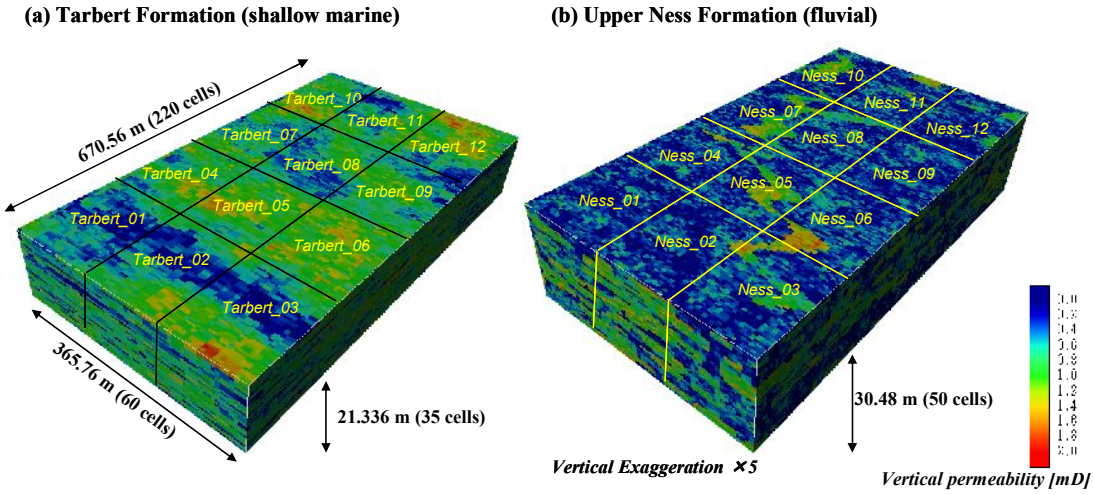

Figure 4.9 3D view of 10th SPE comparative solutions dataset No.2 (Christie and Blunt, 2001). The original model is divided into 24 sub-volumes (Tarbert_01 to 12 and Ness_01 to 12) to represent seismic-scale grid cells.

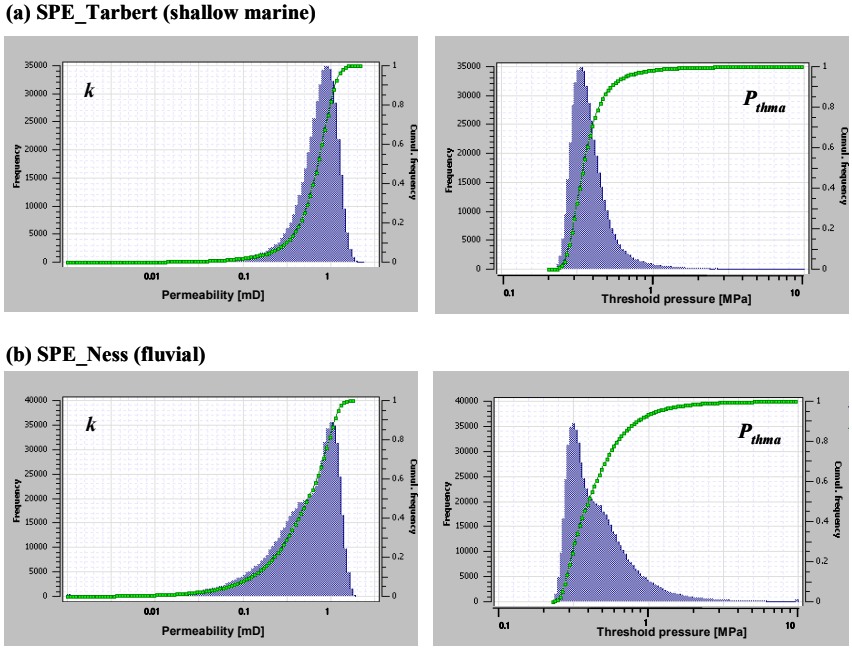

Figure 4.10 Permeability and threshold pressure distributions for geostatistical models (Figure 4.9). Threshold pressure was calculated from permeability.

4.2.2 Numerical simulation methods

Two kinds of numerical flow simulations are carried out for the created models, *i.e.* water flow and oil migration simulations. Commercial software MPath (Carruthers, 1998) was used for both of the simulations.

(1) Water flow simulations

For water flow simulation, an excess pressure ΔP of 1 MPa was applied to the bottom sand layer whereas the pressure at the top sand layer was kept hydrostatic. No-flow boundary conditions are set to the sides of the models. That is, the boundary conditions are the same as those for laboratory permeability measurements. By running steady-state flow simulation which solve the Laplace's equation (See equation 2.14 in Section 2.3.3), the Darcy velocity q_w was calculated for each cell in the model volume. The up-scaled permeability $\bar{k}$ was calculated by applying Darcy's law across the whole volume.

$$\bar{k} = -\mu_w \frac{\Delta L}{\Delta P} \sum q_w \cdot s \qquad (4.11)$$

where, ΔL: length of the model parallel to the flow direction (z-direction)

μ_w : water viscosity

s: area of individual grid cells.

(2) Oil migration simulations

For oil migration simulations, oil was injected into the water saturated volume from the middle of the bottom sand layer, and allowed to invade upward by its buoyancy until it percolates to the top sand layer. No-flow boundary conditions are used in the simulations. The unidirectional oil injection in the simulations is the main difference from MICP measurements in laboratories, in which omni-directional mercury intrusion is applied. Since natural oil migration occurs more or less unidirectional, the numerical simulation shown here must be more appropriate to mimic oil migration process (Carruthers, 1998).

Invasion percolation algorithm was employed and the least resistive migration path was traced. Then the capillary pressure value and the number of invaded cells when the percolation occurred were reported as the up-scaled P_{th} and the critical oil saturation S_{oc}, respectively.

4.2.3 Results of numerical simulations

(1) Homogeneous isotropic model

The homogeneous isotropic model "Log3D_mud0" with constant k (=0.01 mD) and

P_{thma} (=3.16 MPa) was first tested as the reference model (**Figure 4.7a**). The results of water flow and oil migration simulations are shown in **Figure 4.11**. As expected, constant water flow rate throughout the model volume (**Figure 4.11a**) and vertical oil migration pathway (**Figure 4.11b**) were reproduced and the up-scaled k (=0.01 mD) and P_{th} (=3.16 MPa) equal to those for individual cells were obtained (**Table 4.1**).

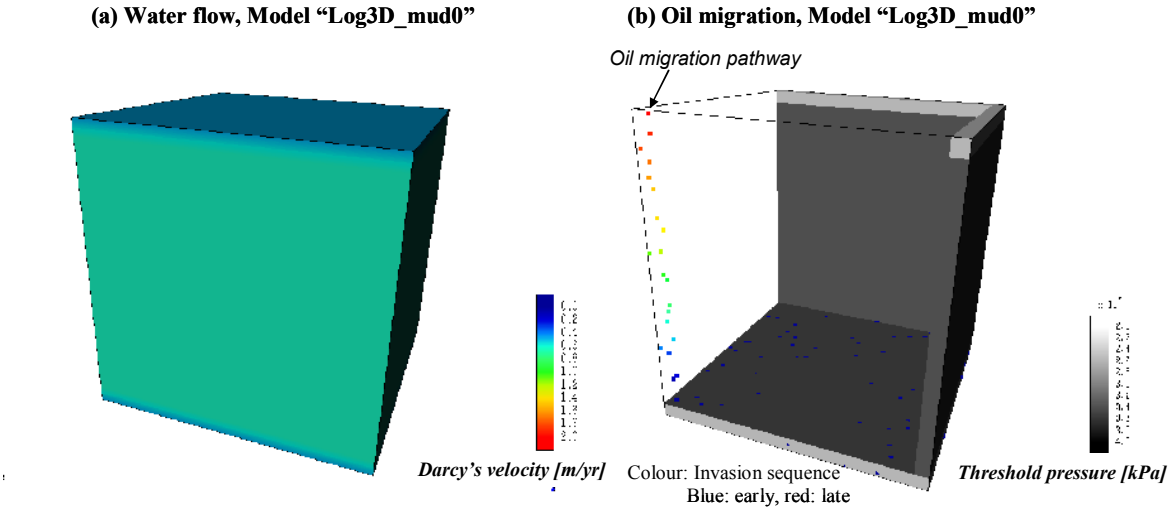

Figure 4.11 Water and oil flow simulation results for log-scale mudstone model "Log3D_mud0", in which constant k (=0.01 mD) and P_{th} (= 3.16 MPa) are used. (a) Darcy's velocity of steady state water flow. Water is injected from the bottom at a constant pressure of 1 MPa. (b) Oil migration pathway color-coded by invasion sequence (from blue to red). Sufficient volume of oil to percolate the model is injected from the bottom.

(2) Heterogeneous isotropic models

Total 10 heterogeneous isotropic mudstone models were generated by randomly assigning k and P_{th} with normal and log-normal distributions (**Table 4.1**). As shown in **Figure 4.12**, both the water flow rate and oil migration pathway become rather complex because of the heterogeneity in k and P_{th}.

The results of water flow simulations indicate that the up-scaled k is equal to the mean of individual k for normal distribution models (*i.e.* k = 0.01 mD regardless of standard deviation σ), while it takes a value between the arithmetic and geometric means for log-normal distribution models (*i.e.* k becomes larger with σ). The reason for the latter is currently not clear. The result looks inconsistent with previous works (Warren and Price, 1961), and can be accidental.

On the other hand, the results of oil migration simulations indicate that up-scaled P_{th} is always smaller than the harmonic mean and become smaller with σ, for both normal and log-normal distribution models. It is interpreted that as σ increases the possibility

increases for a path with smaller P_{th} through the model volume to be formed.

According to the simulations, up-scaled P_{th} becomes small with increasing heterogeneity, whereas up-scaled k is same as the geometric mean or less than the arithmetic mean at largest. Thus it can deflect the k-P_{th} relationship established by core measurements (**Figure 4.13**). However, the amount of deviation is rather small and less than one order of magnitude. The models tested here will cover the sufficient range of heterogeneity for natural mudstones (*e.g.* see **Figure 4.2**), and still the resultant up-scaled P_{th} is *ca.* 80% of the geometric means at minimum and the up-scaled k is *ca.* 170% of the geometric means at maximum. It is therefore concluded that the k-P_{th} relationship derived from core measurements is valid for up-scaled models, as long as the mudstone is isotropic.

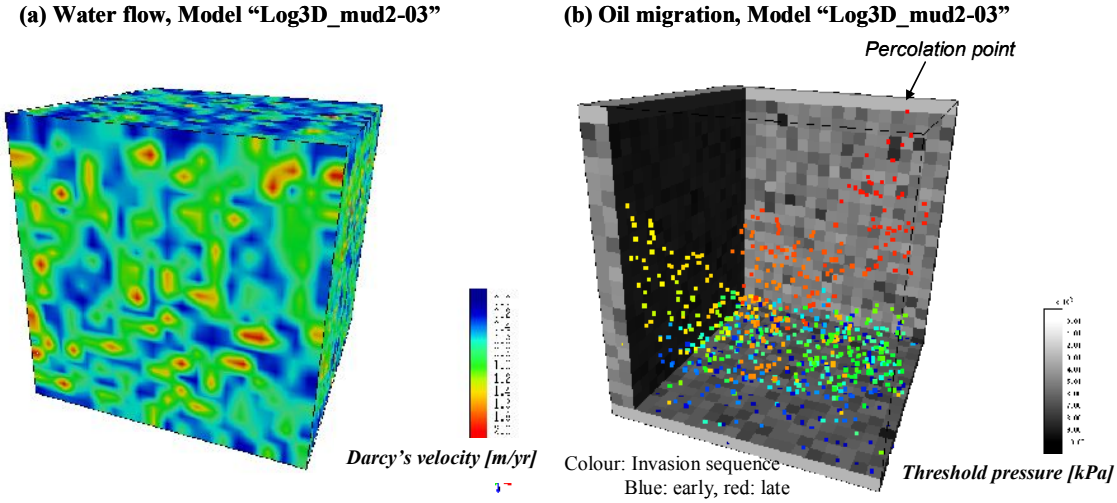

Figure 4.12 Water and oil flow simulation results for log-scale mudstone model "Log3D_mud2-03", with log-normal k and P_{th} distribution. (a) Darcy's velocity of steady state water flow. (b) Oil migration pathway color-coded by invasion sequence.

(3) Heterogeneous anisotropic models

The heterogeneous anisotropic models tested here (Log3D_mud03; **Figure 4.8**) consist of alternating beds of more permeable and less permeable layers with k of log-normal distributions same as those for heterogeneous isotropic models described above (Log3D_mud02).

The results of water flow simulations are very similar to those for isotropic models (**Figure 4.14**), *i.e.* the effect of stratification is rather small, at least for these particular models.

The results of oil migration simulations indicate that the up-scaled P_{th} becomes smaller than the geometric means with increasing σ, implying that less resistive pathways crossing the highest P_{th} layers are formed.

Since the decrease of up-scaled P_{th} is more pronounced than the increase of the up-scaled k, it results in the deviation in the k-P_{th} correlation (**Figure 4.13**). However, the amount of deviation is very small and it would cause an error in estimation of P_{th} from k by a factor of two at maximum.

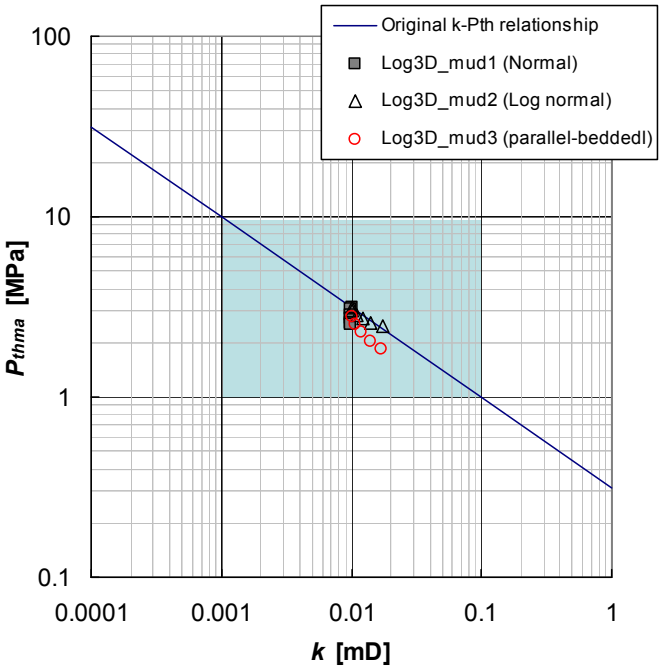

Figure 4.13 Cross plot of equivalent (up-scaled) permeability k and capillary threshold pressure P_{thma} for heterogeneous isotropic mudstone models. Shaded area indicates possible range of equivalent k and P_{thma}.

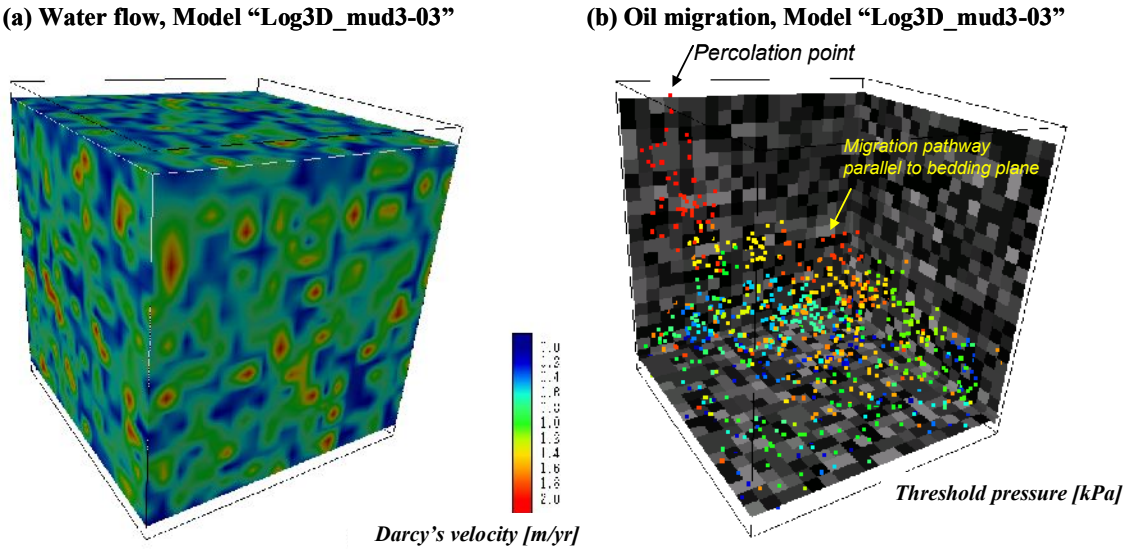

Figure 4.14 Water and oil flow simulation results for heterogeneous anisotropic model "Log3D_mud3-03" (Figure 4.8). (a) Darcy's velocity of steady state water flow. (b) Oil migration pathway color-coded by invasion sequence.

(4) Geostatistical models

Total 26 geostatistical models (2 regional-scale models using the whole volumes and 24 seismic-scale sub-volume models) were tested as geologically more realistic models than the ones generated by Monte-Carlo simulations (**Figure 4.15** to **17** and **Tables 4.2**).

Those figures show very complex flow patterns both for water and petroleum, reflecting geological complexity of the models. Furthermore, they are very different between the Tarbert and Ness models. That is, lateral flow patterns are predominant in the Tarbert models while more vertical paths are predominant in the Ness. It is attributed to the difference in depositional facies between the two. The Tarbert models consist of rather large laterally-continuous sandstone bodies and both water and oil tend to flow laterally through those. On the other hand, in the Ness models, because individual sandstone bodies are small and laterally less connected, water and oil have to flow vertically up through mudstones to reach other sandstones. It illustrates significant influence of facies on both water and petroleum flow.

In spite of their complex flow patterns, the k-P_{th} correlation does not show large deviation from the original one after all (**Figure 4.18**). This might be unexpected results. Actually the upscaled k and P_{th} of its own deflect from the original mean values. However, since k moves right-hand side and P_{th} moves downward, they cancel out the scaling effects and the k-P_{th} correlation does not change much.

4.2.4 Scale independency of k- P_{th} relationship

In this section, scale dependency of k- P_{th} relationship were examined by a series of numerical simulations. The geological models used are all synthetic, but represent log- to seismic-scale rock volumes, and cover a sufficient range of heterogeneity and anisotropy in natural rock volumes.

Simulation results indicate the followings;

(1) up-scaled k is larger than the average of original k, by a factor of two or less
(2) up-scaled P_{th} is smaller than the average of original P_{th} by a factor of two or less
(3) But it does not change the k- P_{th} correlation, *i.e.* the correlation is scale-independent.

Therefore, if one can correctly estimate up-scaled k, one can also correctly estimate P_{th} of the same representative rock volume, by using the common k- P_{th} relationship. The validity of the scale independency of k- P_{th} relationship is further examined in the next section.

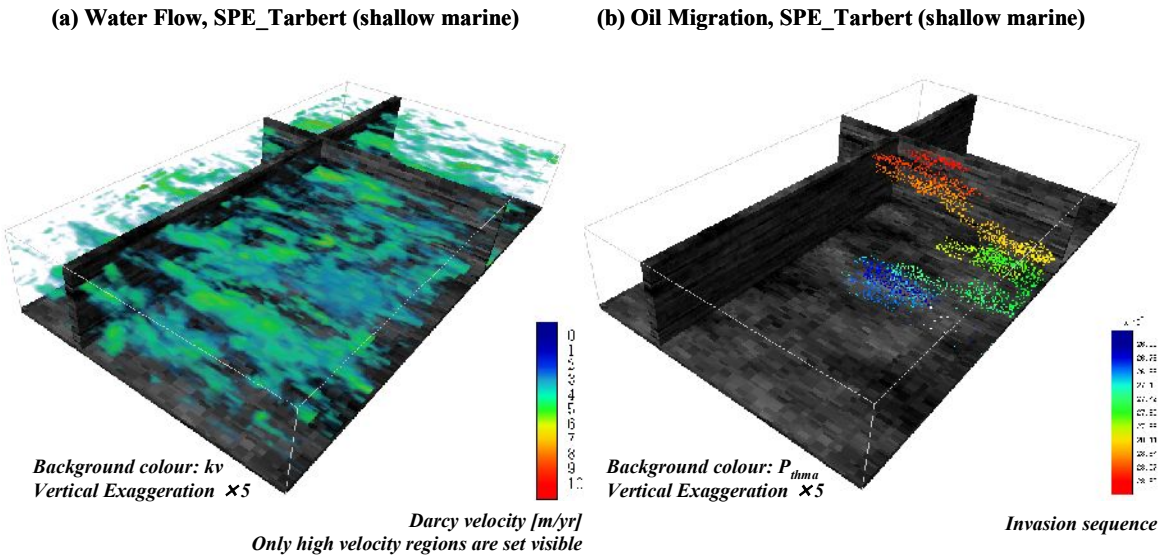

Figure 4.15 Water and oil flow simulation results for geostatistical model "SPE_Tarbert" (Figure 4.9(a)). (a) Darcy's velocity of steady state water flow. High velocity anomalies correspond to sand-dominated regions. (b) Oil migration pathway colour-coded by invasion sequence. Note that only part of sand-dominated regions is used as migration pathways.

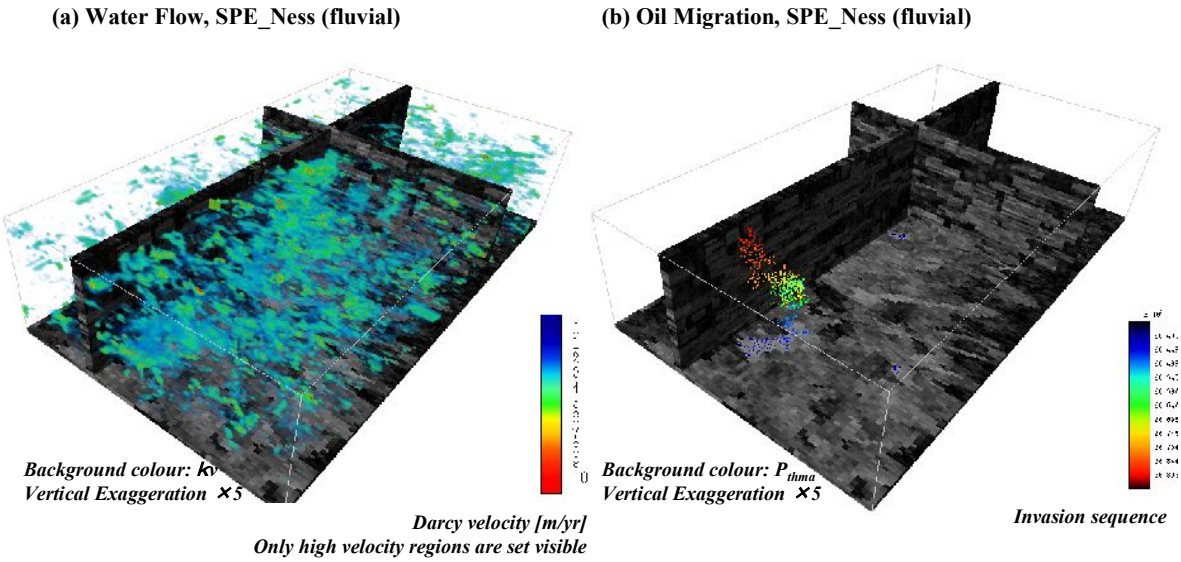

Figure 4.16 Water and oil flow simulation results for geostatistical model "SPE_Ness" (Figure 4.9(b)). (a) Darcy's velocity of steady state water flow. Individual high velocity anomalies are smaller than those in SPE_Tarbert (Figure 4.15 (a)), reflecting the difference in depositional facies. (b) Oil migration pathway colour-coded by invasion sequence. Rather vertical migration pathway was formed to percolate the model volume.

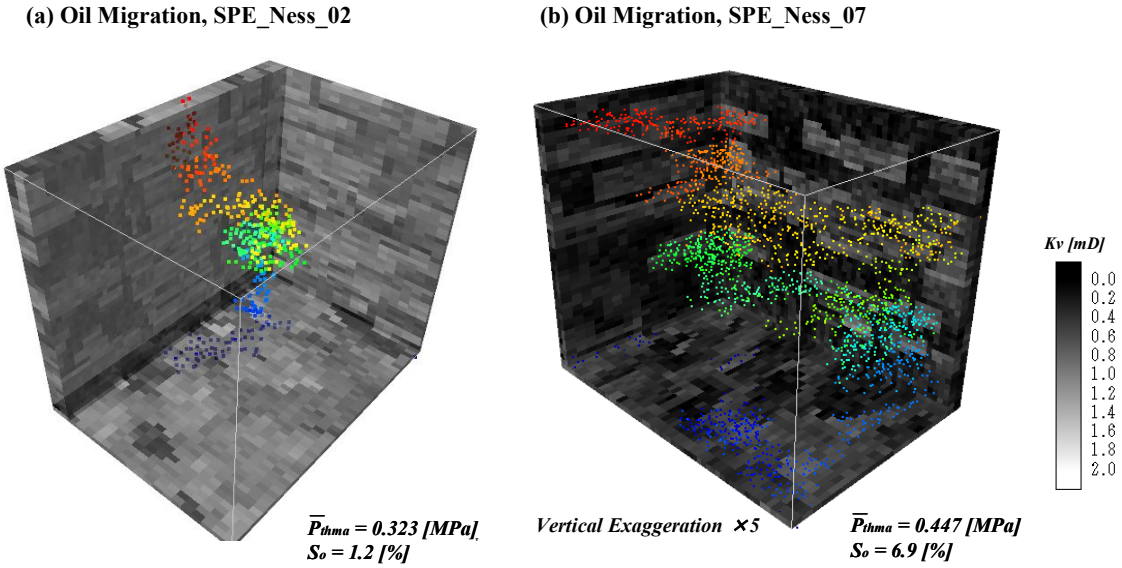

Figure 4.17 Results of oil migration simulations for sub-volumes of SPE_Ness. Invasion sequence for (a) SPE_Ness02, sand-dominated model, and (b) SPE_Ness07, mud-dominated model are shown. Migration pathway of SPE_Ness02 is identical with that of whole volume (SPE_Ness, see Figure 4.16 (b)). Migration pathway of SPE_Ness_07 is rather complex, resulting in higher residual oil saturation (S_o) than for SPE_Ness_02. Up-scaled capillary threshold pressure P_{thma} is higher for SPE_Ness_07 than for SPE_Ness_02.

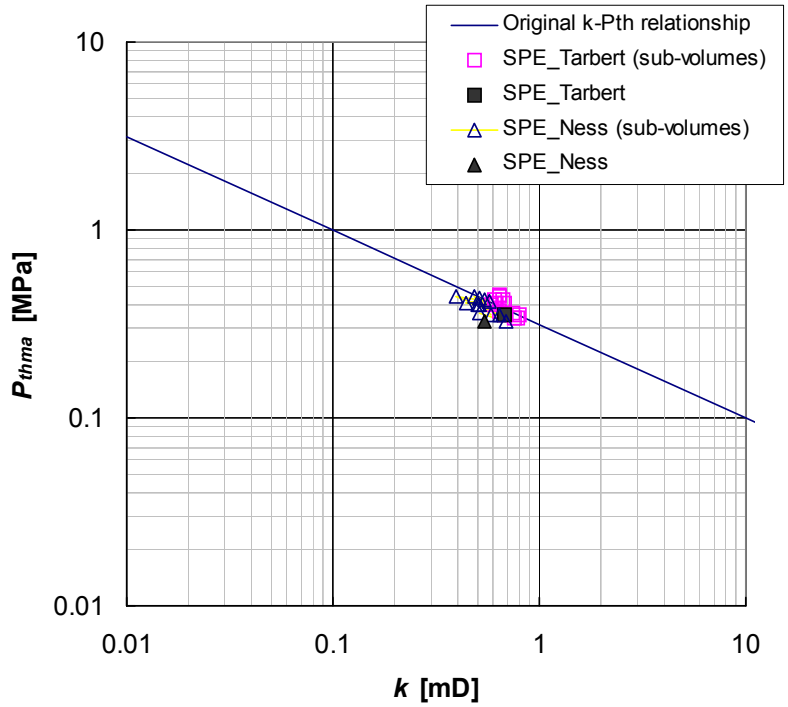

Figure 4.18 Cross plot of up-scaled permeability k and capillary threshold pressure P_{thma} for geostatistical models.

4.3 Assessment of k- P_{th} relationship from regional studies

In this section, validity of regional-scale k- P_{th} relationship is examined by using field examples in which petroleum column height and formation pressure are known.

Regional-scale P_{th} can be directly calculated from the observed petroleum column heights. The only requirements to be met for proper estimation are that (1) they must be capillary-limited traps (Nakayama and Sato, 2002), and (2) sufficient petroleum must be charged in those traps.

On the contrary, regional-scale k can not be directly obtained from formation pressure data, but only by numerical simulations. It is because formation pressure is related to permeability via Darcy's law (equation 2.8 in Section 2.3.3), which means it is a function not only of permeability but also of the amount of water influx and outflow, and of changes of those parameters in geological time. For example, different sedimentation rate (*i.e.* different rate of water influx squeezed from the sediments) results in different permeability estimation even if overpressure level is the same (Mann and Mackenzie, 1990).

Examples were collected from the fields with different proven petroleum column height and different overpressure level from the Norwegian Continental Shelf and Niigata basin, Japan, *i.e.* some of the fields used in Section 3.2 (**Table 3.1**).

4.3.1 Permeability estimation by pressure modelling

Regional-scale k is estimated from formation pressure data, by numerical pressure modelling. Pressure modelling here is different from the water flow simulation shown in section 4.2 in that it simulates pressure development over the burial history of the basin.

A commercial simulator MPath was used for the pressure modelling. The pressure generation is assumed to be caused by disequilibrium compaction, which is widely accepted as the principal cause of abnormal formation pressure (*e.g.* Osborne and Swarbrick, 1997). The simulator basically solves the diffusion equation (equation 2.13) to calculate formation pressure at each time step. By matching calculated pressure with observed pressure at well locations, regional-scale k will be obtained.

Figure 4.19 to **4.22** show the example of pressure modelling in the Haltenbanken, offshore Norway. The section traverses the highly overpressured Morvin discovery and the hydrostatic Åsgard field, which is based on Figure 22 of Ungerer *et al.* (1990). See **Figure 3.9** for location of the section line. The ϕ - k relationship (**Figure 4.19b**) was calibrated for the calculated pressure to match with the observed pressure data at two wells on the section line (**Figure 4.22**), and k values at the seals of the Morvin and Åsgard (hot shale of

Figure 4.19) were estimated as 2.E06 mD and 5.E07 mD, respectively (**Figure 4.23**). Note that the difference in k for the two fields is attributed to the difference in porosity, *i.e.* porosity in the overpressured Morvin is higher than that in the hydrostatic Åsgard (**Figure 4.21a**).

4.3.2 k- P_{th} relationship from regional studies

Figure 4.23 shows that the regional-scale k and P_{th} have a close mutual correlation, which overlaps the same plot derived from published core-scale k and P_{th} (**Figure 4.2**). This indicates the scale-independency of k and P_{th} correlation, as was demonstrated in section 4.2.

However, the points from the Niigata basin are plotted in a different region from those from the Norwegian continental shelf. The difference in k for a given P_{th} exceeds an order of magnitude, or the difference in P_{th} for a given k reaches several times. It means, even if one correctly estimates the permeability from pressure data, prediction of the column height can be totally wrong by using an inappropriate correlation curve.

Since the scale dependency is already ruled out, the difference in k - P_{th} correlation is most likely attributed to the difference in sedimentary facies of the seal rocks. This fact illustrates that reconstructing facies model (not only for sandstones but for mudstones) is extremely important to properly employ the k - P_{th} relationship as a predictive tool.

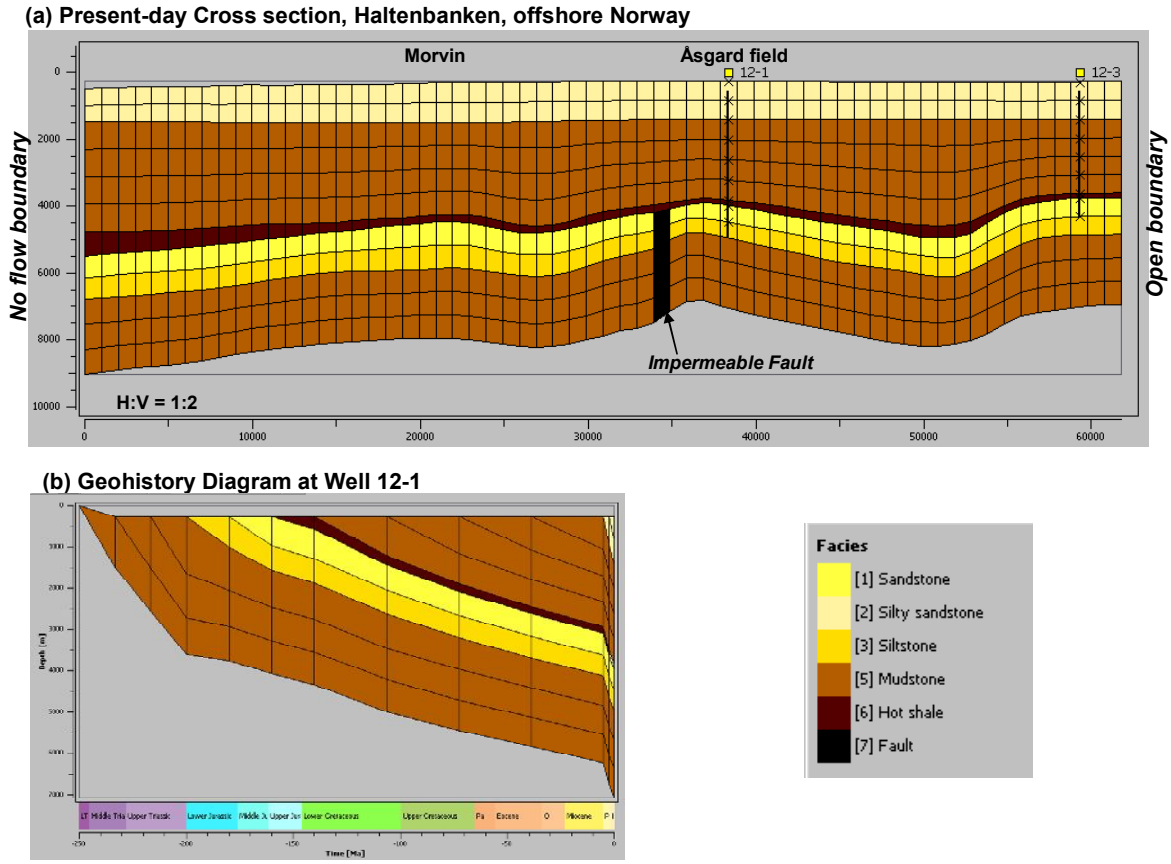

Figure 4.19 Haltenbanken cross section model (a) and geohistory diagram at well 12-1 (b). The cross section is based on Ungerer *et al.* (1990). Lithology and geological age are from Norwegian Petroleum Directorate released well dataset. The model is divided into 744 grid cells (62 by 12). Note that the boundary conditions are set open at the top and right, whereas closed at the bottom and left to reproduce Ungerer *et al.* (1990) model. See Figure 3.9 for location of the section.

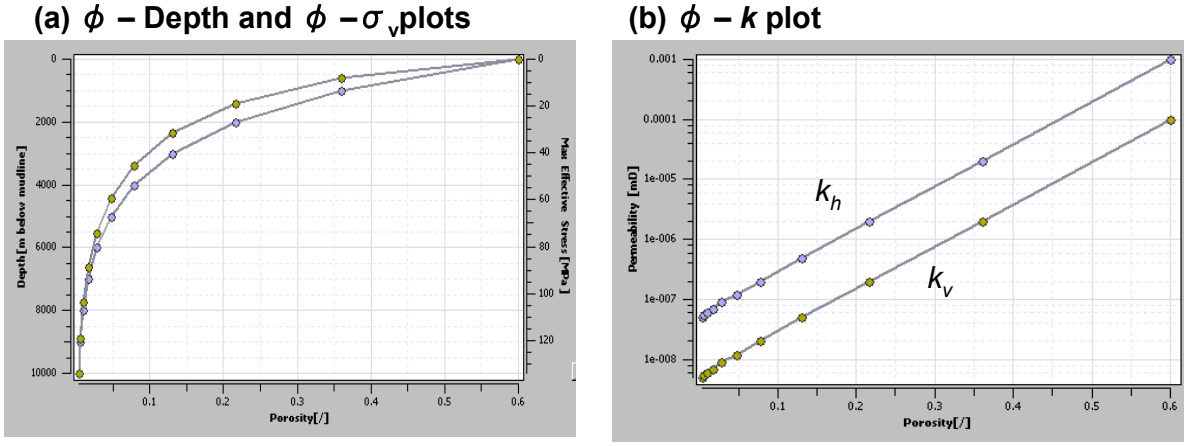

Figure 4.20 Input $\phi - \sigma_v$ and $\phi - k$ for pressure modeling, Haltenbanken.

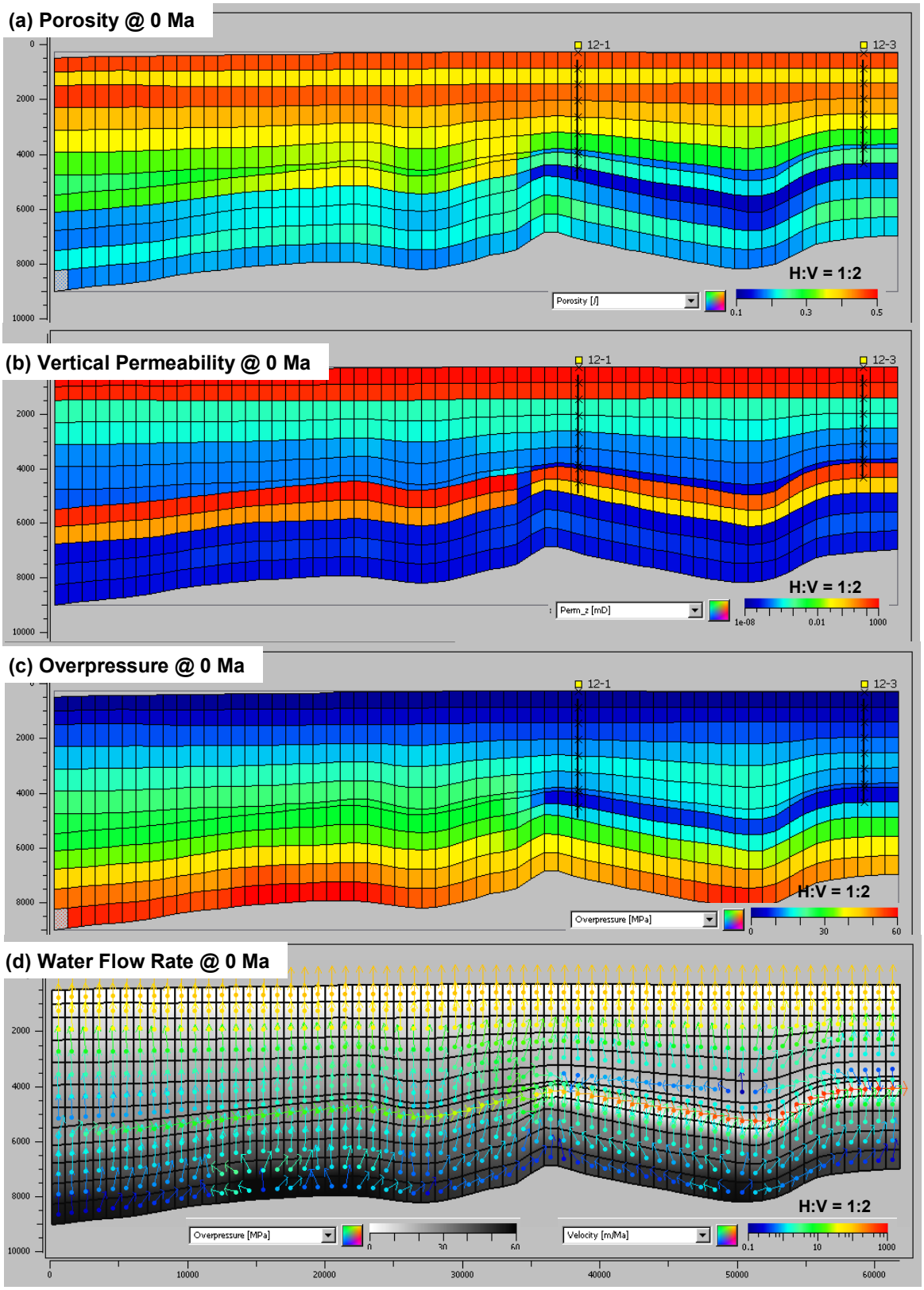

Figure 4.21 Results of pressure modelling in Haltenbanken. (a) Porosity, (b) vertical permeability, (c) calculated overpressure and (d) water flow rate at present-day.

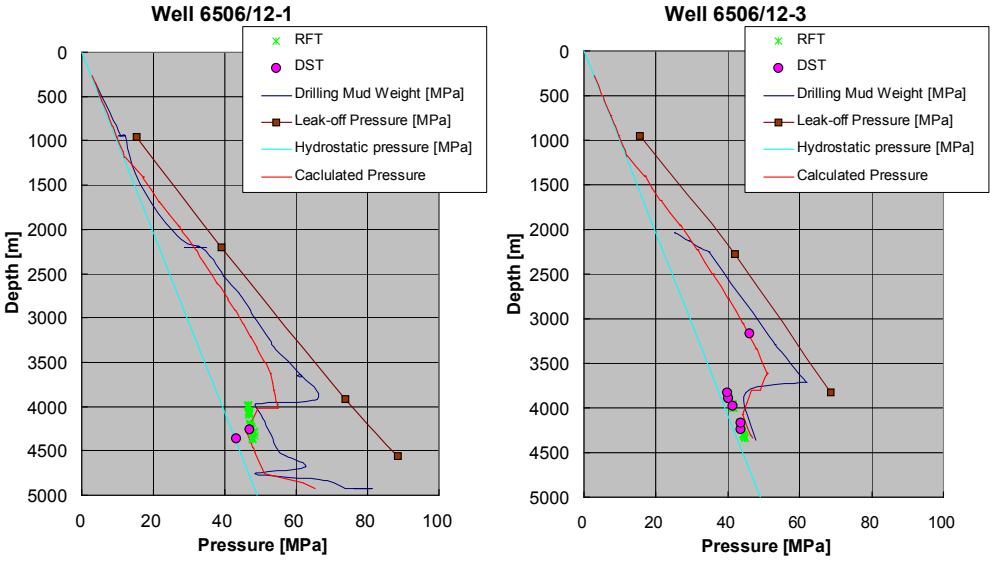

Figure 4.22 Calculated pressure profiles at well locations, Haltenbanken.

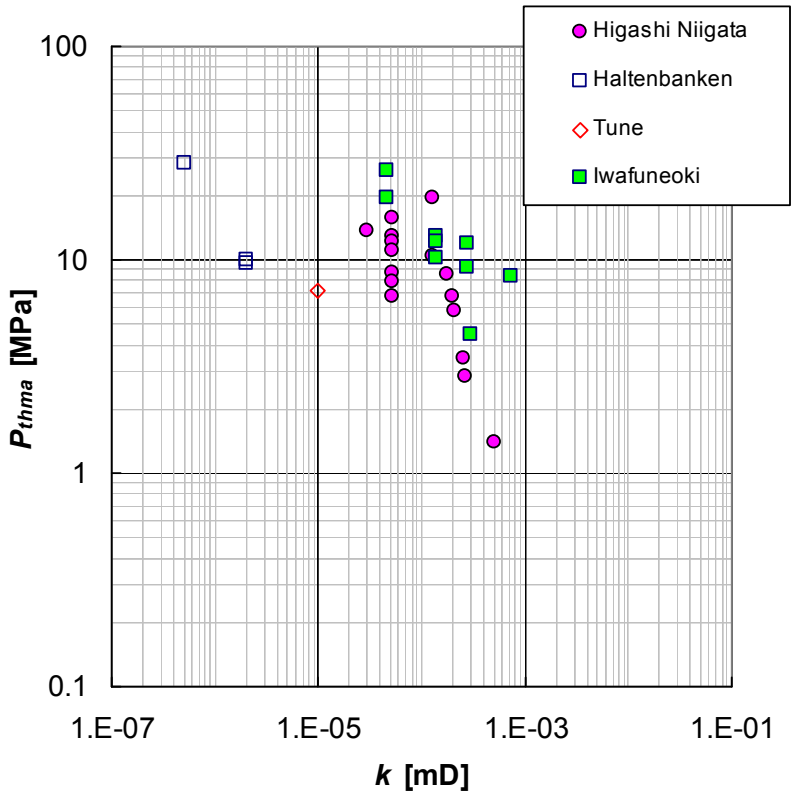

Figure 4.23 Regional-scale permeability k and capillary threshold pressure P_{th} plot from various fields. K for the Tune field is from Childs et al. (2002a). See Section 5.4 for pressure modelling in the Iwafuneoki field.

4.4 Optimizing petroleum migration models by using abnormal formation pressure

In this chapter, scale dependency of k- P_{th} relationship was examined by a series of numerical simulations and regional studies, and it was concluded that the k- P_{th} relationship is scale independent. If this conclusion is valid in all cases, it is extremely useful to optimize petroleum migration and entrapment models.

One of the most difficult challenges of petroleum migration and entrapment modelling is to optimize 3D distribution of P_{th} (for mudstone) throughout the basin's burial history, and it is the P_{th} that overwhelmingly controls the migration pathways and the final petroleum distribution. It is often the case that mudstone P_{th} is calibrated with a few proven column heights in the field studied or with limited number of laboratory measurements for mudstones at best. That is, the lack of calibration data is the major problem we face. In addition, if the laboratory P_{th} data are used for calibration, the difference in representative rock volume (*i.e.* core- vs. regional-scale) becomes another problem, as shown in the previous sections.

However, once the k- P_{th} relationship is established, abnormal formation pressure data can provide with additional calibration data for regional-scale P_{th}. The workflow should be (**Figure 4.24**):

(1) estimate the distribution of regional-scale k by pressure modelling, calibrated with abnormal formation pressure data

(2) then convert the estimated regional-scale k to regional-scale P_{th} by using the common (scale independent) k- P_{th} relationship, derived from either laboratory or field data,

(3) finally conduct petroleum migration and entrapment modelling by using the optimized P_{th} distribution.

Note that formation pressure data are used here only for calibrating k and for calculating PVT (pressure, volume, temperature) in reservoirs, not for incorporating the hydrodynamic effects in petroleum migration and entrapment modelling.

Largest advantage in this workflow is the use of formation pressure data. Firstly, they can be obtained more easily and routinely by formation testing or even by wireline logging at well locations, than column heights, laboratory measurements, or other P_{th} data. That means k and hence P_{th} can be calibrated with more data. Furthermore, the k estimated from the pressure data is of regional-scale, and thus the resultant P_{th} is also of regional-scale which is directly applicable to petroleum migration modelling. That is why this workflow is extremely useful for practical evaluation of migration and entrapment for petroleum exploration purpose.

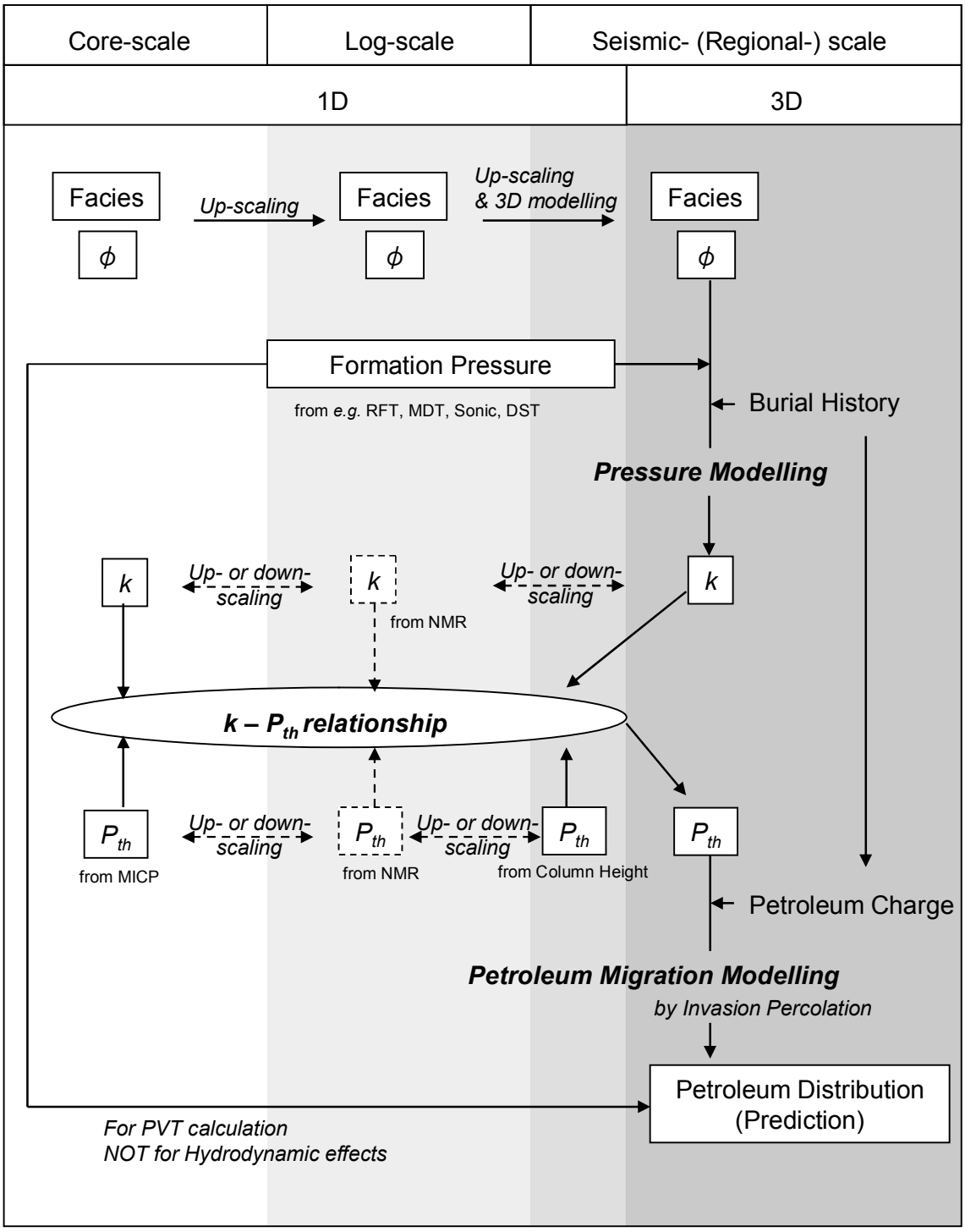

Figure 4.24 Workflow for optimizing petroleum migration modelling by using abnormal formation pressure data.

5 Petroleum migration modelling in the Iwafuneoki field, offshore Japan

In this chapter, the author would like to give an example of regional-scale petroleum migration modelling in the Iwafuneoki field, offshore Niigata, Japan. The objectives of this case study are to examine the validity, and to illustrate the applicability of the model proposed in the previous chapters:

(1) Abnormal formation pressure in reservoirs does not have a direct influence on petroleum migration and entrapment;

(2) However there are close mutual relationships between abnormal pressure and permeability, and between permeability and threshold pressure;

(3) Therefore the abnormal pressure can be used to predict capillary sealing capacity of the seal rocks for evaluation of petroleum migration and entrapment, and vice versa.

The chapter begins with a description of the database and an outline of the field. Formation pressure and capillary pressure of the reservoirs at well locations are summarized, which are used as calibration data for the simulations. Methods for estimating formation pressure and capillary threshold pressure from indirect information are also shown, which provide with additional calibration data.

It is followed by a description of the numerical models used, and the procedures to create them. They include building of the 3D model framework, distributing facies and rock properties, and estimating petroleum charge to the model volume.

After setting up the model, a series of numerical simulations are run. Pressure modelling is carried out first, to optimize permeability, and hence threshold pressure distribution by using the k-P_{th} correlation. Then petroleum migration simulation is performed by using the optimized P_{th} distribution. It is expected that the simulations can explain both pressure and petroleum distribution in the Iwafuneoki field, and give an insight for further exploration potentials.

A commercial software MPath was used in the simulation works (Carruthers, 1998; Moriya *et al.* 2007). See section 2.5 for algorithm of the simulator.

5.1 Database

A subset of a 3D seismic volume and 9 exploratory well data were used for constructing the geological models (**Figure 5.1**).

The seismic volume, which was inverted to relative acoustic impedance and converted to the depth domain, covers about 84 km^2 including the Iwafuneoki field. It is part of a 3D seismic survey conducted in 2002. Five horizon maps and two fault planes interpreted on

the seismic volume were also used.

The well data include horizon marker depths, wireline logs, formation pressure, and mercury injection capillary pressure (MICP) measurements for mudstone core and cuttings. Petroleum column heights for known pools are also used as calibration data.

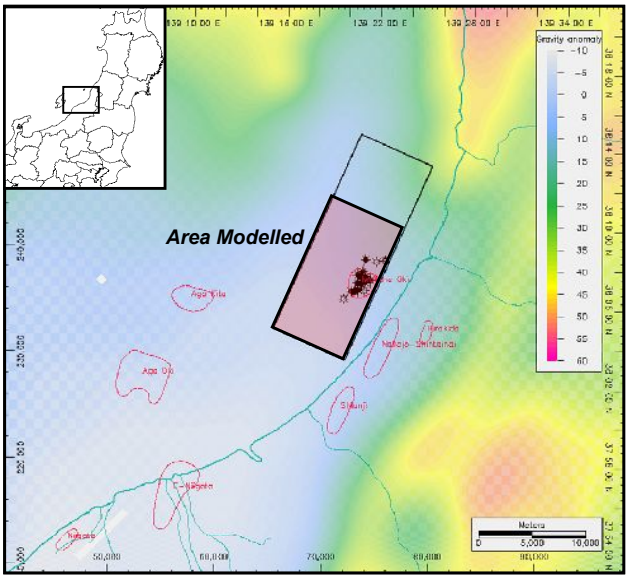

Figure 5.1 Location map of the Iwafuneoki field, offshore Niigata, Japan

5.2 Petroleum occurrence and formation pressure distribution

5.2.1 Hydrocarbon occurrence

The Iwafuneoki field produces oil and gas from several turbidite sand reservoirs of Pliocene age (Miyazaki *et al.* 1987; Moriya *et al.* 2007; **Figure 5.2**). The sands, deposited across the south-plunging Iwafuneoki anticline, form the stratigraphic traps as they shale out to the north, *i.e.* up-dip side of the anticline (**Figure 5.3, 5.4**).

Hydrocarbon occurrence in the field is rather complex. Both oil and gas are discovered, but in different reservoir intervals. Gas was found in the upper (sequence N3 to N5; Saito *et al.* 2008) and lower (sequence S4) reservoir intervals. In those sands, no ling oil is confirmed to date, except the lowermost sand in the upper reservoirs (sequence N3). On the contrary, the middle reservoirs (sequence N1 and N2) produce oil with no cap gas. The assumption of no cap gas for those reservoirs is supported by PVT (pressure, volume, temperature) analysis, which indicates the oil is under-saturated with gas.

Oil or gas column heights for individual pools are a couple of hundreds of meters, with more than 350 m for the N4 gas pool (**Figure 5.4**). The determined or estimated column height is not simply a function of the reservoir depth nor of petroleum phase and therefore not predictable by *e.g.* the equivalent grain size method of Nakayama and Sato (2002). This fact indicates that the seal capacity in the Iwafuneoki field varies from one pool to another, reflecting variation in facies or pore size distribution of the mudstones. Saito *et al.* (2008) pointed out that the seals for individual pools are correlative to condensed sections of depositional sequences identified in and around the field (**Figure 5.2**).

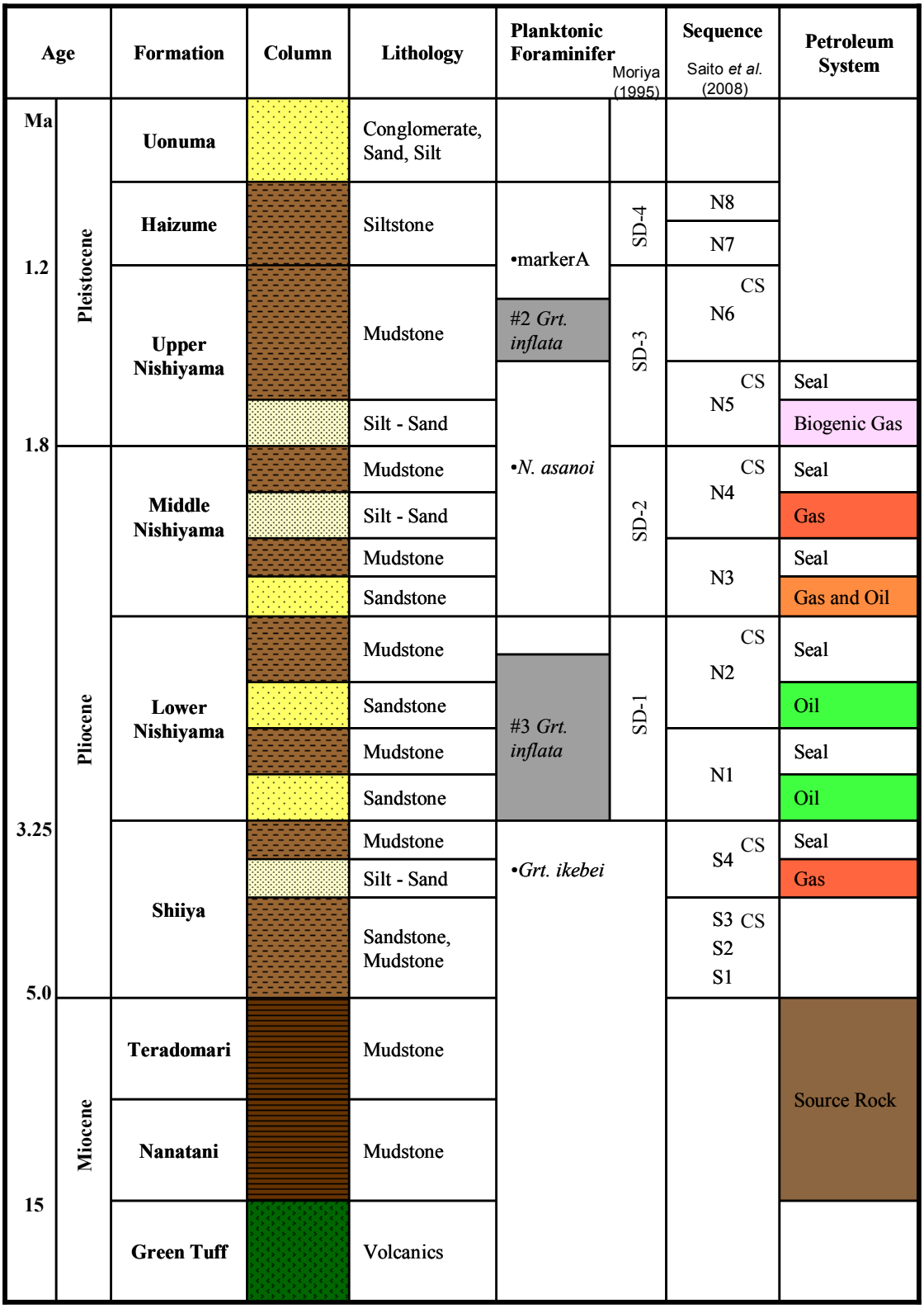

Figure 5.2 Generalized stratigraphic column and petroleum occurrence of the Iwafuneoki field. Geological ages are after Niigata Pref. (2000), Moriya (1995) and Miwa *et al.* (2004). CS in the depositional sequence column stands for condensed sections inferred from abundance of foraminifera (Moriya, 1995; Saito *et al.* 2008).

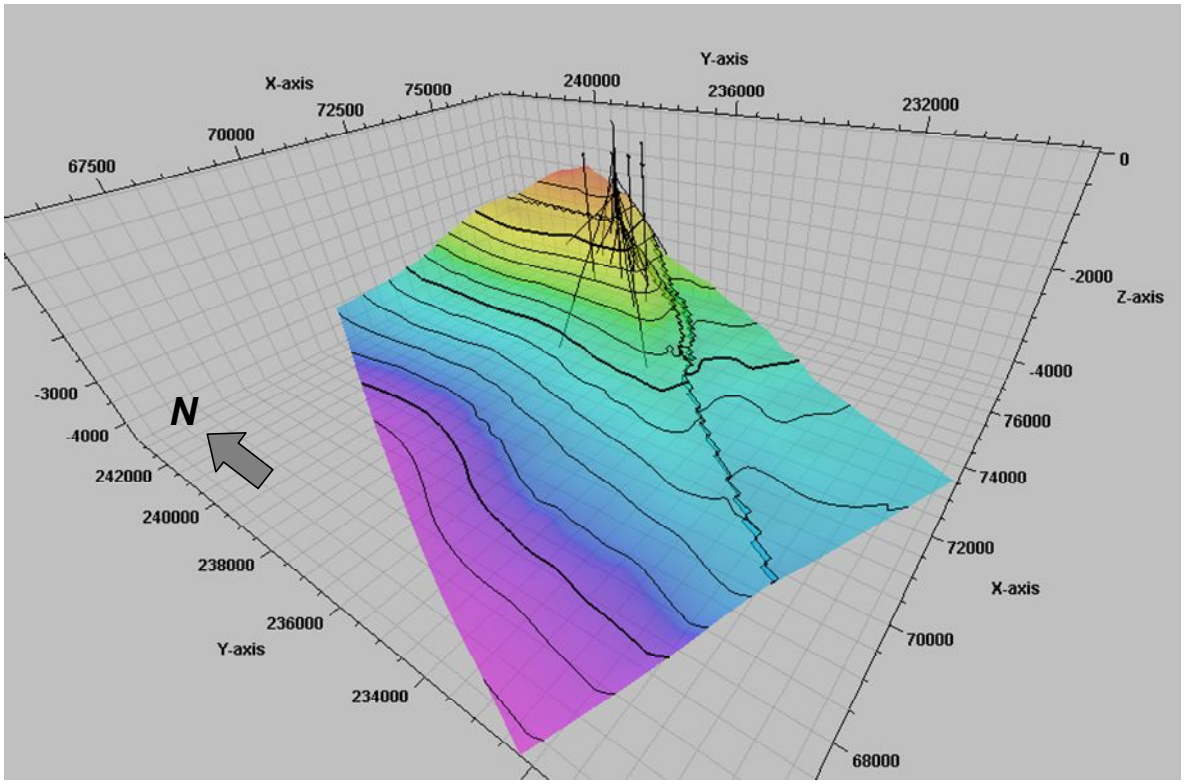

Figure 5.3 Depth contour map of the base Nishiyama Formation, Iwafuneoki field

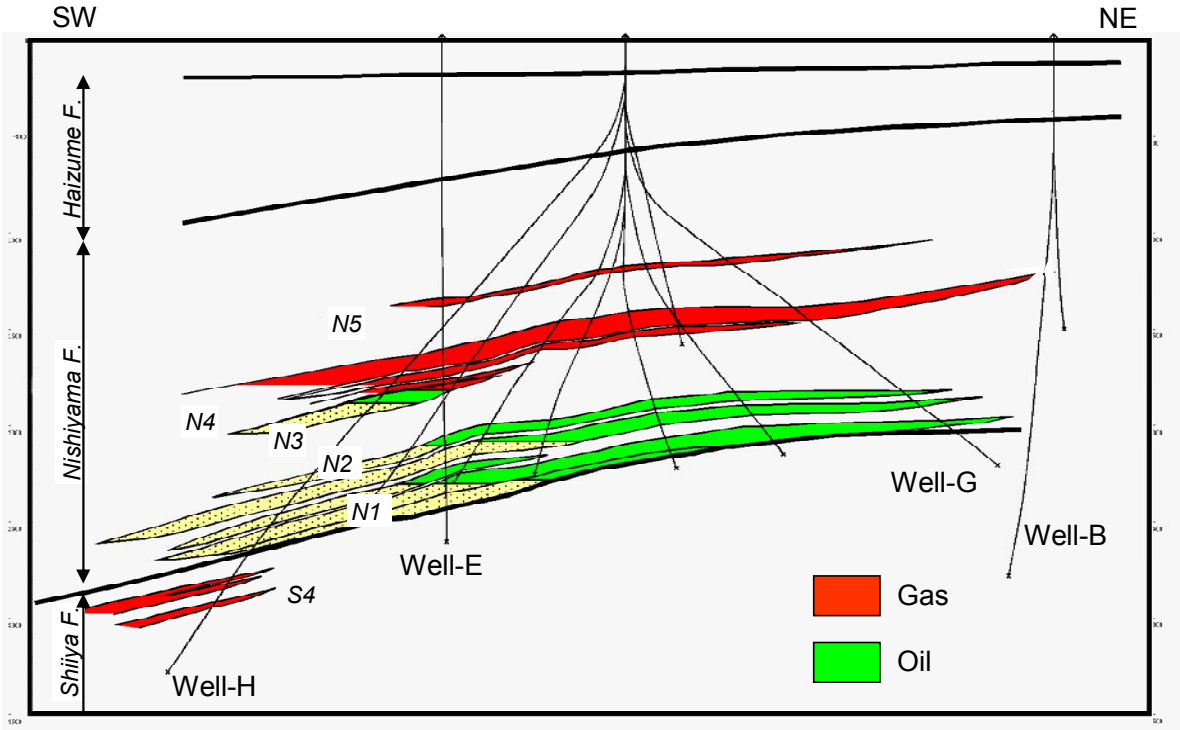

Figure 5.4 SW-NE cross section of the Iwafuneoki field.

5.2.2 Formation pressure distribution

Formation pressure profile derived from drill stem tests (DST) and wireline pressure measurements (RFT and MDT) at exploration wells shows that there exist several vertical pressure compartments with different water phase pressure. Pressure difference between adjacent compartments (or pools) is of the order of MPa, reaching 4 MPa at maximum for the seal between N2 and N3 pools. Note all the pressure data mentioned here were measured before the production started from those reservoirs, *i.e.* they are virgin pressures.

Pressure measurements are, however, not sufficient to draw continuous vertical pressure profiles for individual wells or to laterally correlate from well to well, as they are only available for productive or prospective reservoir intervals. The continuous pressure profiles for individual wells including mudstone dominated intervals are estimated by using sonic logs, which are most routinely logged for all the wells (**Figure 5.5** and **5.6**). Eaton's method (Eaton, 1975) was applied here to predict the formation pressure, optimizing his parameter "m" by fitting calculated pressure with measured pressure points.

$$P = S - (S - P_{hy}) \cdot \left(\frac{\Delta T_n}{\Delta T} \right)^m \tag{5.1}$$

$$P_{ex} = P - P_{hy} \tag{5.2}$$

where:

P [MPa]: formation pressure

P_{ex} [MPa]: excess pressure or overpressure

S [MPa]: overburden pressure determined by integrating density logs

P_{hy} [MPa]: hydrostatic pressure assuming water density as 1,000 kg/m^3

ΔT_n [μs/ft]: sonic transit time derived from the normal trend line for mudstone

ΔT [μs/ft]: sonic transit time for mudstone

m: constant (= 1.5 to 1.8)

The normal trend line was determined as an exponential curve calibrated with mudstone ΔT at shallower depths (~ 1,200 m±):

$$\Delta T_n = \Delta T_o \cdot \exp(-cz) \tag{5.3}$$

where:

ΔT_o [μs/ft]: sonic transit time extrapolated to the surface (205 to 220 μs/ft)

z [m]: vertical depth

c: compaction coefficient (0.00043 to 0.00048).

Spatial distribution of the estimated formation pressure clearly indicates the following (**Figure 5.6** and **5.7**):

(1) Overpressure generation starts in the Upper Nishiyama Formation at 1,000 to 1,500 m below sea level. Excess pressure reaches *ca.* 15 to 20 MPa in the Teradomari and Nanatani mudstones.

(2) Step-like increase of excess pressure occurs at mudstone dominated intervals, *e.g.* mudstones above S4, N1 – N2 and N3 – N4 reservoirs. In sand-dominated intervals, on the other hand, excess pressure profiles are almost vertical, indicating no overpressure generation in sands.

(3) The magnitude of overpressure for individual formations is similar over the field. That is, increase of excess pressure is almost parallel to the formation boundaries or other stratigraphic boundaries, rather than to the depth contours.

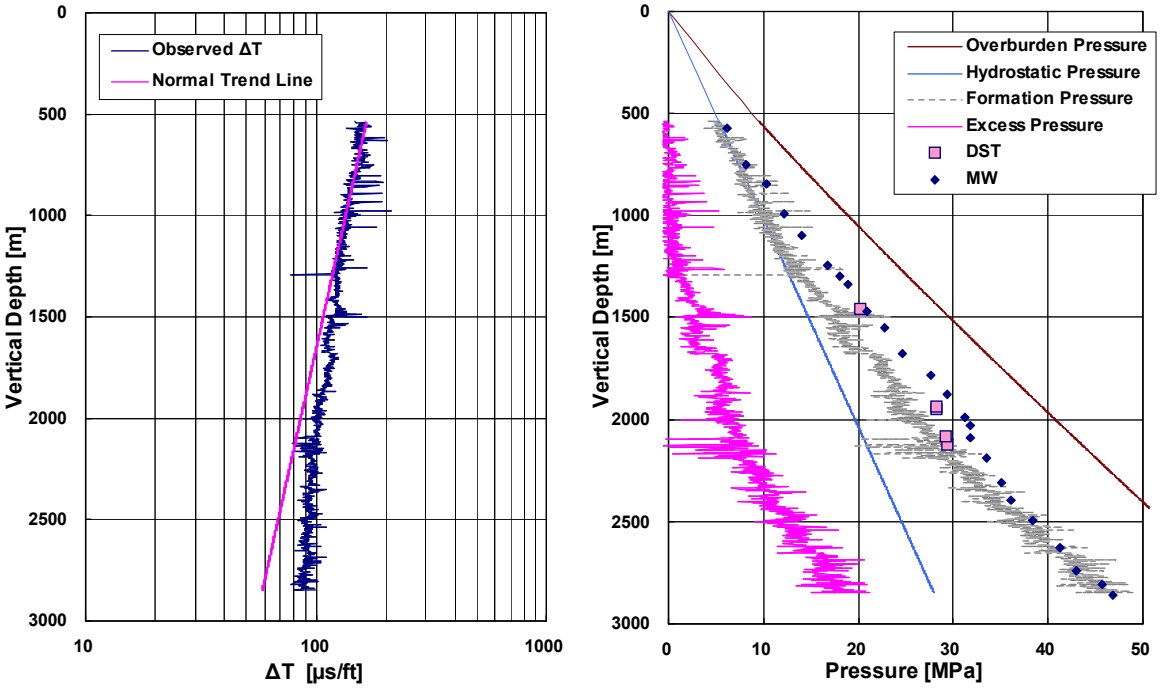

Figure 5.5 Formation pressure prediction from sonic logs, using Eaton (1975) method. (a) Observed sonic log (ΔT) and normal trend line determined from mudstone ΔT at shallow depths. (b) Calculated formation pressure profile. Overburden pressure S is estimated from density log. Pressures are calibrated with drill stem test (DST) and drilling mud weight (MW) measurements.

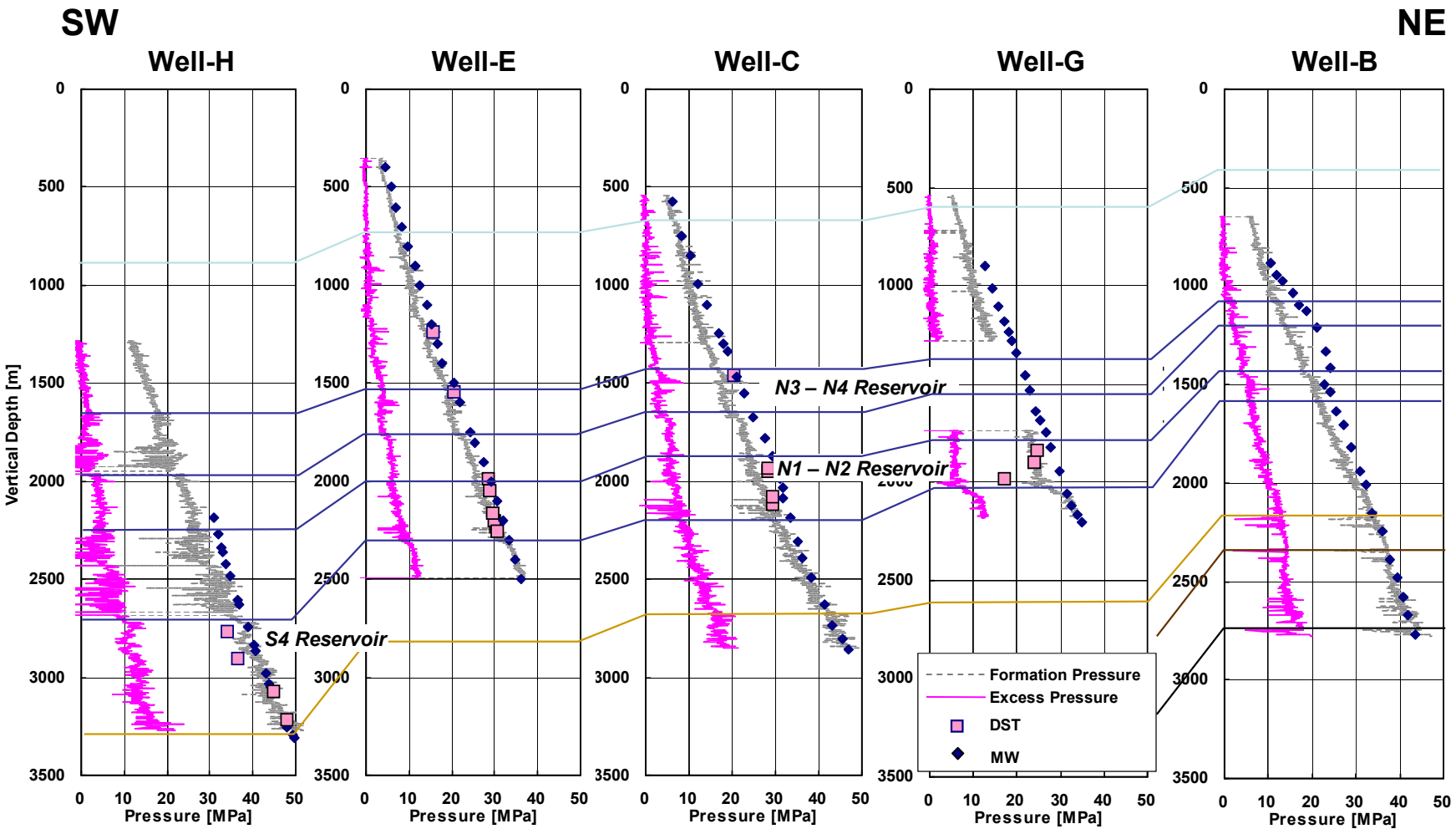

Figure 5.6 Formation pressure profiles predicted from sonic logs for 5 exploration wells. Observed pressures are considered to be initial pressures, except for well-G, where the data were taken after the production started from the reservoir interval concerned.

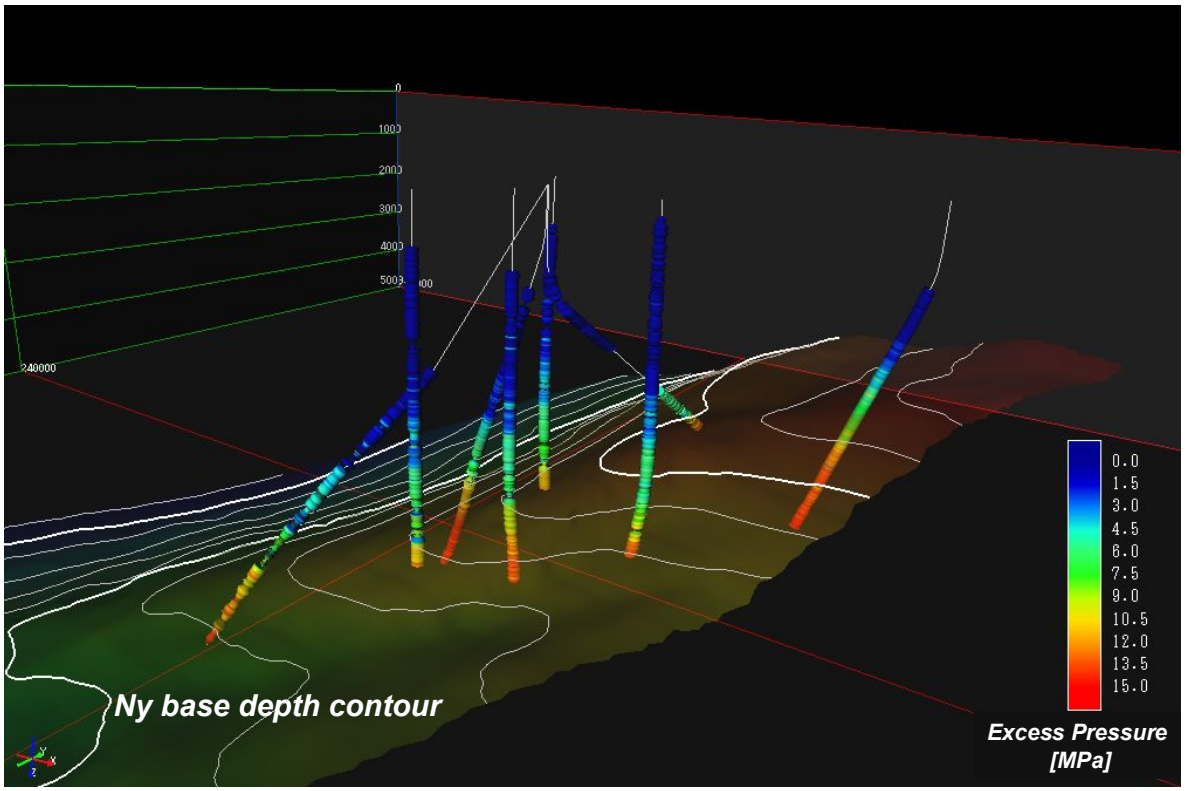

Figure 5.7 Excess pressure profiles predicted from sonic logs at exploration wells.

5.2.3 Relationship between petroleum column height and formation pressure

It is worth note that the seal interval with largest pressure difference (the interval above N2 oil pool) corresponds neither to the interval with highest sealing capacity (seal for N4 gas pool) nor the lowest one (seal for N3 gas and oil pool). That is, no simple relationship is established between the petroleum column height and pressure difference in water phase which the seal rocks can maintain (**Figure 5.8**). However, it is natural that this simple formulation collapses. It is the permeability vs. threshold pressure that a mutual correlation exists, not the resultant pressure and petroleum column height. Furthermore, both pressure and petroleum distribution in the field is related to water and petroleum influx to and outflow from the system, not just to the rock properties alone. Therefore, quantification of the mutual effects of rock properties (permeability and threshold pressure) and fluid influx/outflow by the numerical simulation is necessary to understand the pressure and petroleum distribution in the field.

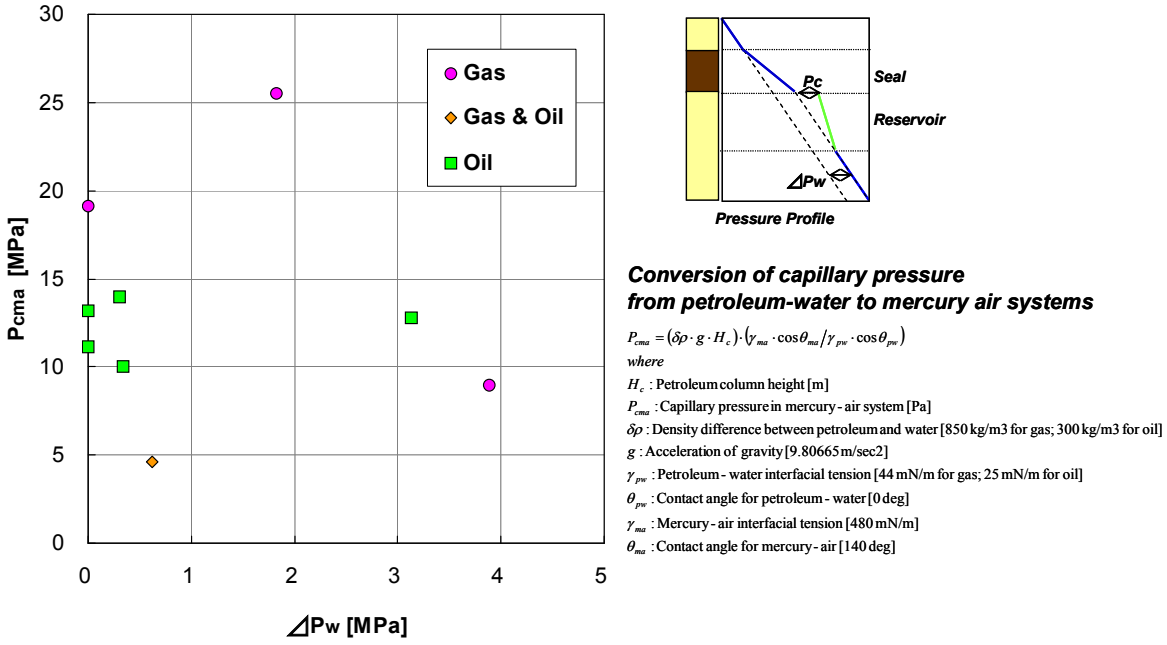

Figure 5.8 Pressure difference in water phase (ΔP_w) vs. sealing capacity shown as capillary pressure in mercury-air system (P_{cma}) for the Iwafuneoki pools.

5.3 Setting up the simulation model

5.3.1 Building 3D model and reconstructing burial history

Structural framework of the 3D model volume was built by stacking the horizon depth maps and fault planes, both of which were interpreted on the 3D seismic volume (**Figure 5.9**). The model has a dimension of *ca.* 12 by 7 km horizontally with the maximum depth of 6 km. It was then subdivided into *ca.* 3,400,000 grid cells, with 232 by 133 by 110 grid cells of approximately 50 by 50 by 10 - 100 m in size. The vertical segmentation is set finer for the Shiiya and Nishiyama Formations (*ca.* 10 - 20 m), than other formations (*ca.* 100 m), to achieve sufficient resolution in the reservoir intervals but still keep the model size as small as possible. In addition to this fine-grid model for the petroleum migration modelling, a coarser model with 60 by 35 by 28 grid cells was also created to perform the pressure modelling (see section 5.4).

The present-day structural model was backstripped to reconstruct a series of palaeo-structural frameworks (**Figure 5.10**). De-compaction was applied by assuming facies-dependent normal compaction curves (Sclater and Christie, 1980). See the following sections for definition of individual facies and determination of physical properties including porosity.

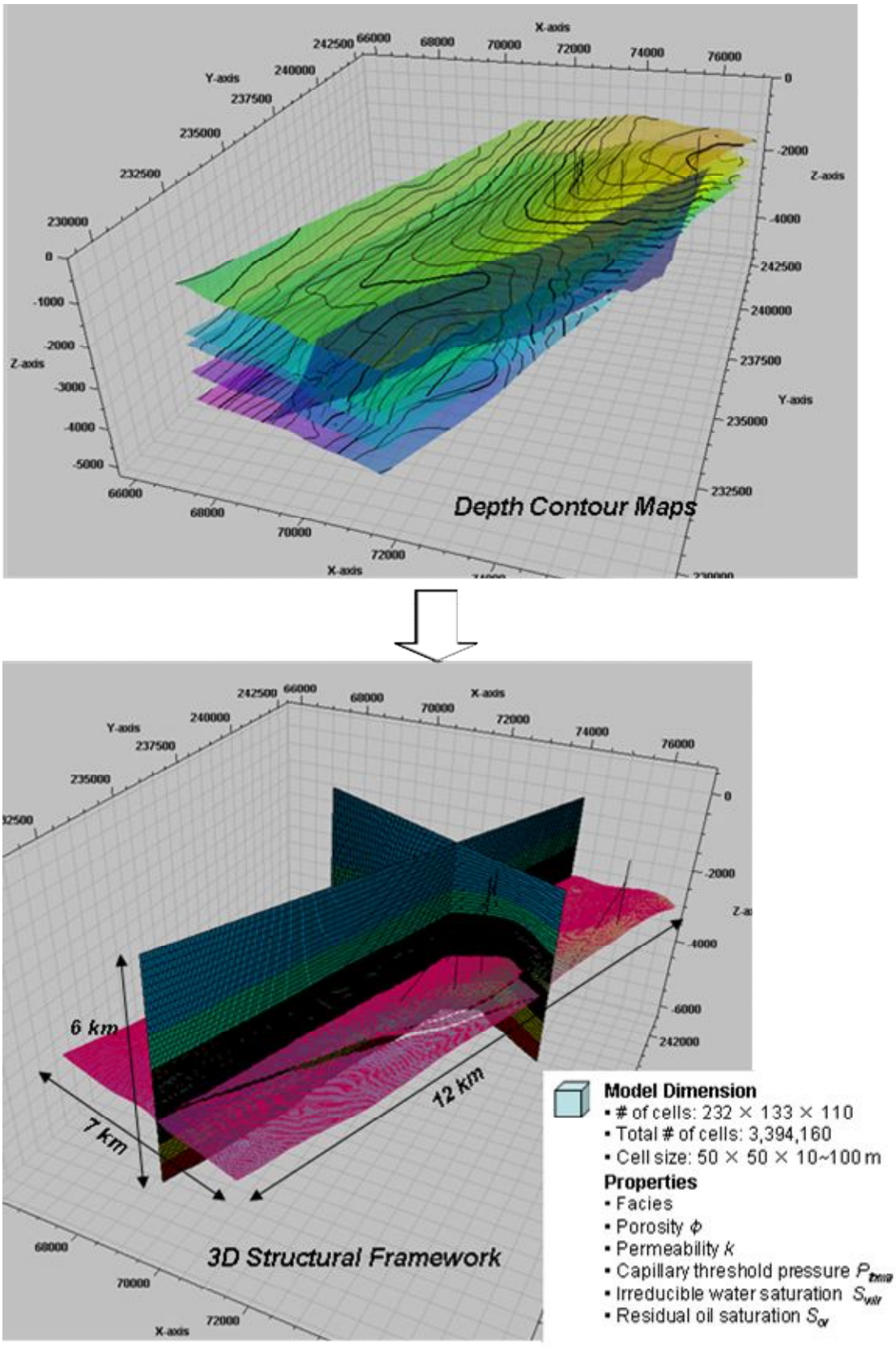

Figure 5.9 Construction of 3D geological model by using a series of depth contour maps and fault planes.

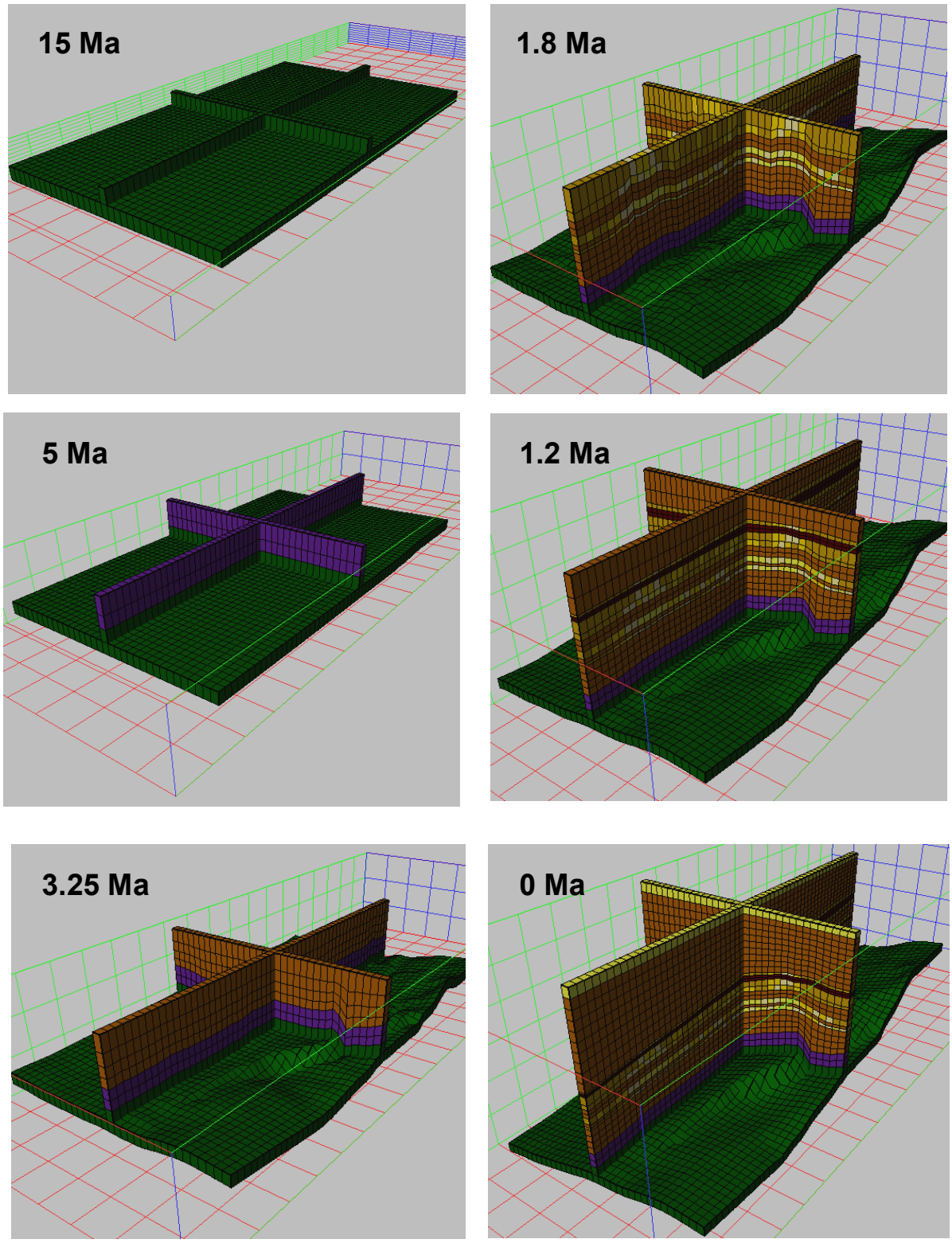

Figure 5.10 Structural backstripping for burial history reconstruction (Coarse-grid model with 60 by 35 by 28 cells).

Since the backstripping only restore the vertical depths for each time step, lateral movement of the rock mass can not be restored. It means that the thrust fault located on the eastern flank of the anticline was not reconstructed properly. However, the faults were active only from Miocene to Pliocene, as indicated by the seismic interpretation (**Figure 5.9**), earlier than the timing of petroleum generation and expulsion of this area (see Section 5.3.3). Therefore, the error in reconstruction of structural framework at the fault has only minimal influence on petroleum migration.

5.3.2 Distributing properties in 3D model

Once the structural framework through the burial history is constructed, a set of physical properties should be assigned for individual grid cells. They include facies, porosity ϕ, permeability k (both horizontal and vertical), capillary threshold pressure P_{th}, irreducible water saturation S_{wir} and residual oil saturation S_{or} (**Figure 5.9**).

Since some of the properties change with time as the grid cells are progressively buried, they must be defined to reflect the change in subsurface conditions during the burial history. Porosity ϕ is given as a function of vertical effective stress σ_v while k and P_{th} as a function of ϕ. S_{wir} and S_{or} are however set to be constant because they are not expected to change with burial. The functions to determine those properties are defined for individual facies and calibrated with observed or measured data at well locations.

(1) Facies

Six facies were defined: sandstone, siltstone, mudstone, condensed section, source rocks and volcanic rocks. The latter two are constituents of the Teradomari - Nanatani Formations and Green Tuff, respectively. The Shiiya and younger formations consist of other clastic facies, and they are determined at well locations from *Vcl* (clay volume) log: sandstone as $Vcl < 30\%$, siltstone as $30\% \leqq Vcl < 70\%$ and mudstone as $70\% \leqq Vcl < 100\%$.

Mudstone in the upper part of N4 sequence was however differentiated as the condensed section, because it has extremely higher sealing capacity than ordinary mudstone, as predicted from NMR log (see below).

Facies in the Shiiya and younger formations were populated in 3D by a geostatistical method (**Figure 5.11**). Sequential Gaussian simulation (Deutsch and Journel, 1998) was performed to distribute *Vcl* at well locations using the inverted seismic (acoustic impedance) volume as conditioning data. The main advantages using the geostatistical method include (1) it enables to incorporate the anisotropy in *Vcl* distribution as the variogram, (2) it can integrate seismic attribute and (3) the realized *Vcl* exactly matches with the *Vcl* log at well locations. Acoustic impedance volume was used as the conditioning

seismic attribute because it is most likely related to *Vcl* and facies in this area (Moriya *et al.* 2007).

The resultant *Vcl* volume was then converted to the facies volume according to the criteria shown above. Since it is a stochastic modelling, the sequential Gaussian simulation can produce equally-probable multiple realizations. Nevertheless, the facies in the area was represented here only by a single realization because it is beyond the scope of work to examine the uncertainty in the facies modelling.

(2) Porosity

Porosity ϕ is given as a function of vertical effective stress σ_v (**Table 5.1**; **Figure 5.12a-b**). First, for each of the facies, a normal compaction curve is defined as an exponential function of vertical depth under hydrostatic condition.

$$\phi = \phi_0 \cdot \exp(-c \cdot z) \tag{5.4}$$

where:

ϕ_0 [frac]: surface porosity

c: compaction coefficient

z [m]: vertical depth

It is then converted to the ϕ-σ_v curve, by using densities of rock and water (Sclater and Christie, 1980).

$$\sigma_v = S - P = (\overline{\rho}_b - \rho_w) \cdot g \cdot z \tag{5.5}$$

$$\phi = \phi_0 \cdot \exp\left(-\frac{c}{(\overline{\rho}_b - \rho_w) \cdot g} \cdot \sigma_v\right) \tag{5.6}$$

where:

P [Pa]: pore water pressure

S [Pa]: overburden pressure

$\overline{\rho}_b$ [kg/m^3]: mean bulk density

ρ_w [kg/m^3]: water density

g [m/s^2]: acceleration due to gravity, 9.80665 m/s^2

The constants ϕ_0 and c in equation 5.4 were optimized through the calibration runs with log-derived porosity at well locations. See section 5.4 for details of the calibration runs.

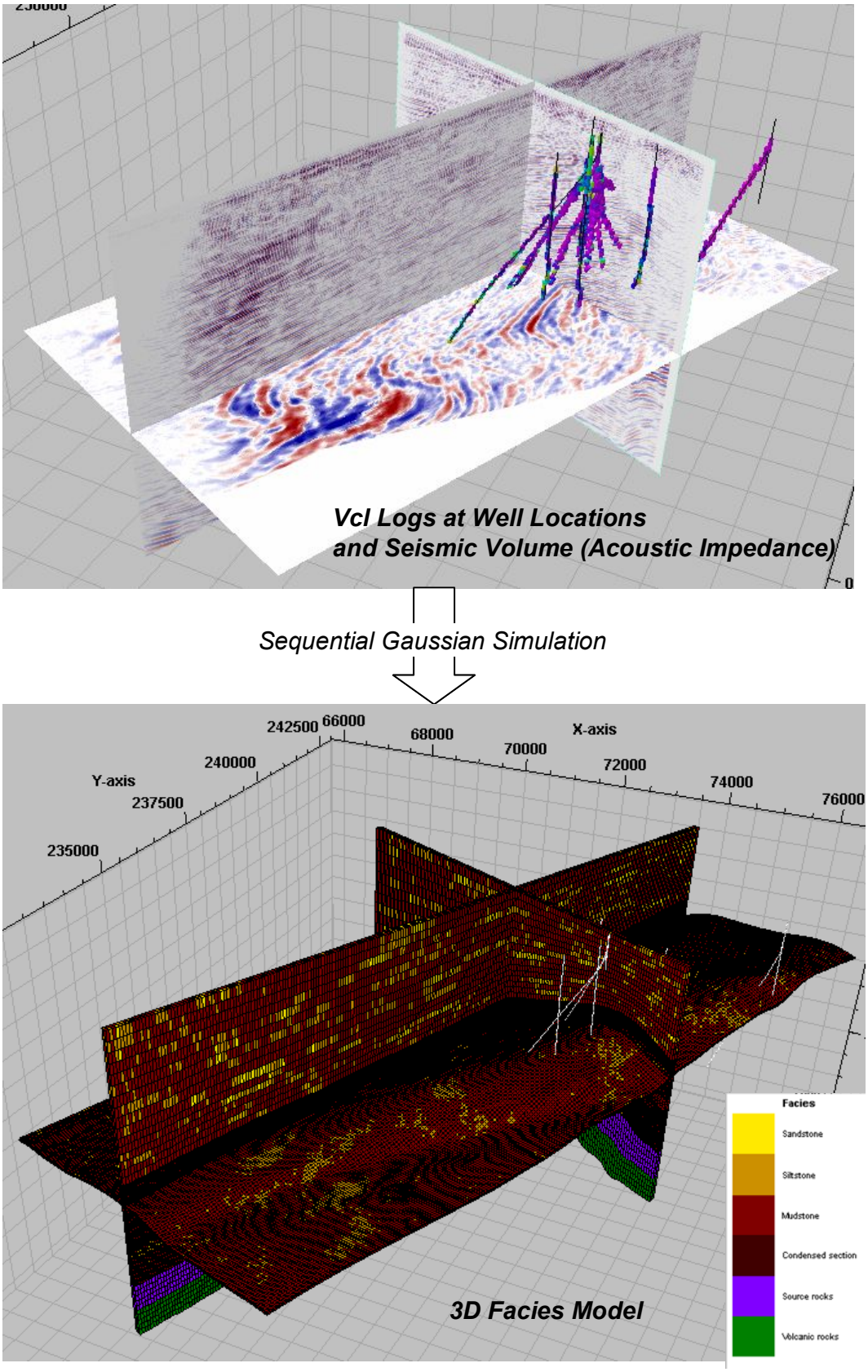

Figure 5.11 Facies modelling by sequential Gaussian simulation conditioned by inverted seismic data (acoustic impedance volume).

Table 5.1 Input parameters for the "Base Model"

Facies		Sandstone	Siltstone	Mudstone	Condensed section	Source rock	Volcanics
Matrix density [kg/m3]		2650	2680	2780	2780	2700	2650
Compressibility [%]		10	10	20	20	20	10
Matrix conductivity @20C [W/m/C]		3.5	3.5	2.2	2.2	2.2	3.5
Conductivity anisotropy		1.05	1.05	1.35	1.35	1.35	1.05
Matrix specific heat @20C [J/kg/K]		750	750	900	900	900	750
Matrix radiogenic heat [uW/m3]		0.8	0.8	2	2	2	0.8
Poisson's ratio		0.1	0.3	0.45	0.45	0.45	0.1
Depth - ϕ coefficients	ϕ_o	0.5	0.6	0.7	0.7	0.7	0.45
	c	0.0004	0.00045	0.00072	0.00072	0.00072	0.00035
ϕ - k_v coefficients	A	10	10	10	10	10	10
	B	-2.5	-4.5	-6.7	-7.7	-7.7	-2.5
k_v/k_h		0.1	0.1	0.1	0.1	0.1	0.1
Constant for P_{thma} from φ - k_v		0.18	0.18	0.18	0.18	0.18	0.18
Swc		0.2	0.4	0.85	0.9	0.9	0.2
Sor		0.05	0.05	0.05	0.05	0.05	0.05

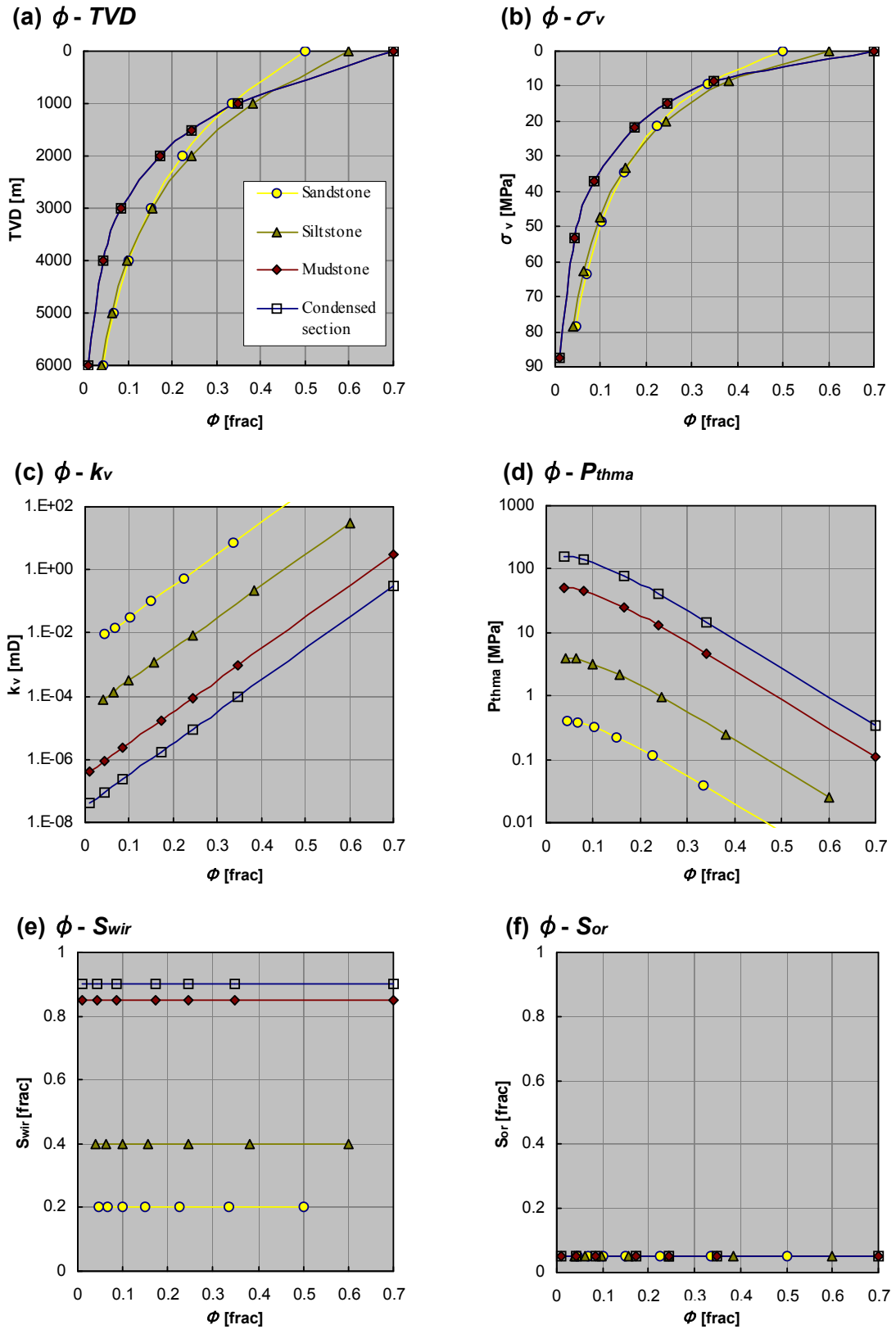

Figure 5.12 Physical properties assigned for individual grid cells in the "Base Model". They are given as functions of facies and porosity.

(3) Permeability and capillary threshold pressure

Optimizing k and P_{th} functions for mudstones is of particular importance for realistic pressure and petroleum migration modelling, respectively. On the contrary, that for sandstone is less important, because both k and P_{th} have sufficient capacity for water and petroleum to flow in any case.

All the available data which are directly or indirectly related to k and P_{th} for mudstones were used to calibrate the functions. They include petroleum column height of known pools, MICP measurements of mudstone cores and cuttings samples, and nuclear magnetic resonance (NMR) logs in mudstone dominated intervals.

Mudstone k and P_{th} from cores and drill cuttings

Despite a plenty of porosity and permeability data from cores and cuttings is available for sandstone, there are very few measurements for mudstone in the Iwafuneoki field. Moreover, the data were taken in 1983-1990, and the lower limit of measurable permeability at that time is 1.0E-17 m^2 or 0.01 mD, orders of magnitude higher than normal mudstone permeability. Thus it is difficult to predict mudstone permeability from the laboratory measurements.

As for the capillary pressure of mudstones, MICP was measured only for one well (well-I) drilled recently, by using side-wall cores (MSCT) and cuttings samples (**Figure 5.13** and **5.14**). P_{th} values from cuttings samples are apparently smaller than those from cores because of the sample surface irregularity of the formers (Sneider *et al.* 1997), and therefore corrections were made for the capillary curve to ignore mercury injections at very low pressures (**Figure 5.13**). Since the corrected P_{th} values are still rather small, further scaling has been made to match them with the values from cores at the same or similar depths (**Figure 5.14**). Despite of these correction and scaling, obtained P_{th} values from cuttings are correlative to P_{cma} values back-calculated from the observed petroleum column height. It indicates that P_{th} from cuttings can be used as calibration data at well locations, as well as that from cores and column heights.

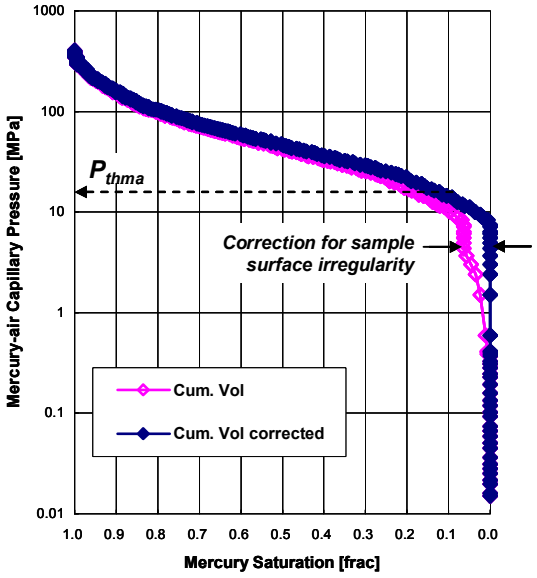

Figure 5.13 Example of mercury injection capillary pressure (MICP) measurement of mudstone cuttings. Correction was made for the capillary curve to ignore mercury injections at very low pressures, which were probably induced by sample surface irregularities (Sneider *et al.* 1997).

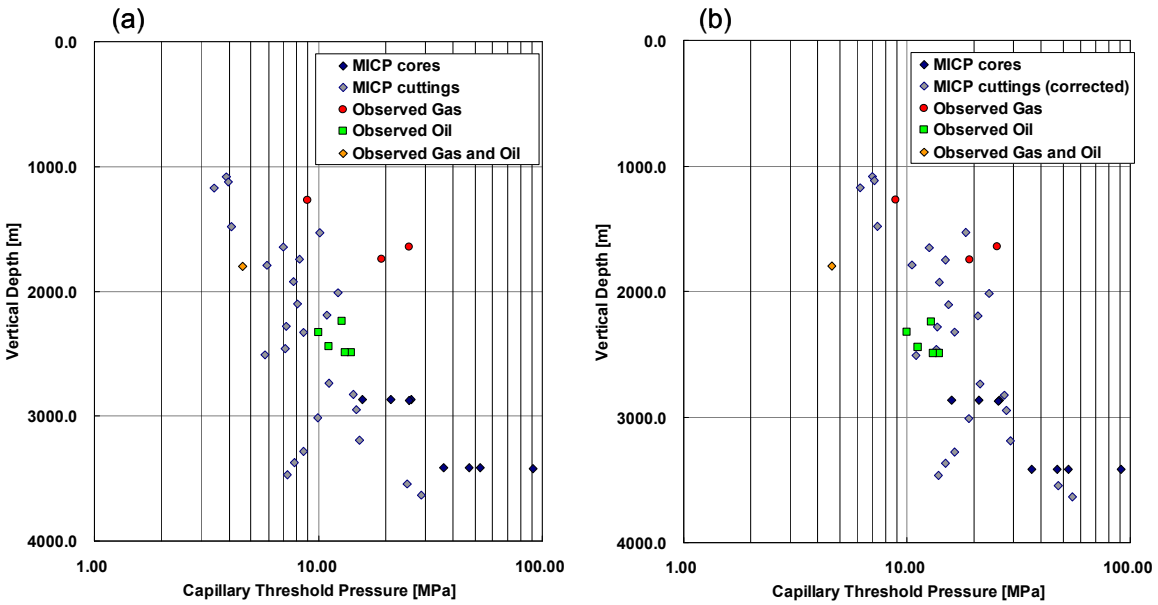

Figure 5.14 (a) Capillary threshold pressure P_{thma} of mudstones estimated from MICP measurement of cores and drill cuttings, well-I. Also plotted are capillary pressures for individual pools converted to mercury-air system (Depths are shifted to the reservoir top depths at well-I). (b) Same plot as (a) but P_{thma} from cuttings are scaled to match with that from cores.

Mudstone k and P_{th} from NMR logs

Nuclear magnetic resonance (NMR) logging measures properties related to pore-size distribution of rocks, and therefore it can be used to predict k and P_{th} (Kenyon, 1997; Volokitin *et al.* 1999). It is the only wireline logging tool to date which can measure those properties continuously along well paths. NMR logs for mudstone dominated intervals in well-I was used as additional calibration data for k and P_{th} (**Figure 5.15**).

The Timur-Coates model, one of the most widely used permeability estimators was applied here to obtain the NMR-derived k (Allen *et al.* 2000). It is calculated from the ratio of long- and fast-relaxing components of *T2*, indicating free and irreducible (or capillary-bound) fluid volume, respectively. That is, the model postulates that k is related to the relative volume of large and small pores.

$$k_{TIM} = a \cdot \phi^m \cdot \left(\frac{FFV}{BFV} \right)^n \tag{5.7}$$

where:

k_{TIM} [m^2]: permeability by Timur-Coates model

a: constants to be adjusted

ϕ : porosity [frac]

FFV: free fluid volume from NMR log

BFV: capillary-bound fluid volume from NMR log

m (=4) and n (=2): constants

It should be noted, however, that permeability estimation from NMR logs has the following limitations:

(1) NMR provides pore-body size distribution, whereas permeability and threshold pressure are controlled by pore-throat size. A single pore-body vs. pore-throat size relationship is assumed in the model, which must be valid only for ideal porous media.

(2) NMR is sensitive to bulk pore volumes, *i.e.* there is no information on how the pores are connected. Permeability and threshold pressure are, of course, related to volume and structure (tortuosity) of only the connected pores. Therefore, existence of isolated pores likely results in overestimation of permeability and underestimation of threshold pressure derived from NMR logs.

(3) The Timur-Coates model applies a simplified method and needs parameter optimization. It uses *FFV* and *BFV*, rather than incorporate whole *T2* distribution in the model and empirical cutoff values of *T2* are introduced for determining *FFV* and *BFV*. Moreover, there are some constants (a, m and n) which have to be determined.

Because of those shortcomings, permeability derived from NMR logs should be used as semi-quantitative data, and optimized by other calibration data. In this case study, it was calibrated with the P_{th} data from mudstone cuttings and also those estimated from

observed petroleum column heights, by using the k-P_{th} relationship (see Chapter 4), for there is no permeability data available for mudstones.

$$P_{thma} = 0.33 \cdot \sqrt{\frac{\phi}{k}} \qquad (5.8)$$

where P_{thma} is in mercury-air system in MPa and k in mD. After converting the measured or observed P_{th} data to k by equation 5.8, they are used as the calibration data for constant a in equation 5.7, and a = 21.6 was obtained as the optimal value (**Figure 5.15**).

As shown in the NMR-derived ϕ-k plot (**Figure 5.16**), there exist wide variety of mudstones in the field. In particular, there exists an interval with permeability of an order of magnitude smaller than others for a given porosity, *i.e.* the upper part of N4 sequence. In this case study, therefore, another type of mudstone, *i.e.* condensed section is defined for this interval, which has lower k for a given porosity than ordinary mudstone facies.

ϕ-k and ϕ-P_{th} functions

Permeability k is given as an exponential function of porosity ϕ for individual facies, which is the most commonly used empirical relationship (Dewhurst *et al.* 1998; **Table 5.1** and **Figure 5.12c**).

$$\log k_v = A \cdot \phi + B \qquad (5.9)$$

Constants A and B are determined by comparing with the measured data described above.

Once k is calculated by using equation 5.9, P_{th} can also be formulated with ϕ by equation 5.8 (**Figure 5.12d**).

$$P_{thma} = 1.2 \cdot \sqrt{\phi} \cdot 10^{-A \cdot \phi - B} \qquad (5.10)$$

Uncertainty in k and - P_{th}

As indicated by the NMR-derived k and P_{th} curves (**Figure 5.15**), they have high-frequency fluctuations due to slight facies changes which can not be represented in the reservoir-scale facies models. To incorporate these high-frequency fluctuations in k and P_{th}, ϕ-k and ϕ- P_{th} functions are given by probabilistic distribution. That is, k and P_{th} have normal distribution for a given porosity, and standard deviation σ is taken from that of the NMR-derived k and P_{th} curves (**Figure 5.17**).

(3) S_{wir} and S_{or}

Irreducible water saturation S_{wir} and residual oil saturation S_{or} are set to be constant because they are not expected to change with burial (**Table 5.1**; **Figure 5.12e-f**). S_{wir} varies with facies, *i.e.* sandstone has lower values while mudstone has higher. On the other hand, S_{or} are set identical for all the facies (default value of 0.05), because it is poorly constrained and more dependent on dimension of the model than facies (Carruthers, 1998).

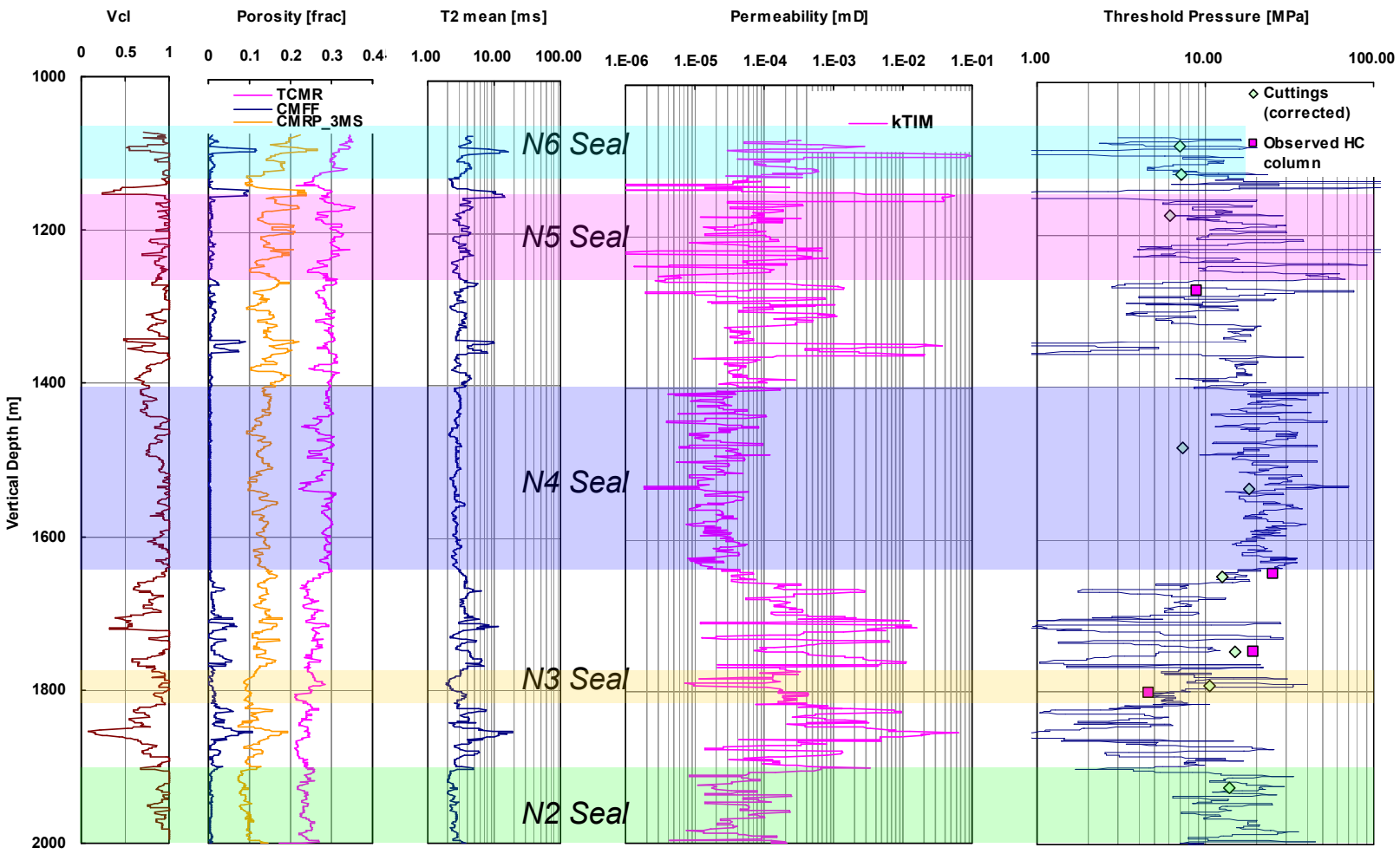

Figure 5.15 NMR log at well-I and predicted permeability k and capillary threshold pressure P_{thma} profiles. P_{thma} was calculated from kTIM (Timur-Coates permeability from NMR) and calibrated with that from observed petroleum column heights and MICP measurements.

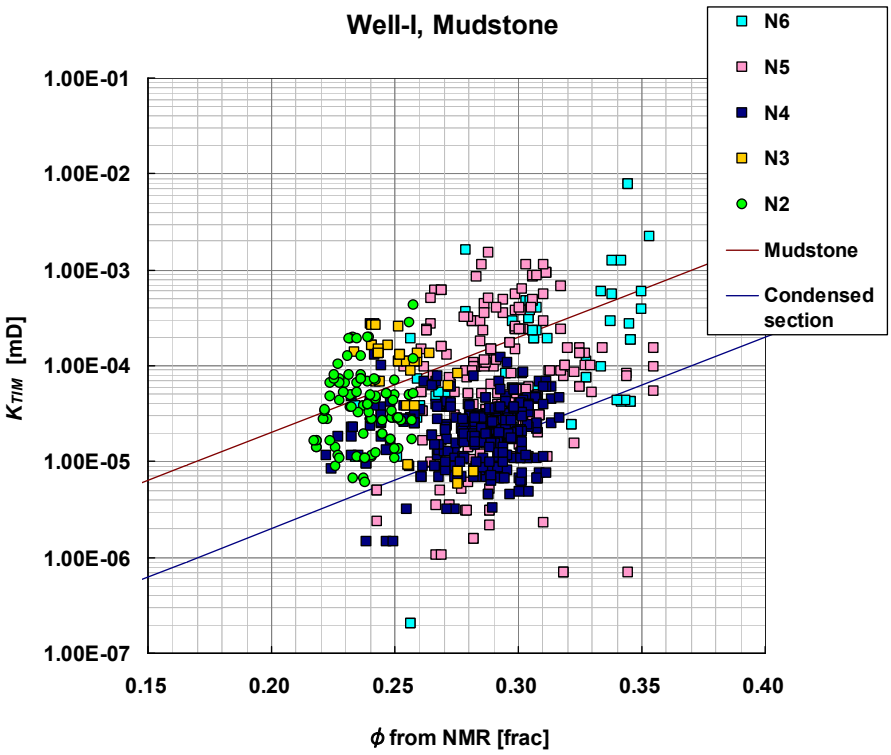

Figure 5.16 Porosity vs. permeability plot from NMR log, for mudstone, well-I. Lines represent ϕ - k correlations for mudstone and condensed section, used in the simulation model (Base Model).

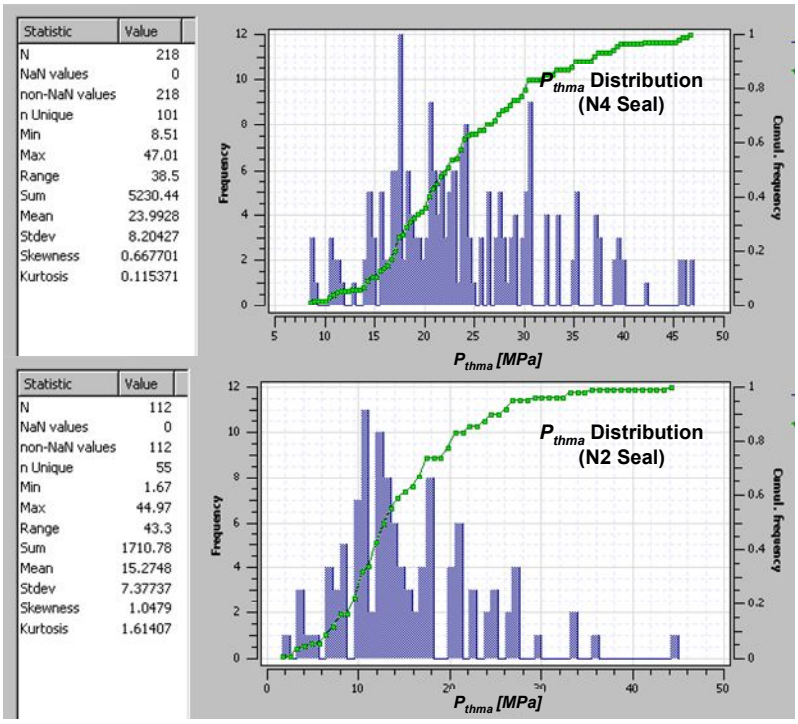

Figure 5.17 High-frequency fluctuations in P_{th} derived from NMR.

5.3.3 Petroleum charge

Petroleum generation and expulsion in the kitchen and charge to the model volume is another important input for the petroleum migration modelling. It was calculated by using pseudo-3D generation / expulsion simulation. In this research, mudstone in the Teradomari and Nanatani Formations is assumed as the source rock (**Figure 5.1**). Commonly adopted geochemical parameters for those formations are used for the generation / expulsion simulations, as listed in **Table 5.2**.

Results of generation / expulsion simulation are shown in **Figure 5.18**. Expulsion maps indicate the source rocks in the southwestern area is deeply buried during the deposition of the Haizume Formation and matured to expel sufficient amount of oil and gas to fill the Iwafuneoki pools.

Generation / expulsion simulation was run only inside the model volume, though the kitchen area of the Kitakanbara area, including the Iwafuneoki, likely extends to the basin centre (Saito *et al.* 2008). This limitation of simulation area fails to reproduce the pools in the Shiiya Formation, as pointed out by Moriya *et al.* (2007). However, the scope of the work is not to reproduce all the pools in the field, and it is sufficient to illustrate the applicability of the model only for the Nishiyama pools.

Table 5.2 Source rock parameters for petroleum generation modelling.

Source horizon	Teradomari+Nanatani
TOC [%]	2.0
Hydrogen index [mgHC/gTOC]	400.0
Kerogen type	II
Geothermal gradient [℃/100m]	4.2

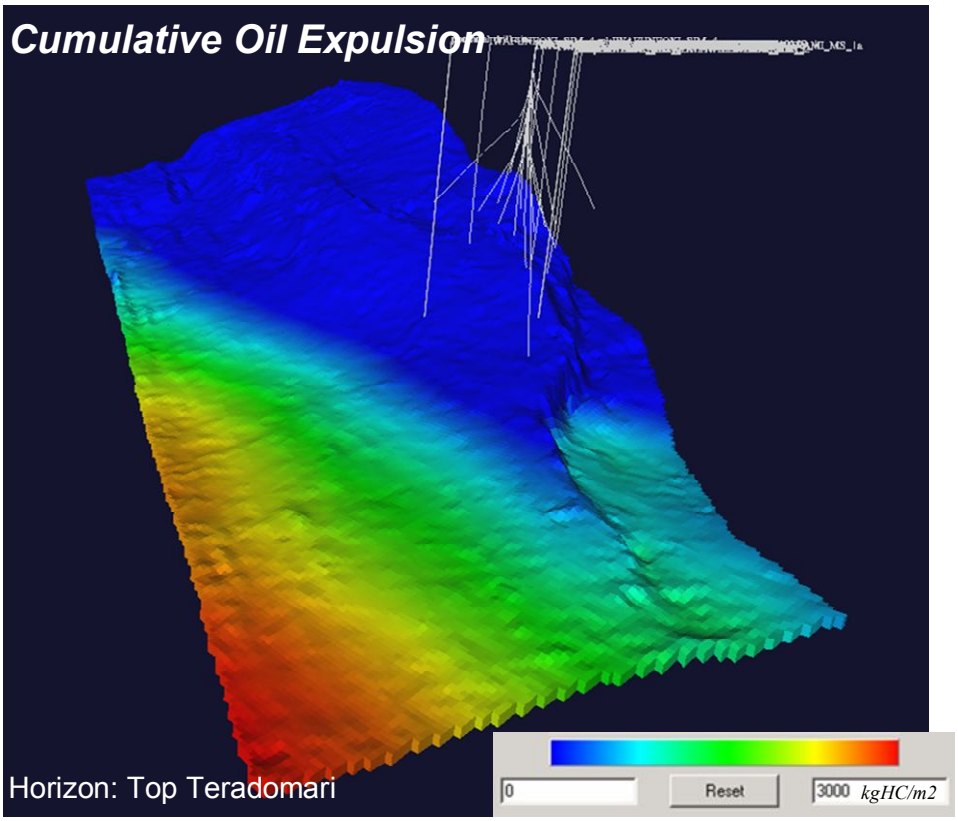

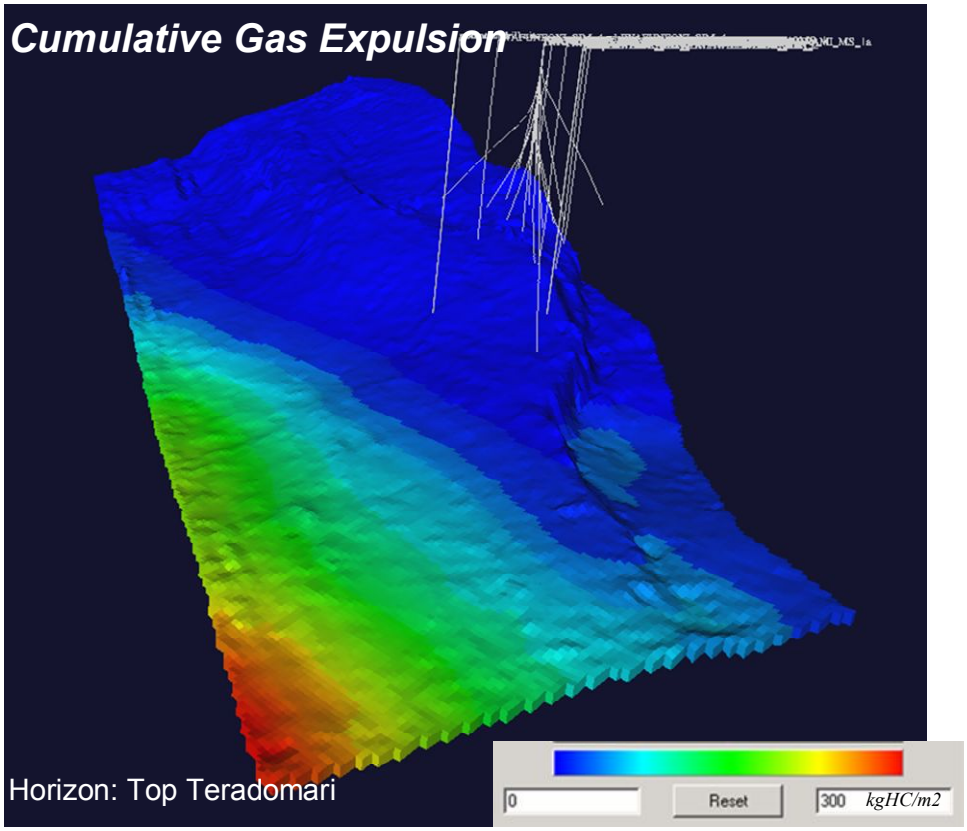

Figure 5.18 Cumulative oil and gas expulsion from the Teradomari and Nanatani source rocks, Iwafuneoki area.

5.4 Pressure modelling for parameter optimization

Pressure modelling is performed to calibrate the capillary threshold pressure P_{th} for petroleum migration modelling. The idea is, as mentioned before, to use abnormal pressure to optimize permeability of mudstones, and hence P_{th}, which is the key parameter for petroleum migration modelling.

Since the main cause of overpressure is attributed to the disequilibrium compaction (*e.g.* Osborne and Swarbrick, 1997) and that is the cause assumed in this simulation works, the most important parameters controlling the pressure distribution are the compaction curve and permeability. The former controls the amount of available water squeezed from the sediments, while the latter affects the rate of dewatering from the system. In this section, sensitivity of those two to the pressure development is discussed, and the ϕ-σ_v and ϕ-k relationships are optimized.

One of the problems with pressure modelling is its computing load to solve the diffusion equation (see section 2.3.3). It requires substantial computation time for running large 3D models. To maximize the efficiency of calibration runs, a test run was carried out for a coarse-grid 3D model first to verify the principal water flow directions, and then a series of calibration runs were conducted on a 2D section sub-parallel to the flow vectors, which must represent most of the water flow in the 3D model volume. After completing the calibration, 3D distribution of k and P_{th} throughout the burial history was reconstructed by the 3D pressure modelling with the optimized ϕ-σ_v and ϕ-k relationships.

5.4.1 Pressure modelling using coarse-grid 3D model

The coarse-grid model with 60 by 35 by 28 cells was used to examine the principal water flow directions. See **Figure 5.12a** to **c** for the parameters used and **Figure 5.19** for the calculated excess pressure distribution and water flow directions at present-day.

The result of pressure modelling clearly shows the following:

(1) Overpressure develops in deep mudstone-dominated intervals, *i.e.* the Nanatani – Teradomari and part of the Shiiya and Nishiyama Formations,

(2) Water flows from high to low excess pressure regions,

(3) Horizontal direction of water flow is sub-parallel to the structural dip while vertical component depends on the pressure gradient and k_v/k_h of the rocks, and

(4) Flow rate in sandstones is extremely high and it causes the flow anomalies.

The above observations indicate that we can practically use 2D section models parallel to the structural dips, instead of the full 3D, to reproduce pressure development of this area.

5.4.2 Parameter calibration and sensitivity analysis by 2D pressure modelling

Parameter calibration was performed by a series of pressure modelling on a NW-SE cross section, which crosses 3 well locations (**Figure 5.19**). The ϕ-*TVD*, ϕ-σ_v and ϕ-k relationships are optimized (**Figure 5.12a** to **c** and "Base Model" in **Figure 5.21** to **5.24**). Through the calibration runs, sensitivity of those parameters to pressure modelling was examined. As mentioned in the previous section, NMR-derived permeability indicates the existence of condensed section in the upper part of N4 sequence, which has lower k for a given porosity than ordinary mudstone facies. The effect of incorporation of this condensed section was also examined. See **Table 5.3** and **Figure 5.20** for the parameters given for the sensitivity analysis.

(1) Normal compaction curve for mudstone

Since the compaction curve controls the amount of water squeezed from the sediments, it has a significant influence on calculating formation pressure. Here it was calibrated with log-derived porosity curves at well locations, because of the lack of direct porosity measurements for mudstones.

Figure 5.22 shows the results of three pressure modelling with different normal compaction curves for mudstones (**Figure 5.20a**). Note that all other parameters are identical for those models. They illustrate that *ca.* 5% of porosity difference in normal compaction curve results in fairly different pressure profiles.

As permeability is optimized by matching calculated pressure with observed one, selection of inappropriate compaction curve results in inappropriate estimation of permeability, and hence threshold pressure for a given porosity. That is, if we take "Model01" curve instead of "Base Model," calculated pressure becomes too large compared with observation, and k needs to be increased in turn to match the pressures. This means inappropriately smaller P_{th} estimation than that of "Base Model".

(2) ϕ-k relationship for mudstone

Next, sensitivity of ϕ-k relationship was analysed. **Figure 5.23** shows the results of three pressure modelling runs with different ϕ-k relationships for mudstones (**Figure 5.20b**). As is expected, change in ϕ-k relationship has a direct influence on calculation of formation pressure. Shifting k by an order of magnitude for a given porosity completely loses the correlation between the calculated and observed formation pressure.

One thing interesting to note is that reducing input k for a given ϕ does not always result in the reduced value of calculated k (see k curve for Model04). This is because reducing input k promotes overpressure development, and overpressure in turn, prevent

porosity reduction. Since porosity is linked with k via ϕ-k relationship, larger ϕ consequently results in larger k than expected. This fact clearly demonstrates the necessity of numerical simulation to properly understand mutually-related phenomena.

(3) Incorporation of condensed section facies

Finally, the effect of incorporating condensed section facies on pressure modelling was examined. Permeability of condensed section is determined to be smaller than that of ordinary mudstone by an order of magnitude, based on the NMR-derived k (**Figure 5.17**). Three models are tested here; BaseModel with condensed section in the upper N4 sequence (calibrated model), Model05 with ordinary mudstone only, and Model06 with condensed section for all the mudstone intervals.

Figure 5.24 shows the results of those three pressure modelling runs. Contrary to one's expectation, the pressure profiles are almost identical if there exists condensed section or not (Base Model and Model05). That is, it is difficult to know if there is a condensed section interval only from pressure modelling, though the NMR-derived k tells us that the condensed section likely exists. It indicates that this method does not always work in all the situations but the sensitivity to k depends on the relative magnitude of porosity reduction and k of the interval in question. In fact, there are other intervals where k can be estimated much more precisely, *i.e.* at the bottom of the well (3,400 m – T.D., Base Model and Model05). This fact conversely reveals that integrating all the information, not just pressure, is extremely important for understanding the whole system.

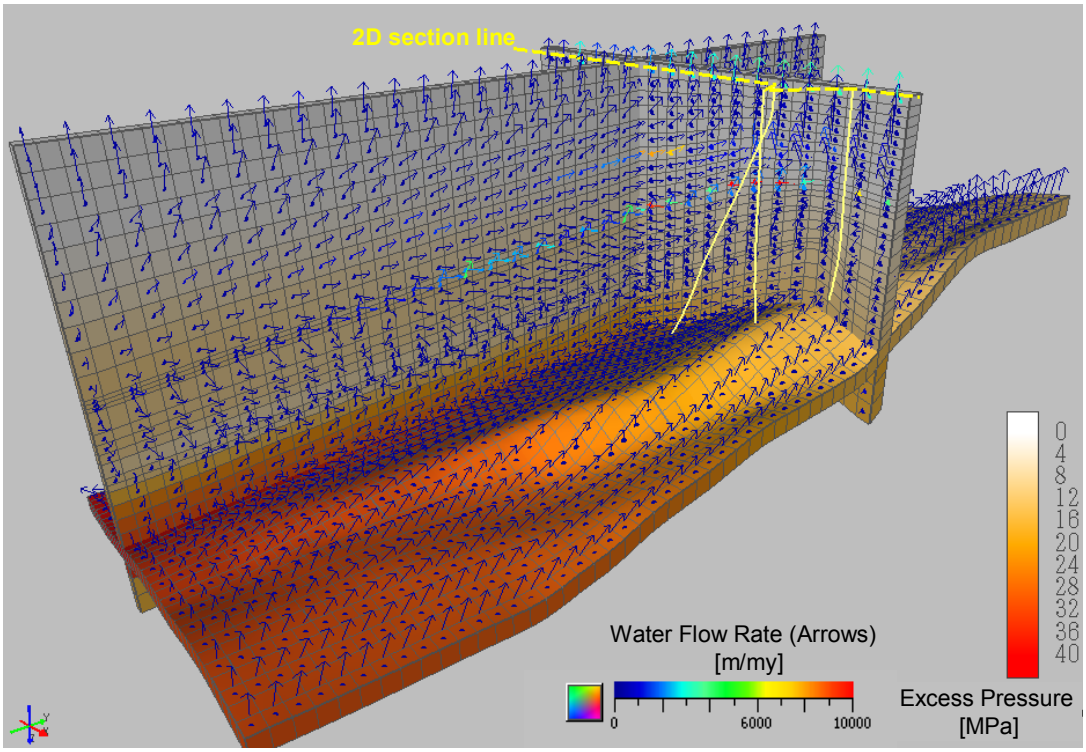

Figure 5.19 Water flow rate vectors superimposed on excess pressure distribution, from pressure modelling for coarse grid model. Note that water flows from high to low excess pressure regions, and its horizontal direction is sub-parallel to the structural dip. Flow rate anomalies correspond to sandstones.

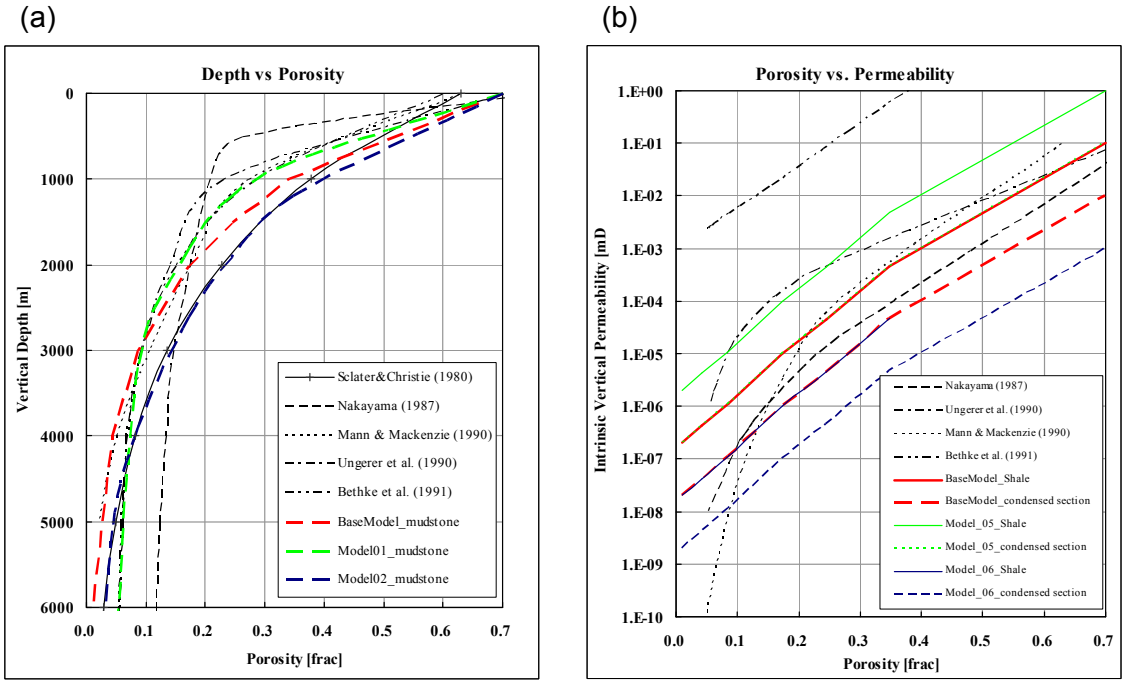

Figure 5.20 Depth vs. porosity (a) and porosity vs. permeability (b) relationships for mudstone, used for the calibration runs of pressure modelling. Also plotted are those from literatures.

Table 5.3 Input parameters for pressure modelling sensitivity runs.

BaseModel	Calibrated								
Mudstone					**Condensed section**				
Depth[m]	ϕ [frac]	k_h [mD]	k_v [mD]	P_{thma} [MPa]	Depth[m]	ϕ [frac]	k_h [mD]	k_v [mD]	P_{thma} [MPa]
0	0.700	2.00E+01	2.00E+00	1.07E-01	0	0.700	2.00E+00	2.00E-01	3.37E-01
1000	0.341	5.10E-03	5.10E-04	4.65E+00	1000	0.341	5.10E-04	5.10E-05	1.47E+01
1500	0.238	4.76E-04	4.76E-05	1.27E+01	1500	0.238	4.76E-05	4.76E-06	4.02E+01
2000	0.166	9.09E-05	9.09E-06	2.43E+01	2000	0.166	9.09E-06	9.09E-07	7.69E+01
3000	0.081	1.28E-05	1.28E-06	4.52E+01	3000	0.081	1.28E-06	1.28E-07	1.43E+02
4000	0.039	4.93E-06	4.93E-07	5.08E+01	4000	0.039	4.93E-07	4.93E-08	1.61E+02
6000	0.009	2.47E-06	2.47E-07	5.30E+01	6000	0.009	2.47E-07	2.47E-08	1.70E+02

Model_01	Compaction curve from Bethke *et al.* (1991)								
Mudstone					**Condensed section**				
Depth[m]	ϕ [frac]	k_h [mD]	k_v [mD]	P_{thma} [MPa]	Depth[m]	ϕ [frac]	k_h [mD]	k_v [mD]	P_{thma} [MPa]
0	0.700	2.00E+01	2.00E+00	1.07E-01	0	0.700	2.00E+00	2.00E-01	3.37E-01
800	0.341	5.10E-03	5.10E-04	4.65E+00	1000	0.341	5.10E-04	5.10E-05	1.47E+01
1200	0.238	4.76E-04	4.76E-05	1.27E+01	1500	0.238	4.76E-05	4.76E-06	4.02E+01
1800	0.166	9.09E-05	9.09E-06	2.43E+01	2000	0.166	9.09E-06	9.09E-07	7.69E+01
3200	0.081	1.28E-05	1.28E-06	4.52E+01	3000	0.081	1.28E-06	1.28E-07	1.43E+02
8000	0.039	4.93E-06	4.93E-07	5.08E+01	4000	0.039	4.93E-07	4.93E-08	1.61E+02
20000	0.009	2.47E-06	2.47E-07	5.30E+01	6000	0.009	2.47E-07	2.47E-08	1.70E+02

Model_02	Compaction curve from Sclater and Christie (1980)								
Mudstone					**Condensed section**				
Depth[m]	ϕ [frac]	k_h [mD]	k_v [mD]	P_{thma} [MPa]	Depth[m]	ϕ [frac]	k_h [mD]	k_v [mD]	P_{thma} [MPa]
0	0.700	2.00E+01	2.00E+00	1.07E-01	0	0.700	2.00E+00	2.00E-01	3.37E-01
1200	0.341	5.10E-03	5.10E-04	4.65E+00	1000	0.341	5.10E-04	5.10E-05	1.47E+01
1900	0.238	4.76E-04	4.76E-05	1.27E+01	1500	0.238	4.76E-05	4.76E-06	4.02E+01
2600	0.166	9.09E-05	9.09E-06	2.43E+01	2000	0.166	9.09E-06	9.09E-07	7.69E+01
3900	0.081	1.28E-05	1.28E-06	4.52E+01	3000	0.081	1.28E-06	1.28E-07	1.43E+02
5100	0.039	4.93E-06	4.93E-07	5.08E+01	4000	0.039	4.93E-07	4.93E-08	1.61E+02
8000	0.009	2.47E-06	2.47E-07	5.30E+01	6000	0.009	2.47E-07	2.47E-08	1.70E+02

Model_03	A order of higher permeability								
Mudstone					**Condensed section**				
Depth[m]	ϕ [frac]	k_h [mD]	k_v [mD]	P_{thma} [MPa]	Depth[m]	ϕ [frac]	k_h [mD]	k_v [mD]	P_{thma} [MPa]
0	0.700	2.00E+01	2.00E+00	1.07E-01	0	0.700	2.00E+00	2.00E-01	3.37E-01
1000	0.341	5.10E-03	5.10E-04	4.65E+00	1000	0.341	5.10E-04	5.10E-05	1.47E+01
1500	0.238	4.76E-04	4.76E-05	1.27E+01	1500	0.238	4.76E-05	4.76E-06	4.02E+01
2000	0.166	9.09E-05	9.09E-06	2.43E+01	2000	0.166	9.09E-06	9.09E-07	7.69E+01
3000	0.081	1.28E-05	1.28E-06	4.52E+01	3000	0.081	1.28E-06	1.28E-07	1.43E+02
4000	0.039	4.93E-06	4.93E-07	5.08E+01	4000	0.039	4.93E-07	4.93E-08	1.61E+02
6000	0.009	2.47E-06	2.47E-07	5.30E+01	6000	0.009	2.47E-07	2.47E-08	1.70E+02

Model_04	A order of lower permeability								
Mudstone					**Condensed section**				
Depth[m]	ϕ [frac]	k_h [mD]	k_v [mD]	P_{thma} [MPa]	Depth[m]	ϕ [frac]	k_h [mD]	k_v [mD]	P_{thma} [MPa]
0	0.700	2.00E+01	2.00E+00	1.07E-01	0	0.700	2.00E+00	2.00E-01	3.37E-01
1000	0.341	5.10E-03	5.10E-04	4.65E+00	1000	0.341	5.10E-04	5.10E-05	1.47E+01
1500	0.238	4.76E-04	4.76E-05	1.27E+01	1500	0.238	4.76E-05	4.76E-06	4.02E+01
2000	0.166	9.09E-05	9.09E-06	2.43E+01	2000	0.166	9.09E-06	9.09E-07	7.69E+01
3000	0.081	1.28E-05	1.28E-06	4.52E+01	3000	0.081	1.28E-06	1.28E-07	1.43E+02
4000	0.039	4.93E-06	4.93E-07	5.08E+01	4000	0.039	4.93E-07	4.93E-08	1.61E+02
6000	0.009	2.47E-06	2.47E-07	5.30E+01	6000	0.009	2.47E-07	2.47E-08	1.70E+02

Model_05	Same properties for condensed section as those for mudstone								
Mudstone					**Condensed section**				
Depth[m]	ϕ [frac]	k_h [mD]	k_v [mD]	P_{thma} [MPa]	Depth[m]	ϕ [frac]	k_h [mD]	k_v [mD]	P_{thma} [MPa]
0	0.700	2.00E+01	2.00E+00	1.07E-01	0	0.700	2.00E+00	2.00E-01	3.37E-01
1000	0.341	5.10E-03	5.10E-04	4.65E+00	1000	0.341	5.10E-04	5.10E-05	1.47E+01
1500	0.238	4.76E-04	4.76E-05	1.27E+01	1500	0.238	4.76E-05	4.76E-06	4.02E+01
2000	0.166	9.09E-05	9.09E-06	2.43E+01	2000	0.166	9.09E-06	9.09E-07	7.69E+01
3000	0.081	1.28E-05	1.28E-06	4.52E+01	3000	0.081	1.28E-06	1.28E-07	1.43E+02
4000	0.039	4.93E-06	4.93E-07	5.08E+01	4000	0.039	4.93E-07	4.93E-08	1.61E+02
6000	0.009	2.47E-06	2.47E-07	5.30E+01	6000	0.009	2.47E-07	2.47E-08	1.70E+02

Model_06	Same properties for mudstone as those for condensed section								
Mudstone					**Condensed section**				
Depth[m]	ϕ [frac]	k_h [mD]	k_v [mD]	P_{thma} [MPa]	Depth[m]	ϕ [frac]	k_h [mD]	k_v [mD]	P_{thma} [MPa]
0	0.700	2.00E+01	2.00E+00	1.07E-01	0	0.700	2.00E+00	2.00E-01	3.37E-01
1000	0.341	5.10E-03	5.10E-04	4.65E+00	1000	0.341	5.10E-04	5.10E-05	1.47E+01
1500	0.238	4.76E-04	4.76E-05	1.27E+01	1500	0.238	4.76E-05	4.76E-06	4.02E+01
2000	0.166	9.09E-05	9.09E-06	2.43E+01	2000	0.166	9.09E-06	9.09E-07	7.69E+01
3000	0.081	1.28E-05	1.28E-06	4.52E+01	3000	0.081	1.28E-06	1.28E-07	1.43E+02
4000	0.039	4.93E-06	4.93E-07	5.08E+01	4000	0.039	4.93E-07	4.93E-08	1.61E+02
6000	0.009	2.47E-06	2.47E-07	5.30E+01	6000	0.009	2.47E-07	2.47E-08	1.70E+02

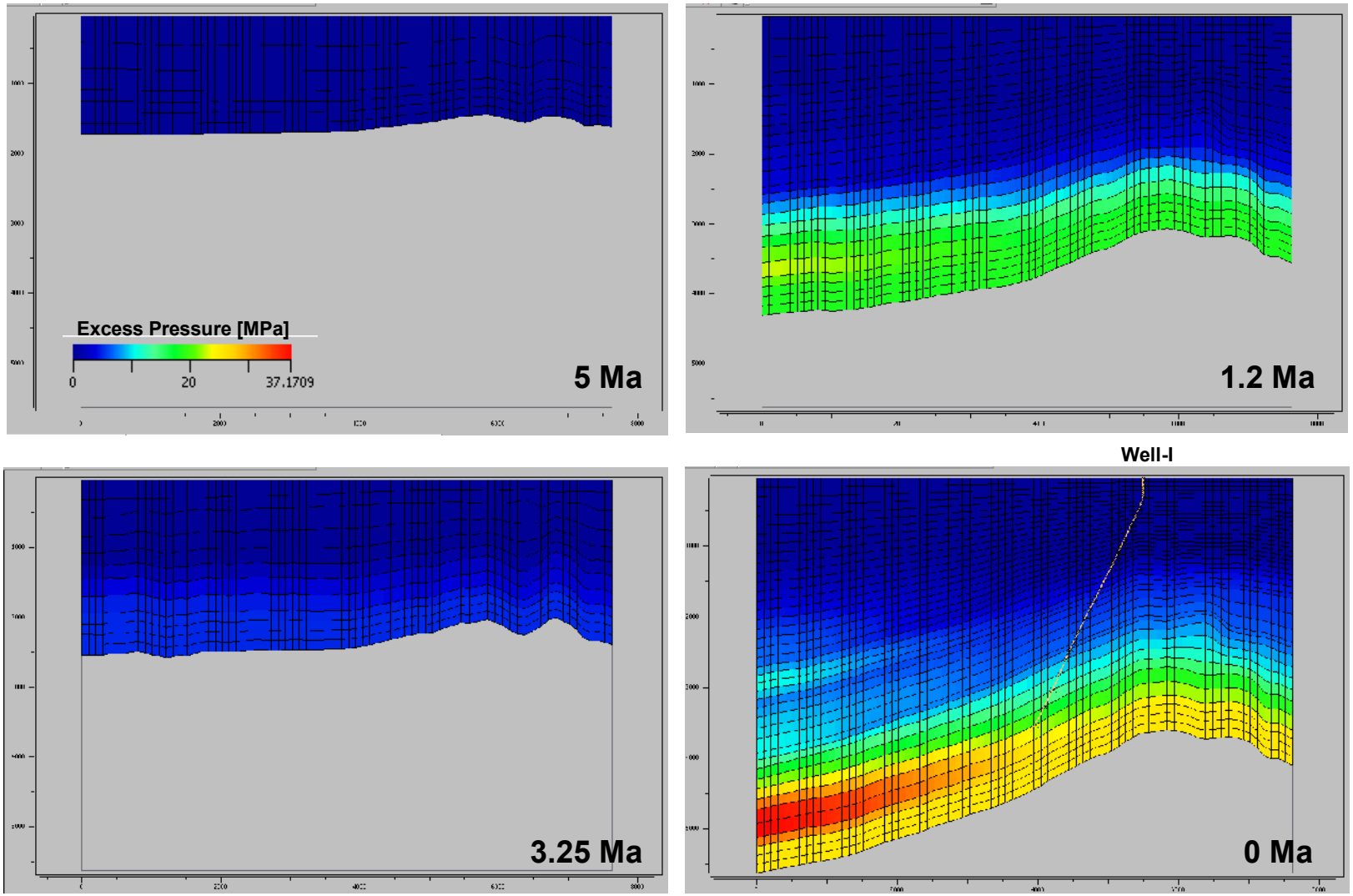

Figure 5.21 Results of 2D pressure modelling on NW-SE cross section showing overpressure development through time (Base Model)

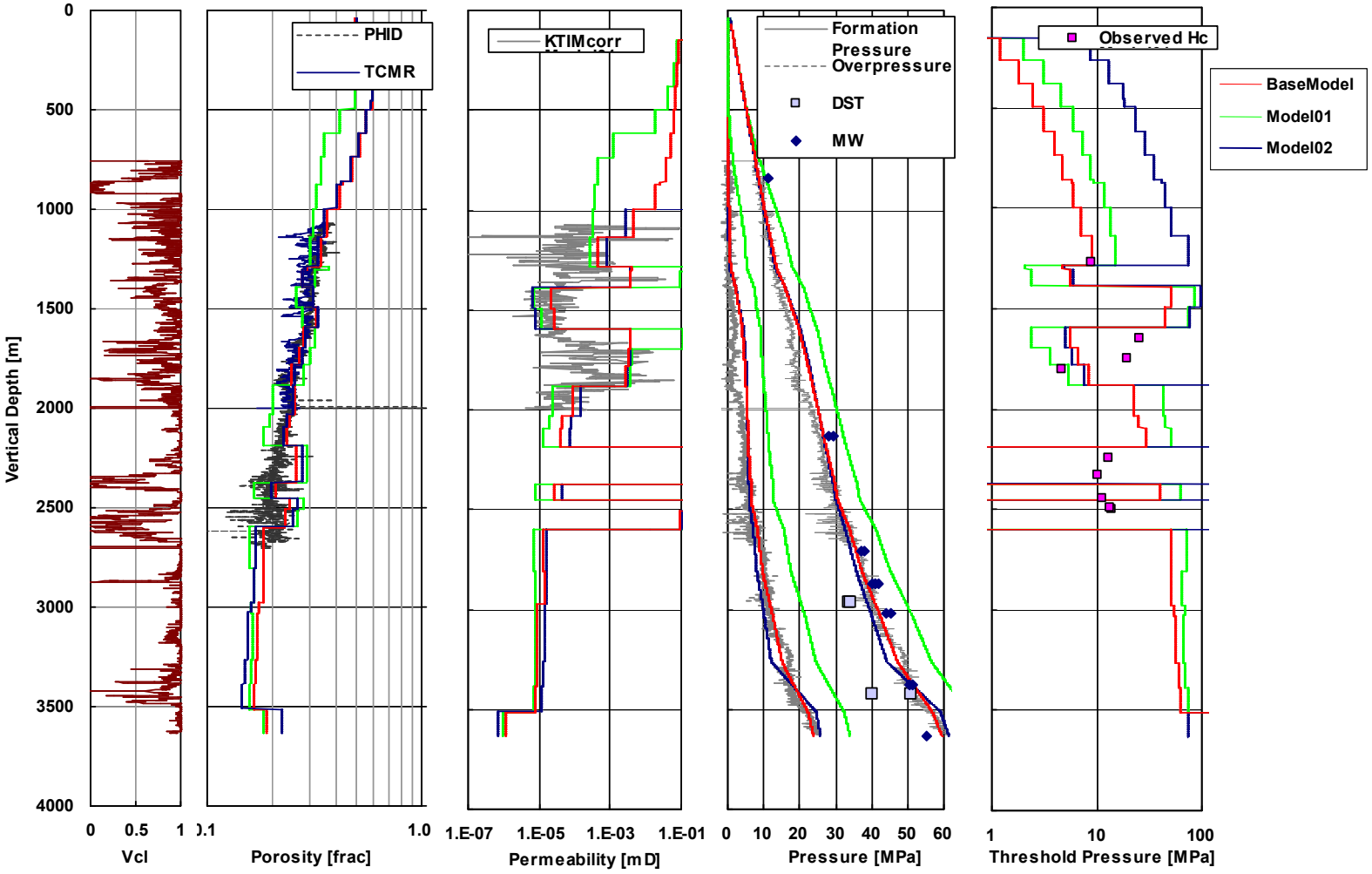

Figure 5.22 Permeability and threshold pressure optimization at well-I, showing sensitivity to compaction curves (Base Model vs. Model 01 and 02).

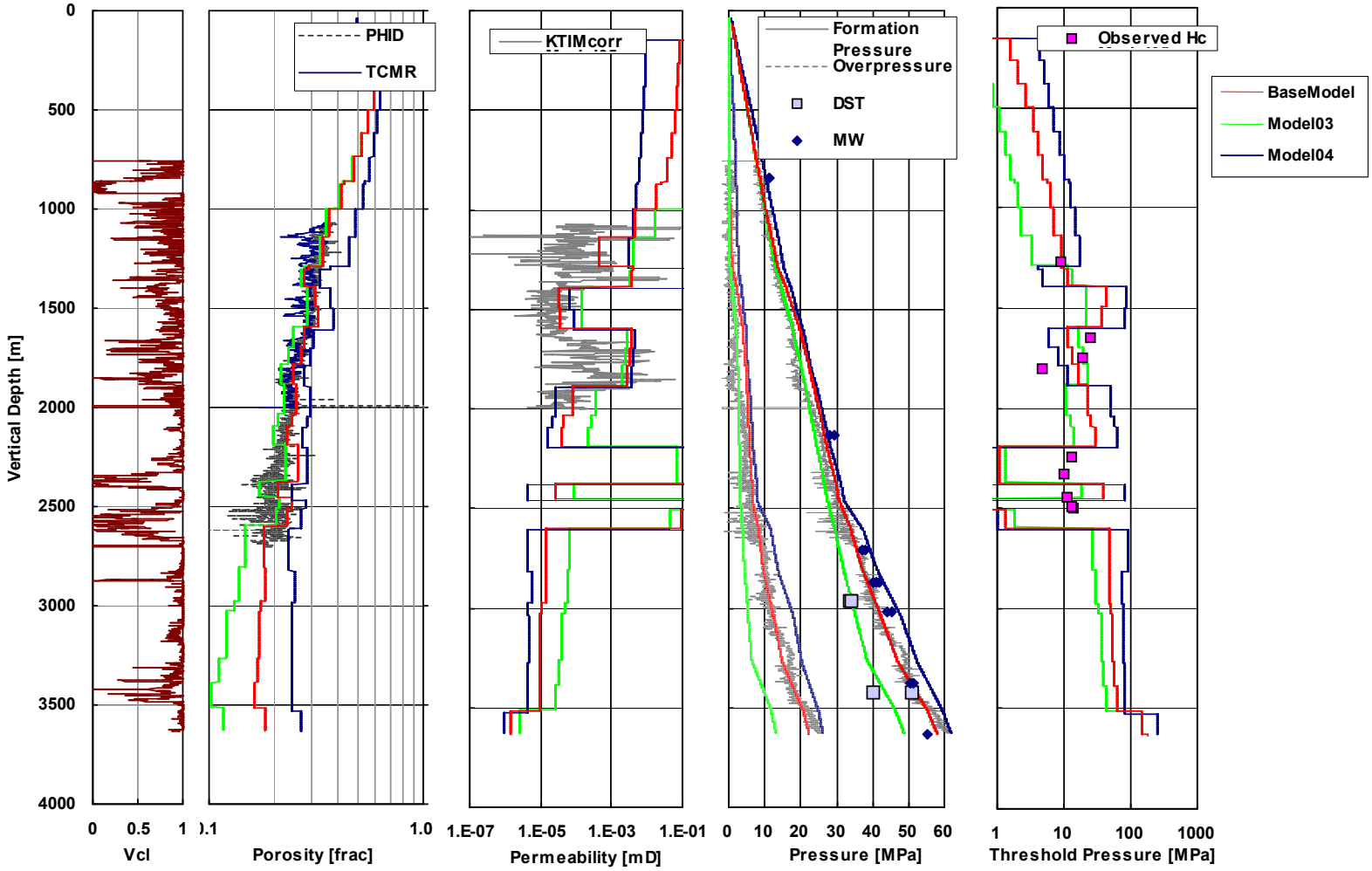

Figure 5.23 Permeability and threshold pressure optimization at well-I, showing sensitivity to ϕ-k relationship (BaseModel vs. Model 03 and 04).

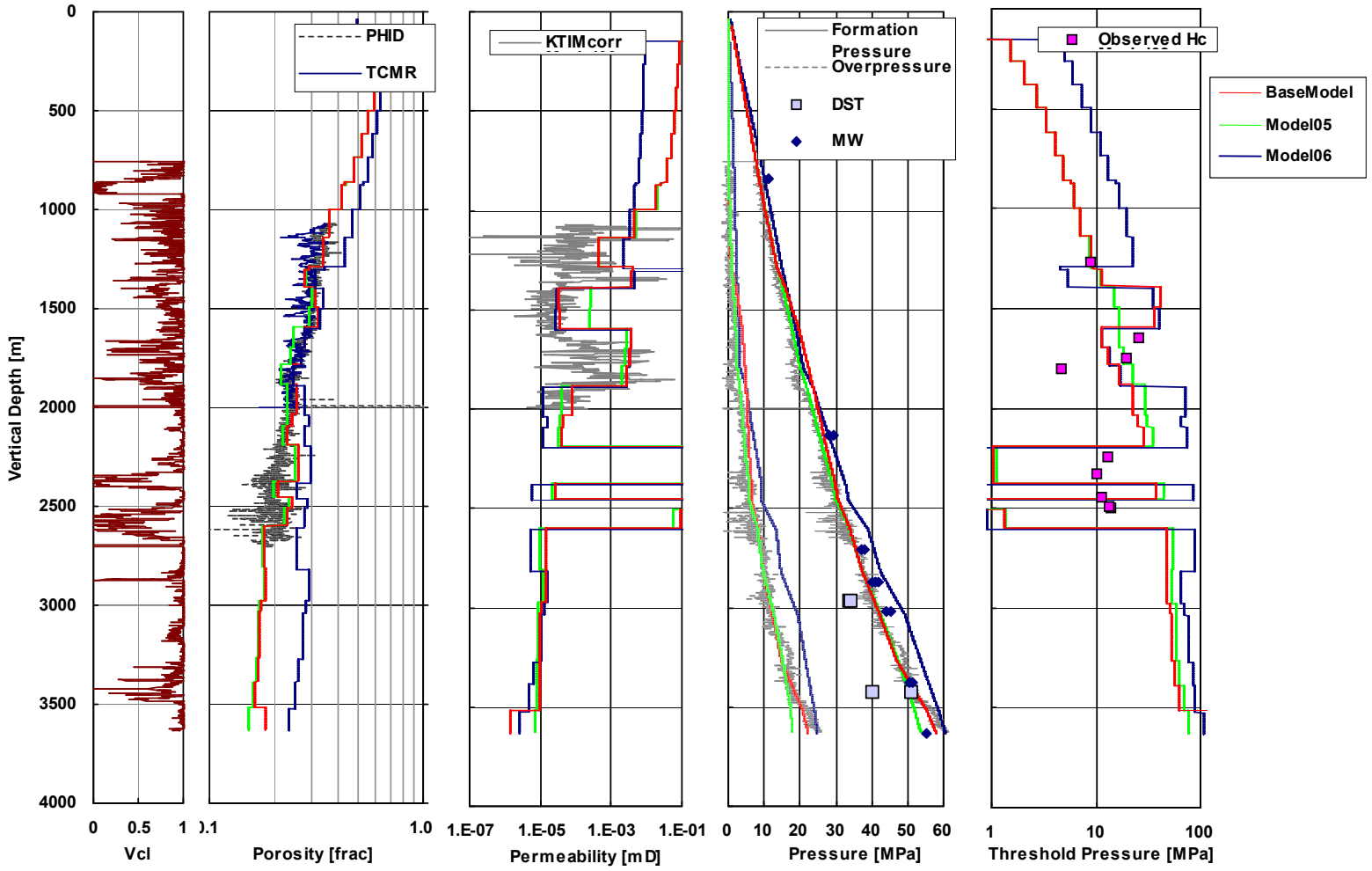

Figure 5.24 Permeability and threshold pressure optimization at well-I, showing sensitivity to incorporation of condensed section (Base Model vs. Model 05 and 06).

5.5 Petroleum migration modelling

5.5.1 Petroleum migration simulation using optimized P_{th}

In the previous section, parameters for petroleum migration modelling, permeability k and hence capillary threshold pressure P_{th} in particular, were optimized by pressure modelling. Now it is ready to conduct petroleum migration modelling using the optimized P_{th} distribution, *i.e.* that for "Base Model" in **Table 5.1**.

There are couple of assumptions and limitation of the migration modelling here. They are listed below, though some of those were already mentioned.

(1) Formation pressure was used only for calculating PVT (pressure, volume, temperature) and petroleum phase in the subsurface conditions, not for incorporating the hydrodynamic effects which deviate migration pathways and change sealing capacity of mudstones.

(2) Petroleum generation and expulsion are assumed only inside the model volume, though the actual kitchen area likely extends outside the volume.

(3) Generated petroleum was charged to the present-day structural volume only, not to the paleo-structures, simply to save the computation time. It is justified from the result of generation / expulsion modelling which demonstrates all the petroleum was generated and expelled in very recent time.

Petroleum migration was simulated by using the invasion percolation method. A commercial software MPath was used in the simulation works (see Section 2.5).

5.5.2 Results of petroleum migration simulation

Figures 5.25 shows petroleum migration pathways coloured by invasion sequence, *i.e.* cells are coloured according to the sequence in which they are charged with petroleum. Cells coloured in blue see the petroleum first, and those in red do in the late stages. The oil and gas expelled from the matured Nanatani and Teradomari Formations in the southwest migrate vertically to the Shiiya Formation, and once they reach carriers (sandstones) then move laterally in those carriers towards the structural high: the Iwafuneoki anticline. Since carriers are not continuous for the whole area, the oil and gas reach the pinch-out points to form accumulations. A number of accumulations are seen along the migration pathways, *i.e.* in the downdip side of the Iwafuneoki field (**Figures 5.26**).

The amount of the accumulation (column height) is controlled by the mudstone P_{th} at the pinch-out points, and when the buoyancy of the trapped oil and gas exceed the $P_{th,}$ they leak vertically to the carriers in shallower layers in the Shiiya and Nishiyama Formations. On the other hand, if P_{th} of the pinch-out points is higher than the maximum possible

buoyancy which the trap can accumulates, the excess amount of oil or gas spill from the point with the smallest $P_{th.}$ **Figures 5.27** shows which accumulations undergo leaking, spilling or still having room for additional accumulation. The figure indicates that most of the excess amount of petroleum migrated in the Nishiyama Formation is leaking from the traps, which is natural for stratigraphic traps (green accumulations in **Figures 5.27**). However a small number of traps make the excess amount of petroleum to spill out of them, through the connected sand bodies (orange accumulations). The figure also shows that the amount of the petroleum charge is sufficient to fill the traps in the migration pathways in this area, since there are no pools being filled with additional petroleum.

Type of pore fluid (oil or gas) also has a significant impact on determining migration pathways and final accumulations. It is because gas has a different density and interfacial tension than oil, which results in different buoyancy and $P_{th,}$ (equation 2.28). That is, the same seal rock has a smaller sealing capacity for gas from that for oil, in terms of column height. **Figure 5.28** shows that the simulation successfully reproduces different migration pathways between oil and gas. As a consequence, some accumulations are charged only with oil while others only with gas. The arrow in **Figure 5.28** is an example of phase segregation through migration. It can be explained by Gussow's principle of differential entrapment (Gussow, 1954). That is, the trap with rather small height is gas-prone, and the spilled oil from this trap migrates up to another shallower trap located to the north, to form an oil accumulation. The spill of oil is indicated by the orange colour for this trap in **Figures 5.27**.

5.5.3 Reproducibility of the Iwafuneoki pools

Reliability of the simulation is best demonstrated by examining the reproducibility of the known pools. **Figures 5.29** shows simulated oil and gas accumulations in the Iwafuneoki field. The figure indicates that distribution of most of the known pools is successfully reproduced with acceptable accuracy. That is, oil and gas are accumulated in the middle (N3 – N4 sequences) and lower (N1 – N2) Nishiyama Formation, only between the wells G and H, where the actual accumulations are proven.

However, there are some discrepancies between actual and simulated accumulations. Firstly, the upper Shiiya (S4) pools do not appear in the simulation. Secondly, fraction of accumulated petroleum phase in the Nishiyama Formation is rather different from the actual. That is, the N3 reservoir is filled with oil with cap gas in the simulation (**Figure 5.28**), but reality is a gas pool with no ring oil. On the contrary, N4 is a gas pool in the simulation, but it is actually oil-prone. The same is true for N1 – N2 oil pools, which in the simulation have a small amount of cap gas.

Those two problems are both attributed either to the inappropriate modelled sand distribution in the downdip of the field, or to the limited area of interest.

As shown above, the petroleum distribution and its phase are controlled by a combination of geometry of the sand bodies and P_{th} of the seals throughout the migration pathways from the kitchen to the traps. In particular, since the source rocks (Nanatani and Teradomari Formations) and reservoir rocks (Shiiya and Nishiyama Formations) are in different formations in this field, prediction of three dimensional sand distribution is necessary to properly simulate migration and entrapment. Slight difference in sand distribution in the downdip (*i.e.* carrier distribution in the upstream area) can completely change the migration pathway to the downstream traps and fluid phase in those traps. The discrepancies are therefore most probably because of the inappropriate sand distribution in the downdip area, which is poorly constrained.

Another possibility of the discrepancies is attributed to the limited area of interest. Since the area of interest does not cover the whole basin, the simulation does not account for the petroleum expelled in the more matured kitchen in the basin centre to the southwest where more petroleum must be generated and expelled (**Figure 5.1**). This must affect the amount of petroleum available to fill the traps in the modelled volume, and also the ratio of oil and gas. Furthermore, it results in the failure to incorporate the distribution of carriers outside the modelled volume.

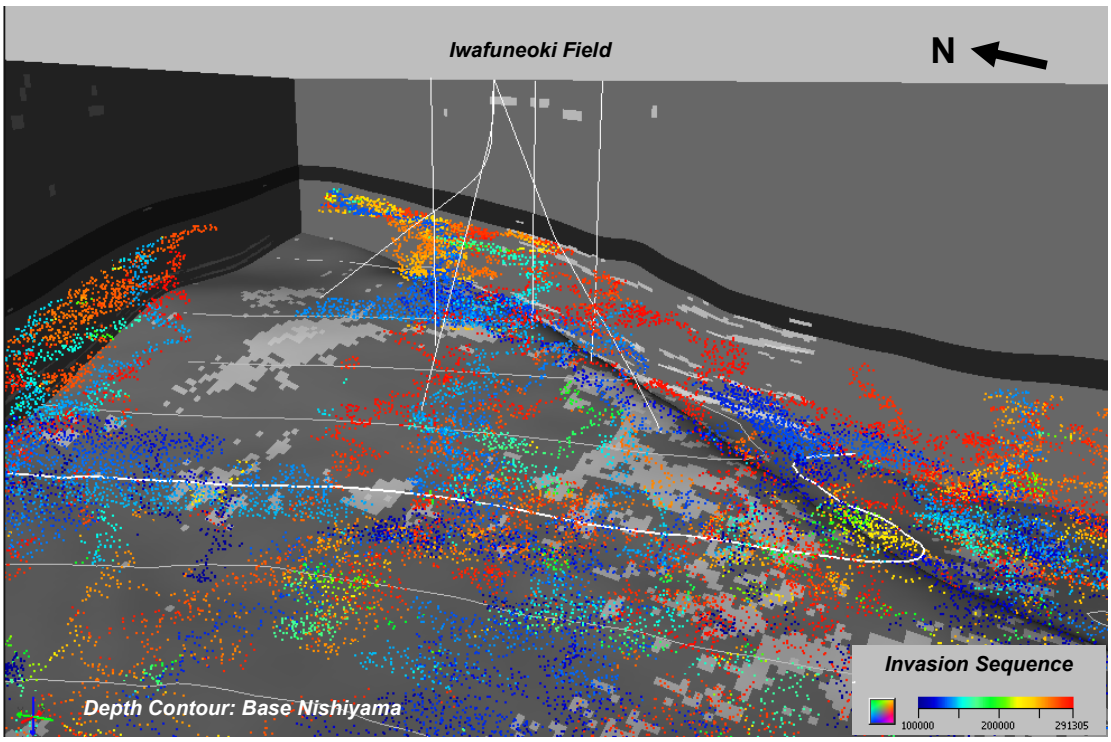

Figure 5.25 Simulated petroleum migration pathways in the Nishiyama Formation, at present-time. A number of migration paths towards the Iwafuneoki field are recognized.

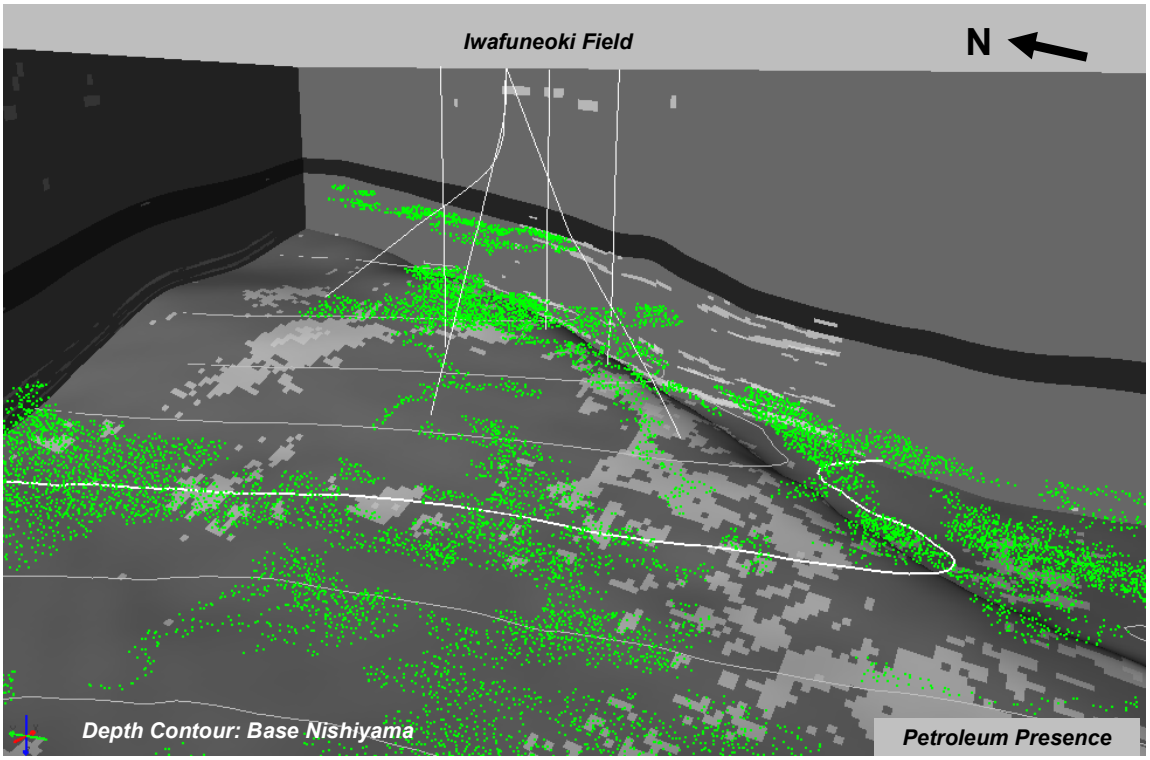

Figure 5.26 Simulated petroleum distribution in the Nishiyama Formation, at present-time. Note the accumulations along the migration paths.

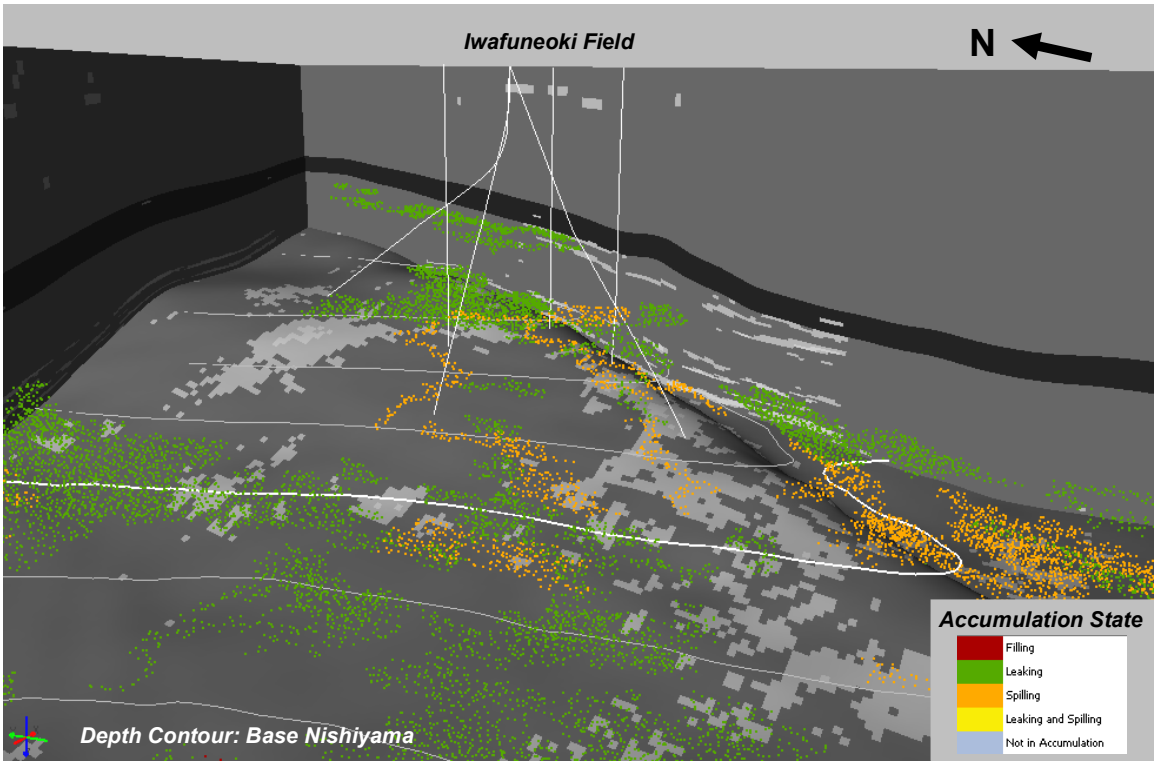

Figure 5.27 Simulated accumulation state of trapped petroleum in the Nishiyama Formation at present-time.

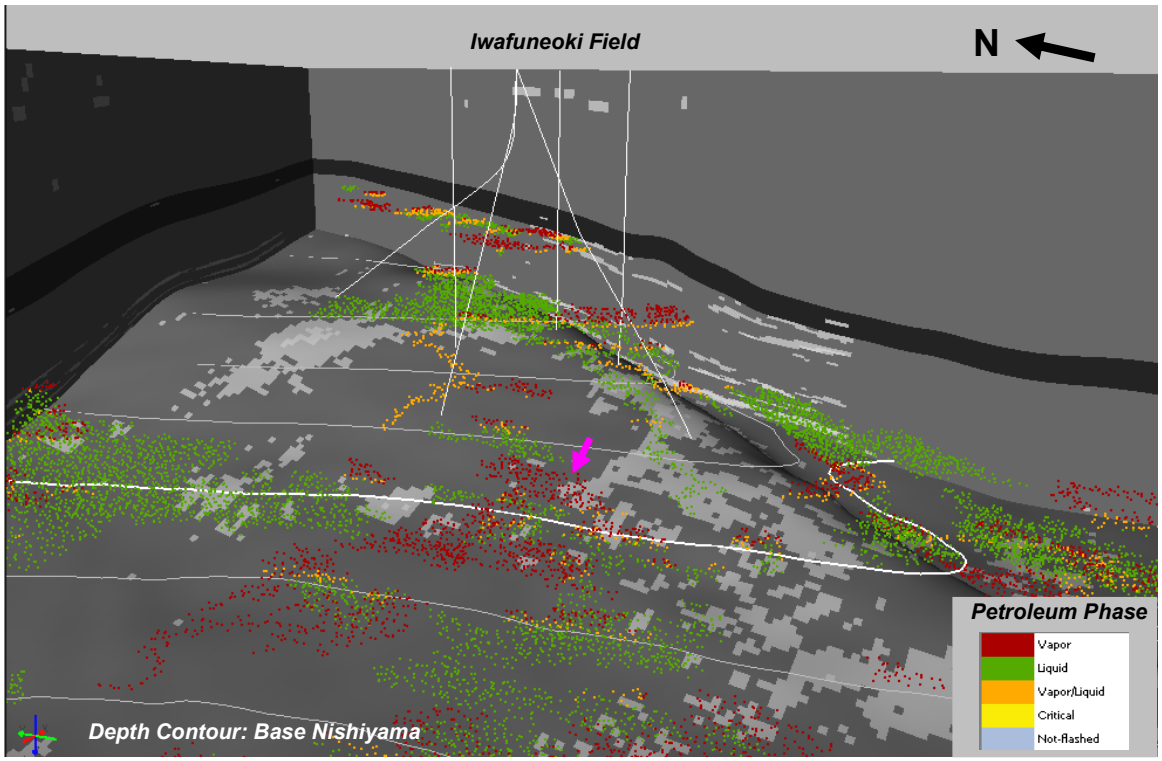

Figure 5.28 Simulated petroleum phase in accumulations in the Nishiyama Formation, at present-time. The gas accumulation shown in a pink arrow corresponds to a spilling trap (orange in Figure 5.27). See text for detail.

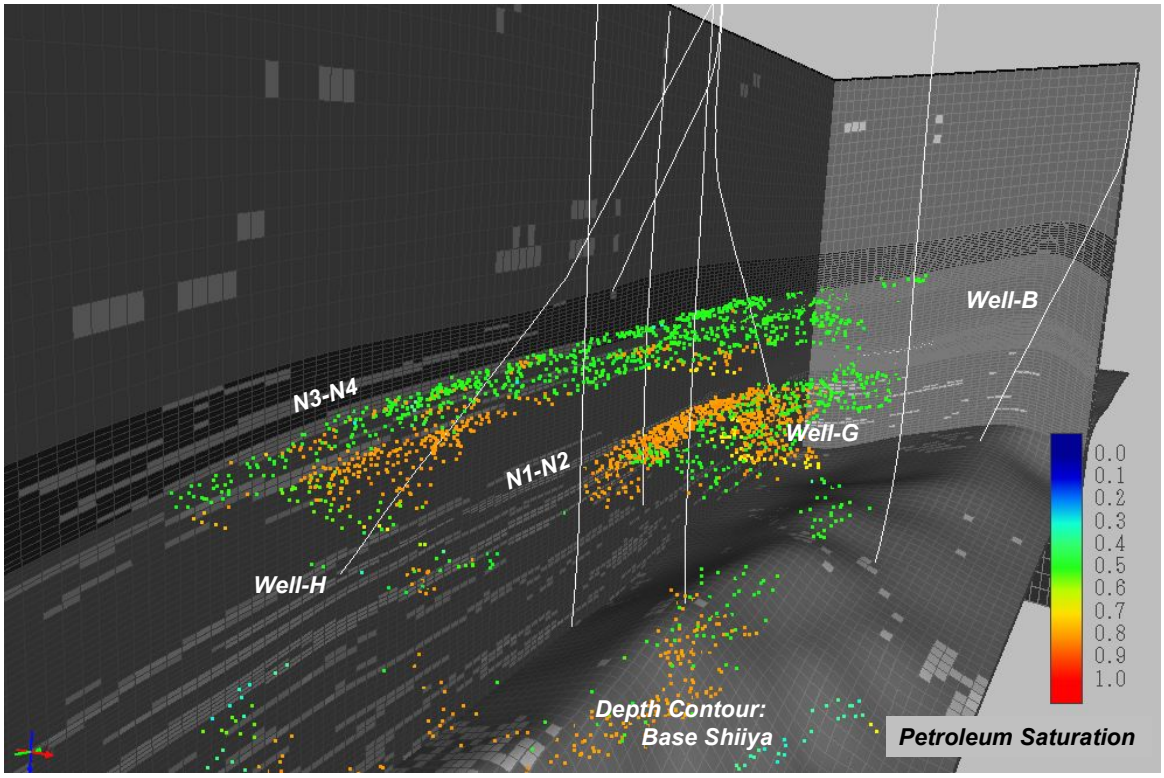

Figure 5.29 Simulated petroleum distribution in the Iwafuneoki field.

6 Petroleum migration modelling as a prediction tool

6.1 Optimizing migration modelling and insight into further exploration potential

Since the first petroleum migration modelling appeared in early 1980's, significant efforts have been continuing to make it really feasible tool for petroleum exploration. The most important recent achievement is obviously the capability of 3D models. Now we can simulate multi-phase petroleum migration and entrapment on very fine-grid, complex 3D models. However, the present state of the art is, in the author's view, at the level that the 3D implementation has just completed (*e.g.* Schneider and Wolf, 2000), and furthermore, many case studies reported in literatures are still in 2D (*e.g.* Naeth *et al.* 2005). It is undeniable that more research and application studies are necessary to obtain more plausible petroleum migration modelling results and use it as a prediction tool for practical petroleum exploration.

There must be two kinds of researches or studies to optimize the migration models as mentioned in Chapter 1; (1) re-examination of migration and entrapment mechanisms, and (2) parameter optimization. Throughout this thesis, the author tried to tackle with both of those from the viewpoint of abnormal formation pressure.

The effect of abnormal formation pressure on petroleum migration and entrapment is one of the disputed problems in petroleum migration mechanism, which the author addressed in this thesis. It was demonstrated that the abnormal formation pressure itself does not promote nor prevent the trapped petroleum to leak, based on the theoretical consideration of pressure profile in reservoirs and examination of field examples. This conclusion will give a positive evaluation for many abnormally pressured prospects, because it is often the case that overpressured reservoirs are overlain by less overpressured seals in the deeper part of sedimentary basins. As exploration gets matured, remaining prospects tend to be situated at deeper part of the basins, and thus there exist more chances for overpressured reservoirs to be encountered. They were often assessed to have high risk of petroleum leakage from the overpressured reservoirs. However, if the conclusion from this research is valid, overpressure itself is not the risk, as long as the pressure does not reach the hydrofracturing level.

Since many geological phenomena are mutually related with each other, it is extremely important to integrate all the data and knowledge to create realistic models. The research demonstrated that more refined or calibrated migration models can be created by properly incorporating abnormal formation pressure data via the k - P_{th} correlation. It is important to note, however, the error bar in the k - P_{th} correlation is rather large, because

it is a power-law relationship, *i.e.* estimated values can easily be different from the real ones by a couple of times. Moreover the correlation line can be fairly different from one field to another, so calibration for individual fields is necessary to obtain reliable estimations. Nevertheless, continuing improvement of the models by integrating all the data and knowledge is the right way to the better understanding of petroleum migration and entrapment, which will be used as a *real* prediction tool.

6.2 Areas for future researches

This research is far from perfect but many areas of further researches are still left to optimize petroleum migration and entrapment models. Three of those are listed below:

As pointed out through the thesis, capillary threshold pressure of mudstones and its 3D distribution are the most significant parameter to control petroleum migration and entrapment. Obviously more researches are needed to create more realistic P_{th} distribution models. Using seismic attributes, geostatistical methods and applying sequence stratigraphic concepts must be the main areas of researches. In the example of the Iwafuneoki field shown in Chapter 5, it was revealed that one of the condensed sections has higher sealing capacity than that of other mudstones and that it forms the upper limit of the thermogenic petroleum migration in this field. Prediction of 3D distribution of the condensed section by *e.g.* applying sequence stratigraphic concepts may be a great help to understand the petroleum system of this area.

One of the largest unknowns in petroleum migration is the petroleum flow rate in mudstones. In this research, capillary (buoyancy) pressure of petroleum is assumed to be in balance with capillary threshold pressure of the seal rocks. However, it is not clear if this equilibrium is always valid. Petroleum charge to traps occurs at a finite rate, while leakage of petroleum from traps also must take some time. If leakage rate is sufficiently high to drain all the excess amount of petroleum charged to a trap, capillary threshold pressure does determine the column height. On the contrary, if leakage rate is slower than charge rate, the trap might hold larger column height than calculated from the threshold pressure, forming a "dynamic trap" (Sylta, 2005). The latter case might happen in overpressured environments, because in those environments at least retard of water flow occurs in low permeability mudstones. It implies that the leakage of petroleum through those mudstones is also extremely slow. Understanding the mechanism of petroleum migration in mudstones might lead an additional potential of "dynamic traps".

Another exciting research area is an integration of petroleum migration modelling, reservoir engineering and reservoir geochemistry (*e.g.* Cubitt *et al.* 2004). Fluid flow behaviour at production time scale provides with detailed information about the reservoir

heterogeneity or connectivity, which is normally difficult to obtain from the fluid flow behaviour at geological time scale. On the other hand, geochemical data including petroleum maturity, chemical composition, carbon isotope, etc. have recently revealed very complex fluid distribution even in reservoirs in pressure communication, as reported from various fields. It reflects complex migration history and indicates that the fluid mixing is on-going process. Integrating all those data from different disciplines and building the models to satisfy all of those is indeed challenging work, but necessary to make petroleum migration modelling really feasible.

7 Conclusions

The conclusions of this research are as follows:

(1) Abnormal formation pressure in reservoirs does not have a direct influence on petroleum migration and entrapment, *i.e.* it does not promote nor prevent the trapped petroleum to leak.

(2) There are close mutual relationships between abnormal pressure and permeability, and between permeability and capillary threshold pressure. Therefore the abnormal pressure can be used to predict capillary threshold pressure of seal rocks and to optimize petroleum migration and entrapment models.

(3) Validity and applicability of the above model are examined by the case study in the Iwafuneoki field, Japan. It successfully reproduced both pressure and petroleum distribution in the field with acceptable accuracy.

(4) The findings on the role of abnormal formation pressure have a potential impact on prospect evaluation for petroleum exploration. It can cast a new light on undiscovered or overlooked prospects in overpressured fields.

(5) Continuing improvements of the models by integrating all the data and knowledge are necessary to better understanding of petroleum migration and entrapment. Those challenges will lead the migration modelling to a *real* prediction tool.

References

Allen, D., Flaum, C., Ramakrishnan, T. S., Bedford, J., Castelijns, K., Fairhurst, D., Gubelin, G., Heaton, N., Minh, C.C., Norville, M.A., Seim, M.R., Pritchard, T. and Ramamoorthy, R., 2000, Trends in NMR Logging. *Oilfield Review*, **12**, 2, 2-19.

Amyx, J.W., Bass, D.M. and Whiting, R., 1960, *Petroleum Reservoir Engineering, Physical Properties*. McGraw-Hill, 610p.

Aplin, A.C., Fleet, A.J. and Macquaker, J.H.S. (eds) 1999, *Muds and Mudstones: Physical and Fluid Flow Properties*. Geological Society, London, Special Publication, **158**, 190p.

Aplin, A.C. and Larter, S.R., 2005, Fluid flow, pore pressure, wettability, and leakage in mudstone ca rocks. *In*: Boult, P. and Kaldi, J. (eds) *Evaluating Fault and Cap Rock Seals*. AAPG Hedberg Series, **2**, 1-12.

Begg, S. H. and King, P. R., 1985, Modeling the effects of shales on reservoir performance: calculation of effective vertical permeability. SPE13529.

Berg, R.R., 1975, Capillary pressures in stratigraphic traps. *AAPG Bulletin*, **59**, 939–956.

Berg, R.R., Avery, A.H., 1995, Sealing properties of Tertiary growth faults, Texas Gulf Coast. *AAPG Bulletin* **79**, 375-393.

Bethke, C.M., Reed, J.D. and Oltz, D.F., 1991, Long range petroleum migration in the Illinois basin. *AAPG Bulletin*, **75**, 925-945.

Bjorkum, P. A., Walderhaug, O. & Nadeau, P., 1998, Physical constraints on hydrocarbon leakage and trapping revisited. *Petroleum Geoscience*, **4**, 237-239.

Brace, W.F., 1980, Permeability of crystalline and argillaceous rocks. *International Journal of Rock Mechanics & Mining Sciences*, **17**, 241-251.

Bradley, J. S., 1975, Abnormal formation pressure. *AAPG Bulletin*, **59**, 957-973.

Bradley, J. S. and Powley, D. E., 1994, Pressure compartments in sedimentary basins: a review. *In* Ortoleva, P. J. (ed), *Basin compartments and seals*. AAPG Memoir **61**, 3-26.

Bredehoeft, J.D., Wesley, J.B., Fouch, T.D., 1994, Simulations of the origin of fluid pressure, fracture generation, and the movement of fluids in the Uinta Basin, Utah. *AAPG Bulletin*, **78**, 1729-1747.

Carman, P.C., 1956, *The Flow of Gases through Porous Media*. Academic Press, New York.

Carruthers, D., 1998, Transport modelling of secondary oil migration using gradient-driven invasion percolation techniques. phD thesis, Department of Petroleum Engineering, Heriot-Watt University, 210p.

Carslaw, H.S. and Jaeger, J.C., 1959, *Conduction of Heat in Solids.* Oxford University Press, 510p.

Catalan, L., Xiaowen, F., Chatzis, I. and Dullien, F.A., 1992, An experimental study of

secondary oil migration. *AAPG Bulletin*, **76**, 638-650.

Childs, C., Manzocchi, T., Nell, P., Walsh, J.J., Strand, J., Heath, A.E. and Lygren, T.H., 2002a, Geological implications of a large pressure difference across a small fault in the Viking Graben. *In*: Koestler, A.G. and Hunsdale, R. (eds), *Hydrocarbon Seal Quantification.* NPF Special Publication **11**, 187-201.

Childs, C., Sylta, Ø., Moriya, S., Hermansen, D., Strand, J.A. and Walsh, J.J., 2002b, The impact of fault seal properties on hydrocarbon migration modelling of the Oseberg-Syd area, Viking Graben. *AAPG Hedberg Conference*. Barossa Valley, Australia. 75-78.

Childs, C., Sylta, Ø., Moriya, S., Walsh, J.J. and Manzocchi, T., 2002c, A method for including the capillary properties of faults in hydrocarbon migration models. *In*: Koestler, A.G. and Hunsdale, R. (eds), *Hydrocarbon Seal Quantification.* NPF Special Publication **11**, 127-139.

Childs, C., Sylta, Ø., Moriya, S., Morewood, N., Manzocchi, T. and Walsh, J.J., in press, Calibrating fault seal using a hydrocarbon migration model of the Oseberg-Syd area, Viking Graben. *Marine and Petroleum Geology*.

Christie, M.A. and Blunt, M.J., 2001, Tenth SPE Comparative Solution Project: A Comparison of Upscaling Techniques. *SPE Reservoir Evaluation & Engineering*, **4**, 308-317.

Clayton, C.J. / Bjorkum, P. A., Walderhaug, O. & Nadeau, P., 1999, Discussion: 'Physical constraints on hydrocarbon leakage and trapping revisited' by Bjorkum, P. A. *et al*. *Petroleum Geoscience*, **5**, 99-101.

Clayton, C.J. and Hay, S.J., 1994, Gas migration mechanisms from accumulation to surface. *Bulletin of Geological Society of Denmark*, **41**, 12-23.

Core Laboratories, Inc., 1982, A course in special core analysis.

Corbet, T.F. and Bethke, C.M., 1992, Disequilibrium fluid pressures and groundwater flow in the Western Canada sedimentary basin. *Journal of Geophysical Research*, **97**, B5, 7203-7217.

Corcoran, D.V. and Dore, A.G., 2002, Top seal assessment in exhumed basin settings – some insights from Atlantic Margin and borderland basins. *In*: Koestler, A.G. & Hunsdale, R. (eds), *Hydrocarbon Seal Quantification.* NPF Special Publication **11**, 89-107.

Cubitt, J. M., England, W. A. and Larter, S. R. (eds), 2004, Understanding Petroleum Reservoirs: Towards an Integrated Reservoir Engineering and Geochemical Approach. *Geological Society Special Publication*, **237**

Deming, D., 1994, Facors neccesary to define a pressure seal. *AAPG Bulletin*, **78** 1005-1009.

Deutsch, C.V. and Journel, A.G., 1998, *GSLIB: Geostatistical Software Library and User's*

Guide. Oxford University Press, 369p.

Dewhurst, D.N., Yang, Y., Aplin, A.C., 1999, Permeability and fluid flow in natural mudstones. *In*: Aplin, A.C., Fleet, A.J. and Macquaker, J.H.S. (eds) *Muds and Mudstones: Physical and Fluid Flow Properties*, Geological Society London Special Publication, **158**, 23-43.

Eaton, B.A., 1975, The equation for geopressure prediction from well logs. SPE5544.

England, W.A., Mackenzie, A.S., Mann, D.M and Quigley. T.M., 1987, The movement and entrapment of petroleum fluids in the subsurface. *Journal of the Geological Society London*, **144**, 327-347.

Fristad, T., Groth, A., Yielding, G. and Freeman, B., 1997, Quantitative fault seal prediction: a case study from Oseberg Syd. *In*: Moller-Pedersen, P. and Koestler, A.G. (eds) *Hydrocarbon Seals: Importance for Exploration and Production*. NPF Special Publication, **7**, 107-124.

Grauls, D., Pascaud, F. and Rives, T., 2002, Quantitative fault seal assessment in hydrocarbon-compartmentalised structures using fluid pressure data. *In*: Koestler, A.G. & Hunsdale, R. (eds), *Hydrocarbon Seal Quantification.* NPF Special Publication **11**, 141-156.

Gussow, W. C., 1954, Differential entrapment of oil and gas: a fundamental principle. *AAPG Bulletin*, **38**, 816-853.

He, Zhiyong and Corrigan, J., 1995, Factors Necessary to Defne a Pressure Seal: discussion. *AAPG Bulletin*, **79**, 1075-1078.

Hermanrud, C., 1993, Basin modelling techniques – an overview. *In*: Dore, A.G., Augustson, Hermanrud, C., Stewart, D.J. and Sylta, Ø. (eds), *Basin Modelling: Advances and Applications*. NPF Special Publication **3**, 1-34.

Hesthammer, J., Landro, M. and Fossen, H., 2001, Use and abuse of seismic data in reservoir characterisation. *Marine and Petroleum Geology,* **18**, 635-655.

Heum, O. R., 1996, A fluid dynamic classification of hydrocarbon entrapment. *Petroleum Geoscience*, **2**, 145-158.

Hildenbrand, A., Schlomer, S., Krooss, B.M., 2002, Gas breakthrough experiments on fine-grained sedimentary rocks. *Geofluids*, **2**, 3-23.

Hindle, A.D., 1997, Petroleum migration pathways and charge concentration: a three-dimensional model. *AAPG Bulletin*, **81**, 1451-1481.

Hubbert, M.K., 1953, Entrapment of petroleum under hydrodynamic conditions. *AAPG Bulletin*, **37**, 1954-2026.

Hunt, J.M., 1990, Generation and migration of petroleum from abnormally pressured fluid compartments. *AAPG Bulletin*, **74**, 1-12.

Hunt, J.M., 1995, *Petroleum Geochemistry and Geology*. W.H. Freeman and Company,

743p.

Ibrahim, M.A., Tek, M.R., and Katz, D.L., 1970, *Threshold pressure in gas storage*. American Gas Association, Arlington, VA, 309p.

Ingebritsen, S.E., Sanford, W.E. and Neuzil, C.E., 2006, *Groundwater in geologic processes*, Second edition. Cambridge University Press, 536p.

Ingram, G. M., Urai, J. L. and Naylor, M. A., 1997, Sealing processes and top seal assessment. *In*: Moller-Pedersen, P. and Koestler, A.G. (eds) *Hydrocarbon Seals: Importance for Exploration and Production*. NPF Special Publication, **7**, 165-174.

Jackson, M. D., Yoshida, S., Muggeridge, A. H. & Johnson, H.D., 2005, Three-dimensional reservoir characterization and flow simulation of heterolithic tidal sandstones. *AAPG Bulletin*, **89**, 507-528.

Jiao, Z.S. and Surdam, R.C., 1994, Stratigraphic / diagenetic pressure seals in the muddy sandstone, Powder River Basin, Wyoming. *In*: Ortoleva, P.J. (ed.) *Basin Compartments and Seals*. AAPG Memoir, **61**, 297-312.

Karlsson, W., 1986, The Snorre, Statfjord and Gullfaks oilfields and the habitat of hydrocarbons on the Tampen Spur, offshore Norway. *In:* Spencer, A.M., Campbell, C.J., Hanslien, S.H., Holter, E., Nelson, P.H.H., Nysæther, E. and Ormaasen, E.G. (eds.) *Habitat of Hydrocarbons of the Norwegian Continental Shelf*. Norwegian Petroleum Society, Graham and Trotman, London, 181-197.

Kenyon, W. E., 1997, Petrophysical principles of applications of NMR logging. *The Log Analyst*, **38**, 21-43.

Krushin, J.T., 1997, Seal capacity of nonsmectite shale. *In*: Surdam, R.C. (ed.), *Seals, traps, and the petroleum system*. AAPG Memoir, **67**, 31-47.

Lash, G.G., 2006, Top seal development in the shale-dominated Upper Devonian Catskill Delta Complex, western New York State. *Marine and Petroleum Geology* **23**, 317–335.

Law, B.E. and Spencer, C.W., 1998, Abnormal pressures in hydrocarbon environments. *In*: Law, B.E., Ulmishek, G.F. and Slavin, V.I. (eds), *Abnormal pressures in hydrocarbon environments*. AAPG Memoir **70**, 1-11.

Law, J., 1944, A statistical approach to the interstitial heterogeneity of sand reservoirs. *AIME Petroleum Trans*, **155**, 202-222.

Lee, Y. and Deming, D., 2002, Overpressures in the Anadarko basin, southwestern Oklahoma: static or dynamic? *AAPG Bulletin*, **86**, 145-160.

Leverett, M.C., 1941, Capillary behavior in porous solids. *AIME Petroleum Trans*, **142**, 152-169.

Lenormand, R., Touboul, E. and Zarcone, C. 1988, Numerical models and experiments on immiscible displacements in porous media. *Journal of Fluid Mechanics*, **189**, 165-187.

Lothe, A.E., Sylta, Ø., Lauvrak, O., Sperrevik, S., 2006, Influence of fault map resolution

on pore pressure distribution and secondary hydrocarbon migration; Tune area, North Sea. *Geofluids*, **6**, 122-136.

Lucia, F. J., 1999, *Carbonate Reservoir Characterization*. Springer-Verlag, Berlin, 226p.

Magoon, L. B. and Dow, W. G. (eds.), 1994, The petroleum system – from source to trap. *AAPG Memoir*, **60**, 655p.

Mann, D.M. and Mackenzie, A.S., 1990, Prediction of pore fluid pressures in sedimentary basins. *Marine and Petroleum Geology*, **7**, 55-65.

Mavko, G., Mukrrji, T. and Dvorkin, J., 1998, *The Rock Physics Handbook*. Cambridge University Press, 329p.

Miyazaki, H., Kude, T., Akiba, F., Fukasawa, H. and Asano, K., 1987, Geology of Iwafune-oki oil field – a preliminary study of the distribution of the sandstone reservoirs –. *Journal of the Japanese Association for Petroleum Technology,* **52**, 173-187 (in Japanese with English abstract).

Miwa, M., Watanabe, M., Yamada, K. and Yanagisawa, Y., 2004, Planktonic foraminiferal assemblages from the Pliocene Yabuta Formation, Nadaura, Himi City, Toyama Prefecture, with special reference to the base of the No.3 *Globorotalia inflata* bed. *Journal of the Japanese Association for Petroleum Technology,* **69**, 668-678 (in Japanese with English abstract).

Moriya, Shigehiro., 1995, High resolution correlation of the Neogene Nishiyama and Haizume Stages based on the foraminiferal fauna in the Kita-Kanbara Basin, Niigata Prefecture, Japan: basic data for sequence stratigraphy. JAPEX Research Report, **11**, 55-67.

Moriya, S., Yamane, T., Saito, Y., Kato, S. and Nakayama, K., 2007, Hydrocarbon migration modeling through turbidite sands in the Iwafuneoki field, offshore Japan. *Journal of the Japanese Association for Petroleum Technology,* **72**, 89-97 (in Japanese with English abstract).

Naeth, J., di Primio, R., Horsfield, B., Schaefer, R.G., Shannon, P.M., Bailey, W.R., Henriet, J.P., 2005, Hydrocarbon seepage and carbonate mound formation: A basin modelling study from the Porcupine Basin (offshore Ireland). *Journal of Petroleum Geology*, **28**, 147-166.

Nakayama, K., 1981, A simulation model for petroleum exploration - theoretical aspects and applications to the East Niigata field. *Journal of the Japanese Association for Petroleum Technology,* **46**, 221-236 (in Japanese with English abstract).

Nakayama, K., 1987, Two dimensional basin analysis for petroleum exploration. PhD Thesis, Department of Geology, University of South Carolina, 225p.

Nakayama, K. and Sato, D., 2002, Prediction of sealing capacityby the equivalent grain size method. *In*: Koestler, A. G. & Hunsdale, R. (eds), *Hydrocarbon Seal Quantification*.

NPF Special Publication **11**, 51-60.

Nakayama, K. and van Siclen, D.C., 1981, Simulation model for petroleum exploration. *AAPG Bulletin*, **65**, 1230-1255.

Neuzil, C.E., 1986, Groundwater flow in low-permeability environments. *Water Resources Research,* **22**, 1163-1195

Neuzil, C.E., 1994, How permeable are clays and shales? *Water Resource Research*, **30**, 145-150.

Neuzil, C.E., 1995, Abnormal pressures as hydrodynamic phenomena. *American Journal of Science*, **295**, 742-786.

Niigata Prefecture Geological Map Revision Committee, 2000, Geological map of Niigata Prefecture (2000 version). Niigata Prefectural Government, Japan (in Japanese).

Nordgard Bolas, H.M., Hermanrud, C. and Teige, G.M.G., 2005, Seal capacity estimation from subsurface pore pressures. *Basin Research*, **17**, 583-599.

Norwegian Petroleum Directorate, 1995, Structural elements of the Norwegian continental shelf, part II the Norwegian Sea region, *NPD Bulletin*, **8**, 45p.

Norwegian Petroleum Directorate, 2008, http://www.npd.no/English/Frontpage.htm.

Olstad, R., Bjorlykke, K. and Karlsen, D.A., 1997, Pore water flow and petroleum migration in the Smorbukk field area, offshore mid-Norway. *In*: Moller-Pedersen, P. and Koestler, A.G. (eds) *Hydrocarbon Seals: Importance for Exploration and Production*. NPF Special Publication, **7**, 201-217.

Osborne, M. J. and Swarbrick, R. E., 1997, Mechanisms for generating overpressure in sedimentary basins: a reevaluation. *AAPG Bulletin*, **81**, 1023-1041.

Pittman, E.D., 1992, Relationships of porosity and permeability to various parameters derived from mercry injection-capillary pressure curves for sandstone. *AAPG Bulletin*, **76**, 191-198.

Purcell, W.R., 1949, Capillary pressures-their measurement using mercury and the calculation of permeability therefrom. *Trans. AIME*, **186**, 39-48

Rodgers, S. / Bjorkum, P. A., Walderhaug, O. & Nadeau, P., 1999, Discussion: 'Physical constraints on hydrocarbon leakage and trapping revisited' by Bjorkum, P. A. *et al.* – further aspects. *Petroleum Geoscience*, **5**, 421-423.

Saito, Y., Yamamoto, T., Yamane, T., Moriya, S., Nishimura, M. and Takano, O., 2008, Exploration case study of sandstone pinch-out stratigraphic traps offshore Kitakanbara - challenge to discovery of "the second Iwafuneoki oil and gas field"-. *Journal of the Japanese Association for Petroleum Technology*, **73**, 38-46 (in Japanese with English abstract).

Sanchez-Vila, X., Carrera, J., Girardi, J.P., 1996, Scale effects in transmissivity. *Journal of Hydrology,* **183**, 1-22.

Sawamura, F. and Nakayama, K., 2005, Estimating the amount of oil and gas accumulation from top seal and trap geometry. *In*: Sorkhabi, R. and Tsuji, Y. (eds) *Faults, fluid flow and petroleum traps*. AAPG Memoir **85**, 33-42.

Schlomer, S. and Krooss, B.M., 1997, Experimental characterisation of the hydrocarbon sealing efficiency of cap rocks. *Marine and Petroleum Geology*, **14**, 565-580.

Schowalter, T.T., 1979, Mechanics of secondary hydrocarbon migration and entrapment. *AAPG Bulletin*, **63**, 723-760.

Sclater, J.G. and Christie, P.A.F., 1980, Continental stretching: an explanation of the post-Mid-Cretaceous subsidence of the Central North Sea basin. *Journal of Geophysical Research*, **85**, 3711-3739.

Schneider, F. and Wolf, S., 2000, Quantitative HC potential evaluation using 3D basin modelling: Application to Franklin structure, Central Graben, North Sea, UK. *Marine and Petroleum Geology*, **17**, 841-856.

Sneider, R.M, Sneider, J.S, Bolger, G.W. & Neasham, J.W., 1997, Comparison of seal capacity determinations: conventional cores vs. cuttings. *In*: Surdam, R.C. (ed.), *Seals, Traps, and the Petroleum System*. AAPG Memoir, **67**, 1-12.

Sperrevik, S., Gillespie, P.A., Fisher, Q.J., Halvorsen, T. and Knipe, R.J., 2002, Empirical estimation of fault rock properties. *In*: Koestler, A.G. & Hunsdale, R. (eds), *Hydrocarbon Seal Quantification*. NPF Special Publication **11**, 109-125.

Surdam, R.C., Jiao, Z.S. and Heasler, H.P. 1997, Anomalously pressured gas compartments in cretaceous rocks of the laramide basins of wyoming: a new class of hydrocarbon accumulation. *In*: Surdam, R.C. (ed.), *Seals, Traps, and the Petroleum System*. AAPG Memoir, **67**, 199-222

Swarbrick, R. E., Osborne, M. J., Grunberger, D., Yardley, G. S., Macleod, G., Aplin, A. C., Larter, S. R., Knight, I. and Auld, H. A., 2000, Integrated study of the Judy Field (Block 30/7a) - an overpressured Central North Sea oil/gas field. *Marine and Petroleum Geology*, **17**, 993-1010.

Sylta, Ø., 1991, Modelling of secondary migration and entrapment of a multicomponent hydrocarbon mixture using equation of state and ray-tracing modelling techniques. *In*: England, W.A. and Fleet, A.J. (eds) *Petroleum Migration.* Geological Society Special Publication, **59**, 111–122.

Sylta, Ø., 2005, On the dynamics of capillary gas trapping: implications for the charging and leakage of gas reservoirs. *In*: Dore, A.G. and Vining, B.A. (eds) *Petroleum Geology: North-West Europe and Global Perspectives* - Proceedings of the 6th Petroleum Geology Conference, 625-631.

Takahata, S., 2004, Estimation and petroleum geological interpretation of subsurface pressure regimes. *Journal of the Japanese Association for Petroleum Technology,* **69**,

167-180 (in Japanese with English abstract).

Teige G.M.G., Hermanrud C., Thomas W.H., Wilson O.B., Nordgard Bolas H.M., 2005, Capillary resistance and trapping of hydrocarbons: a laboratory experiment. *Petroleum Geoscience*, **11**, 125-129.

Thomas, L.K., Katz, D.L. and Tek, M.R., 1968, Threshold pressure phenomena in porous media. *Journal of Petroleum Technology*, 174-184.

Thomeer, J.H.M., 1960, Introduction of a pore geometrical factor defined by the capillary pressure curve. *Trans. AIME*, **213**, 354-358.

Tissot, B.P. and Welte, D.H., 1984, *Petroleum Formation and Occurrence*. Springer-Verlag, Berlin, 699p.

Tokunaga, T., Hosoya, S., Tosaka, H. & Kojima, K., 1998a, An estimation of the intrinsic permeability of argillaceous rocks and the effects on long-term fluid migration. *In*: Duppenbecker, S. J. and Iliffe, J. E. (eds), *Basin Modelling: Practice and Progress*. Geological Society, London, Special Publications, **141**, 83-94.

Tokunaga, T., Matsubara, O., Mogi, K., Tosaka, H. and Kojima, K., 1998b, Can we properly model secondary migration in basin simulation? *Journal of the Japanese Association for Petroleum Technology*, **63**, 52-64 (in Japanese with English abstract).

Tokunaga, T., Mogi, K., Matsubara, O., Tosaka, H., Kojima, K., 2000, Buoyancy and interfacial force effects on two-phase displacement patterns: An experimental study. *AAPG Bulletin* **84**, 65-74.

Toth, J., Maccagno, M.D., Otto, C.J. and Rostron, B.J., 1991, Generation and migration from abnormally pressured fluid compartments: discussion. *AAPG Bulletin*, **75**, 331-335.

Underschultz, J.R., 2005, Pressure distribution in a reservoir affected by capillarity and hydrodynamic drive: Griffin Field, North West Shelf, Australia. *Geofluids,* **5**, 221-235.

Ungerer, P., Burrus, J., Doligez, B., Chenet, P.Y., Bessis, F., 1990, Basin evaluation by integrated two-dimensional modeling of heat transfer, fluid flow, hydrocarbon generation, and migration. *AAPG Bulletin*, **74**, 309-335.

Volokitin, Y., Looyestijn, W.J., Slijkerman, W.F.J. and Hofman, J.P., 1999, A practical approach to obtain 1st drainage capillary pressure curves from NMR core and log data. *Proceedings of the 1999 International Symposium of Society of Core Analysts*, paper 9924.

Warren, J. E. and Price, H. S., 1961, Flow in heterogeneous porous media. *SPE Journal*, 153-169.

Welte, D.H., Hantschela, T., Wygralab, B.P., Weissenburger, K.S. and Carruthers, D., 2000, Aspects of petroleum migration modeling. *Journal of Geochemical Exploration* **69-70**, 711-714.

Welte, D.H. and Yukler, M.A., 1981, Petroleum origin and accumulation in basin evolution - a quantitative model. *AAPG Bulletin*, **65**, 1387-1396.

Wilkinson, D., 1984, Percolation model of immiscible displacement in the presence of buoyancy forces. *Physical Review*, **A30**, 520 – 531.

Yamada, T., 1995, A dissipation-based coarse grid system and its application to the scale-up of two phase problems. PhD Thesis, Department of Petroleum Engineering, Stanford University, 125p.

Yang, Y. and Aplin, A.C., 1998, Influence of lithology and compaction on the pore size distribution and modelled permeability of some mudstones from the Norwegian margin. *Marine and Petroleum Geology*, **15**, 163-I 75.

Yielding, G., 2002, Shale Gouge Ratio - calibration by geohistory. *In*: Koestler, A.G. and Hunsdale, R. (eds), *Hydrocarbon Seal Quantification.* NPF Special Publication **11**, 1–15.

Yielding, G., Freeman, B., Needham, D.T., 1997, Quantitative fault seal prediction. *AAPG Bulletin* **81**, 897-917.